The University Of Sheffield.

Characterising and classifying early hypothalamus development

Ian Groves

A thesis submitted in partial fulfilment of the requirements for the degree of Doctor of Philosophy

The University of Sheffield
Faculty of Science
School of Mathematics and Statistics
July 2022

For my Father, and his love of science.

Acknowledgements

Foremostly, I want to extend tremendous gratitude to my supervisors Alexander Fletcher and Marysia Placzek. You both are the ideal mentors, simultaneously prioritising my academic development alongside my wellbeing. I'm thankful for your patience and advice over the last four years, which I know have been invaluable in this research.

I'm also grateful to the members of my office in the school of mathematics and statistics. The COVID-19 restrictions meant that I had few interactions, but all were useful, especially for the machine learning work at the beginning of this thesis. Of course, I also thank the current and past members of the Placzek and Towers groups for both their help with experimental work and friendship throughout my PhD studies. I am also grateful for the advice and support of my advisor Nick Monk, who was always interested in my work and provided a lot of insight.

Finally, I am thankful to my family and friends, who have supported me over the last four years. My parents, who were always available to speak on the phone, or reduce stress by helping look for places to live. My sister and brother-in-law, who offered plenty of advice on the ins-and-outs of a PhD. Lastly, I thank my fiancée Megan, who was unfailingly patient and supportive (not to mention great at picking cats).

Acknowledgement of collaborative work within the thesis

The candidate confirms that the work submitted is their own, except where work that has formed part of jointly authored publications has been included. The contribution of the candidate and the other authors to this work has been explicitly indicated below. The candidate confirms that appropriate credit has been given within the thesis where reference has been made to the work of others.

Section 5.2.1: *In situ* analyses for *SHH* and *FGF10* were performed by Dr K. Chinnaiya, and images were acquired in collaboration with Dr K. Chinnaiya.

Table of contents

Abstract

Understanding the development of the hypothalamus is important, due to its role as the central regulator of homeostasis. However, relative to development of other regions of the brain, characterisation and understanding of hypothalamus development is incomplete. Three important reasons for this are: (i) the hypothalamus is specified early compared to other brain regions, and then develops rapidly; (ii) the hypothalamus has a complex, anatomical structure even in the embryo; (iii) hypothalamic progenitor cells grow and migrate anisotropically. This non-linear growth makes it difficult to interpret downstream developmental events and molecular interactions that regulate early hypothalamus specification and regionalisation.

One promising way to investigate development of the hypothalamus is through combining computational methods and traditional embryological approaches. To this end, I begin this thesis by developing a method of fine-grained classification of the Hamburger Hamilton (HH) stage 10 chick embryo. I was able to train an accurate classifier despite a limited dataset, by testing a variety of biologically motivated data augmentation techniques. I encouraged confidence in the staging system and subsequent classifications by analysing and visualising the output of the classifier.

Using this classifier, I conducted a detailed morphological study of the developing hypothalamus at HH10 and surrounding stages, using both experimental embryology techniques and computational morphometric analyses. Using my increased understanding of the developing morphology, I characterised the expression of key hypothalamus morphogens: *SHH, FGF10,* and *BMP2,* as well as components of the SHH signalling pathway. I found that regionalisation between these morphogens occurred early and rapidly, with substantial heterogeneity in expression along both the anteroposterior and mediolateral axes.

Finally, I tested to what extent this regionalisation is neuroepithelium intrinsic using *ex vivo* culture. I found both anteroposterior and mediolateral regionalisation in culture, which suggests that these processes are self-organising in the neuroepithelium.

Overall, my thesis provides novel insights into early hypothalamic morphogenesis and molecular regionalisation, and shows through extension and use of the classifier how these complex processes may begin to be unpicked.

Chapter 1

Introduction

In this Chapter, I discuss the role, structure, and development of the hypothalamus. I also outline recent work investigating the interface between morphology and gene expression in the developing brain. I next discuss Sonic Hedgehog (SHH), a morphogen of interest in hypothalamic development and a potential link between hypothalamic progenitor cell development and increasing morphological complexity of the hypothalamus. Finally, I discuss the challenges associated with unpicking the role of complex signalling ligands such as SHH in the developing hypothalamus, and introduce a potential role for neural network based image classification in tackling these challenges.

1.1 The development of the hypothalamus

The hypothalamus is an ancient, vital organ of the brain. Located at the base of the forebrain, the hypothalamus functions as a central homeostatic regulator, controlling core survival processes. Recent advances in genetics have revealed that disordered hypothalamic development plays a role in complex diseases such as infertility, obesity, and chronic stress (Bedont *et al.*, 2015; Biran *et al.*, 2015; Eachus *et al.*, 2017; Moir *et al.*, 2017). However, to understand how aberrant development of the hypothalamus could lead to adult disease, we must first understand how the hypothalamus normally develops.

Until recently, the two major working models of hypothalamus development assumed that the complex arrangement of neuronal populations in the adult hypothalamus arise due to isotropic expansion of progenitor cells during embryonic development. The columnar model suggested that the neuraxis is highly organised along the anteroposterior axis from an early developmental stage, and that the hypothalamus develops from a diencephalic structure (Swanson, 1992, 2012; reviewed by Fu *et al.*, 2019). The prosomere model aimed to form a general way of understanding forebrain development. The prosomere model suggests that the developing hypothalamus is the most anterior point of the brain, not the telencephalon. Further, the model groups the hypothalamus and the telencephalon as one developmental unit (Rubenstein *et al.*, 1994; Puelles and Rubenstein, 2003; Bedont *et al.*, 2015). However,

recent work in the embryonic chick, outlined below, has shed light on how hypothalamic development does not conform to either the columnar or prosomere model.

By mid-embryogenesis, the main progenitor subsets that can be recognised (originally demonstrated in the mouse) are the anterior tuberal, posterior tuberal, and mammillary, separated from paraventricular progenitors by progenitors in the intrahypothalamic diagonal (Shimogori *et al.*, 2010; Kim *et al.*, 2020). The spatial arrangement of these progenitors is closely aligned to the spatial arrangement of distinct adult hypothalamic neurons and glia. Thus, tuberal, mammillary and paraventricular neurons differentiate close to anterior tuberal, mammillary, and paraventricular progenitors, respectively, while radial glial-like cells differentiate from posterior tuberal progenitors. However, until recently, it was completely unclear how these distinct mid-embryonic progenitor territories formed. Understanding how these areas develop is important. For example, the paraventricular neuroendocrine neurons of the adult hypothalamus make connections with the tuberally-located glial pituitary gland, thereby mediating the endocrine role of the hypothalamus through the release of hormones (Swanson, 1987). Since many disorders involving hypothalamic dysfunction are neuroendocrine-related, understanding how these regions are built and how the neurons within them ultimately make connections will be instrumental in treating these disorders.

A study by Fu *et al.* (2017, 2019 - described in detail below) in the chick embryo was the first to suggest that the hypothalamic progenitor subsets detected at mid-embryogenesis develop and grow through a complex, non-linear manner. A more recent study by Kim *et al.* (2022), again using the chick embryo, also suggests this. This latter work involved a detailed single-cell RNA sequencing (scRNA-seq) effort over 6 time points from Hamburger-Hamilton (HH)8 to HH20 to understand which genes were expressed by different progenitor cells, at different early hypothalamic developmental time points. The expression profiles of key genes (including *Sonic Hedgehog* (*SHH)*, *Fibroblast growth factor 10* (*FGF10)*, *Bone morphogenetic proteins* (*BMPs:* in particular *BMP2* and *BMP7*) and the transcription factor *NKX2.1*) were verified, visualising expression through a novel in situ hybridisation technique - hybridisation chain reaction (HCR) - which allows multiple mRNAs to be examined in a single sample ((Choi *et al.*, 2018; Kim *et al.*, 2022)).

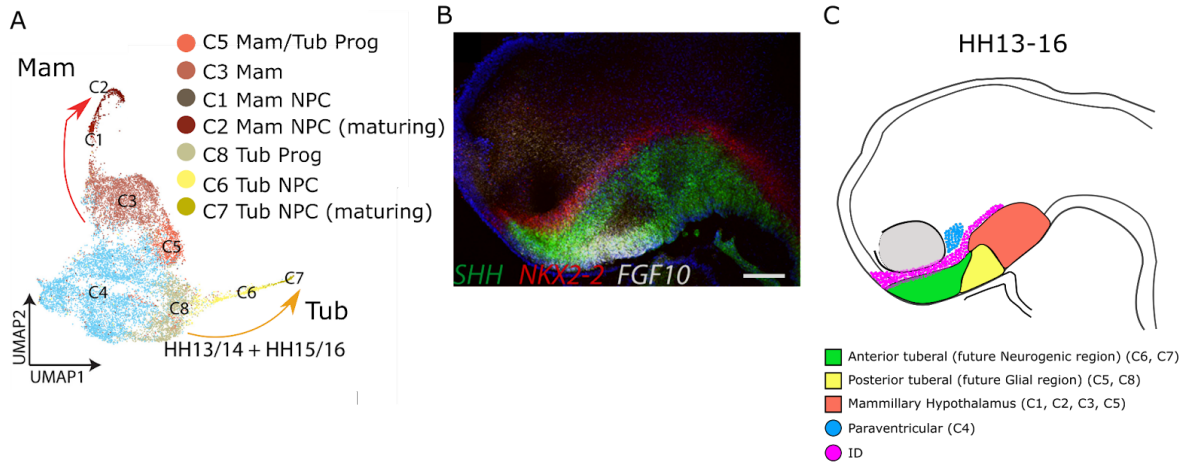

Figure 1.1 Regionalisation of the developing hypothalamus. (A) UMAP clusterings of a scRNA-seq dataset of developing hypothalamus cells at HH13/14 combined with another dataset of cells at HH15/16. Expression of numerous markers enabled the clusters to be identified with distinct progenitor types and maturing neurons. Red arrow: lineage trajectory for mammillary progenitors, orange arrow: lineage trajectory for tuberal progenitors. (B) Side view of a developing chick brain at HH15 following HCR *in situ* hybridization for *SHH*, *NKX2-2, FGF10*. Schematic representation of the HH13-16 developing chick brain in side view. (C) Distinct progenitor cells exist in spatially-defined regions at this stage. (A-C) adapted from (Kim *et al.*, 2022). Scale bar 100µm.

In other words, this study combined bioinformatics analysis with molecular expression profiling to produce a robust picture of the development of hypothalamic progenitor cell types over a large portion of early hypothalamic development. Ultimately, this allowed the authors to link the spatial relationship of progenitor populations profiled across developmental time. At the same time, RNA velocity - an *in silico* analysis that predicts how cells differentiate over time - suggested lineage trajectories from earlier hypothalamic cells, to tuberal, mammillary, and paraventricular progenitors, and then to their respective neurons (Kim et al., 2022; Fig 1.1A).

A principal finding of this work was that chick hypothalamus development could be mapped to well-defined stages of embryonic development: at HH8-10 the hypothalamus was induced from prethalamic-like cells. Between HH10 and HH16 the hypothalamus underwent regionalisation, with distinct gene expression domains arising (Fig 1.1B), giving rise to the same progenitor subsets previously suggested in the mouse (Kim *et al.*, 2020), and between HH13 and HH21 the hypothalamus underwent neurogenesis (Fig 1.1B, C). Importantly, the

study suggested that regionalisation into the distinct progenitor subsets occurred through extensive anisotropic growth from an early population(s) of hypothalamic floor plate-like cells, which are first detected around HH8 (Kim et al., 2022).

The finding that the hypothalamus is induced around HH8, and that at this stage, hypothalamic cells share characteristics with ventral midline floor plate cells, confirmed and extended previous studies (Dale *et al.*, 1997, 1999). These, and the scRNA seq paper of Kim *et al.* showed that hypothalamic floor plate-like cells constitute the anterior-most population of SHH/FOXA2-positive ventral midline cells (Kim *et al.*, 2022), but can be distinguished from more posterior floor plate cells through their expression of hypothalamic transcription factors - such as NKX2-1, and signalling factors - including BMPs (Dale *et al.*, 1997; 1999; Kim *et al.,* 2022). Classic chick embryology approaches - both *in vivo* and *ex vivo* - had shown that hypothalamic floor plate-like cells (originally termed rostral diencephalic ventral midline (RDVM) cells) are induced by underlying the prechordal mesoderm/mesendoderm (Kiecker and Niehrs, 2001; Patten *et al.*, 2003; Ohyama *et al.*, 2005; Placzek and Briscoe, 2005). These studies had shown that prechordal mesoderm/mesendoderm secretes SHH and Nodal, and then SHH and BMPs (Ellis *et al.*, 2015), which work synergistically to induce hypothalamic floor plate cells (Dale *et al.*, 1999; Patten *et al.*, 2003; Manning *et al.*, 2006).

In addition to confirming these earlier studies, Kim *et al.* (2022) extended them, first by significantly expanding the molecular characterisation of hypothalamic floor plate-like progenitors at HH8, and second by showing that hypothalamic floor plate-like progenitors are induced from diencephalic/prethalamic-like cells that express *PAX6* and *Follistatin (FST)*. Since FST is antagonistic to BMP/Nodal signalling by binding extracellularly directly to the ligands (Fainsod *et al.*, 1997; Wu *et al.*, 2008; Kim *et al.*, 2022), a likely possibility is that BMPs and Nodal, initially originating from the prechordal mesoderm, play a role in induction of hypothalamic floor plate cells by FST mediated antagonism.

The scRNA-seq profiling and multiplex HCR analyses showed that, somewhere between HH8 and HH10, *FGF10* is upregulated in hypothalamic floor plate-like cells. The onset of *FGF10* expression, dramatic expansion of hypothalamic floor plate-like cells around HH10, and evidence for extensive growth during regionalisation - all added to the findings of a previous fate-mapping study in the chick, which had provided the first evidence that two of the distinct hypothalamic progenitor subsets (anterior tuberal and mammillary) arise through a mechanism linked to anisotropic growth (Fu, *et al.,* 2017) (Fig 1.2). Upregulation of *FGF10* around HH10, coincides with a dramatic (largely lateral) expansion in the expression of

molecular markers of hypothalamic floor plate-like cells (Dale *et al.*, 1999; Kim *et al.*, 2022). For example, SHH, which is expressed in a rod of ventral midline cells at HH8, is expressed in a wider oval shape at HH10 (Fig 1.3A, B).

Fu et al (2017) injected *FGF10/SHH*-expressing floor plate-like cells in the midline of the HH10 hypothalamus with DiI (a lipophilic fluorescent dye which allows for direct visualisation of cell lineages), and traced these cells to HH17 - a time when anterior tuberal and mammillary progenitor regions are becoming distinct (Fu *et al.*, 2017, Fig 1.1). This study showed that *FGF10/SHH*-positive floor plate-like cells at HH10 undergo extensive tangential migration/growth and ultimately give rise to the anterior tuberal neurogenic domain, and the mammillary progenitor domain, while between these, a third domain, which does not expand, forms the posterior tuberal progenitor domain (Fig 1.2B,C). This is a non-neurogenic zone, which ultimately gives rise to glial cells, including cells that become the infundibulum, median eminence and posterior pituitary (Pearson *et al.*, 2011). The fate-mapping studies showed that each of these three progenitor domains are generated from distinct regions of *FGF10/SHH* floor plate-like cells. Anterior tuberal (neurogenic) cells are generated through the anisotropic anterior growth of the anterior-most *FGF10*-expressing cells, which downregulate *FGF10* as they grow anteriorly; glial tuberal cells are generated from central-most *FGF10*-expressing cells that downregulate *SHH.* Mammillary progenitors are generated through the anisotropic growth of the posterior-most *FGF10*-expressing cells, and retain *SHH* expression (Fu et al., 2017; 2019) (Fig 1.2B-C). Throughout these events, the profile of *SHH* in the developing hypothalamus undergoes dramatic changes: from a rod-shape, then an oval-shape at HH8-HH10, then to the torus-shaped profile that characterises the hypothalamus from HH13 onwards (Figs 1.1B and 1.3). In summary, this work was the first to describe an anisotropic growth model of hypothalamic development in which hypothalamic progenitors migrate, and/or proliferate from earlier FGF10-expressing floor plate-like cells beginning around HH10.

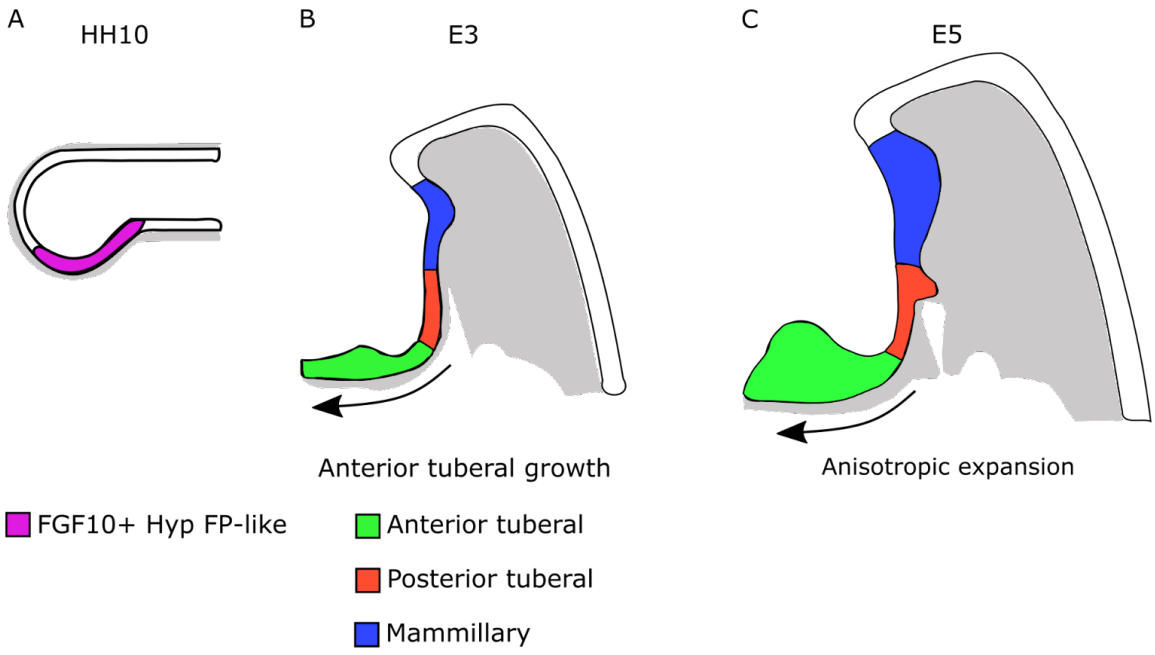

Figure 1.2 Anisotropic growth of the developing hypothalamus. (A) At HH10, the prospective hypothalamus has been induced in the neuroepithelium and is a floor plate (FP)-like FGF10 positive domain. (B) At E3 the hypothalamus has been regionalised into anterior tuberal, posterior tuberal and mammillary domains. At this point, the hypothalamus has begun anisotropic growth i.e. anterior growth from the tuberal domain. By E5, the anterior tuberal domain has expanded, and the mammillary domain has begun to expand.

This study also highlighted a role for the secreted signalling ligand SHH in the growth and differentiation of anterior tuberal progenitors (see Section 1.3 for more details of Shh signalling, and its role in patterning and proliferation). As anterior tuberal neurogenic progenitors emerge from *FGF10*-expressing floor plate cells, they maintain/upregulate *SHH*, and this ultimately promotes their differentiation as measured through p57 expression. This results in a proliferative gradient from anterior (high differentiation, low proliferation) to posterior (high proliferation, low differentiation) (Fu *et al.,* 2017, Fu *et al.,* 2019). If SHH signalling is pharmacologically blocked, using cyclopamine, at HH10 - i.e. a time when floor plate-like cells have already been induced - then the anterior tuberal *SHH*-positive neurogenic progenitors do not grow - as measured by a reduction in the size of the anterior hypothalamic domain concomitant with a reduction of DiI labelled cells in the anterior hypothalamus (Fu *et al.,* 2017) (Fig 1.2). Other studies in mouse similarly suggested that neuroepithelial-derived SHH is necessary for differentiation of anterior tuberal hypothalamic progenitors (Szabó *et al.*, 2009; Shimogori *et al.*, 2010; Carreno *et al.*, 2017)

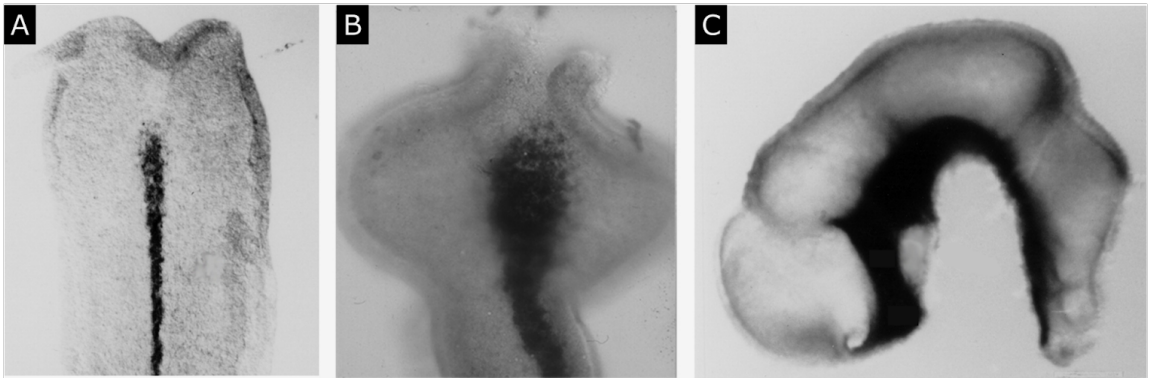

Figure 1.3. *SHH* expression in the early developing hypothalamus. (A-B) show flat-wholemount ventral views and (C) shows a wholemount side view of an isolated neuroepithelium, with *SHH* expression visualised at HH7 (A), HH10 (B), and HH18 (C). (A) At HH7, the neuroepithelium is cylindrical, (B) at HH10, the optic vesicles have extended laterally, which allows the developing prosencephalon (pictured) to be easily identified. (C) At HH18, the developing brain has turned, making ventral views difficult to image, and therefore side views are typically used. At this point, the hypothalamus is detectable along the ventral neuroepithelial tissue. (A-C) adapted from (Manning *et al.*, 2006).

The Fu et al (2017) study demonstrates the dynamic expression of *SHH* and *FGF10*, and raises the possibility that interactions between them may be important in hypothalamic development. Elsewhere in the embryo, *SHH* and *FGF10* regulate each other's expression. For instance, in the developing limb bud (Sekine *et al.*, 1999; Jin *et al.*, 2019), while in the developing lung, FGF10 downregulates SHH to initiate branching morphogenesis (Bellusci *et al.*, 1997; Sekine *et al.*, 1999).

To date, no study has directly investigated interactions between SHH and FGF10 at early stages of hypothalamic development. However, studies have examined interactions between SHH and BMPs. In chick, the prechordal mesoderm secretes BMPs (Dale *et al.*, 1999), which in turn induce the transcription factor TBX2 in central hypothalamic floor plate-like cells (Manning *et al.*, 2006). The study by Manning et al., (2006) also performed gain- and loss-of-function studies showing that TBX2 represses *SHH*, so a likely interpretation is that *TBX2*-expressing cells give rise to the future posterior tuberal progenitors - that ultimately form the glial domain of the tuberal hypothalamus (Figs 1.1. and 1.2).

Work in mouse suggests this is a conserved pathway: here studies have shown that *Tbx2* and *Tbx3* are expressed in a similar pattern to that in the chick, and that Tbx3 directly represses Shh by removing a positive transcriptional regulator (Sox2) (Trowe *et al.*, 2013).

At the same time, *BMPs* themselves - in particular *BMP2* and *BMP7* - are upregulated in the hypothalamus. Initial studies (Kim et al., 2022) suggest that *BMP2* and *BMP7* are expressed very dynamically over HH8-HH18, but their profiles have not yet been investigated thoroughly.

1.1.1 Role of the prechordal mesoderm

As introduced above, a particularly salient feature of the developing hypothalamic neuroepithelium is its relationship with the adjacent prechordal mesoderm, which initially induces hypothalamic floor plate-like cells. The prechordal mesoderm has a complicated spatial relationship with the developing hypothalamus. At HH9-10, the prechordal mesoderm is in line with the developing hypothalamus, but becomes progressively more posterior/caudal to the hypothalamus (Fu *et al.*, 2019). Additionally, the cells comprising the prechordal mesoderm begin to disperse shortly after HH10 (Jacob *et al.*, 1984; Seifert and Christ, 1990; Ellis *et al.*, 2015). How necessary the prechordal mesoderm is for *continued* hypothalamus development is unclear, considering the distancing and dispersal that occur relatively early in hypothalamus development.

Kim et al. (2022) and Fu et al. (2017) were landmark studies in hypothalamus development, shedding light on the induction, regionalisation, growth, and differentiation of hypothalamus progenitor populations. However, they also suggest that the early hypothalamus is highly dynamic, rendering it challenging to decipher how embryonic progenitor populations give rise to the adult hypothalamus. Further, neither of these studies considered an important implication from the anisotropic growth model of Fu et al. (2017): the development of morphological structure.

1.2 Morphological studies of development

There is increasing recognition among developmental biologists that growth and function are intrinsically linked, and understanding their relationship is vital to obtaining a mechanistic understanding of development as well as to harnessing developmental reprogramming to treat disorders.

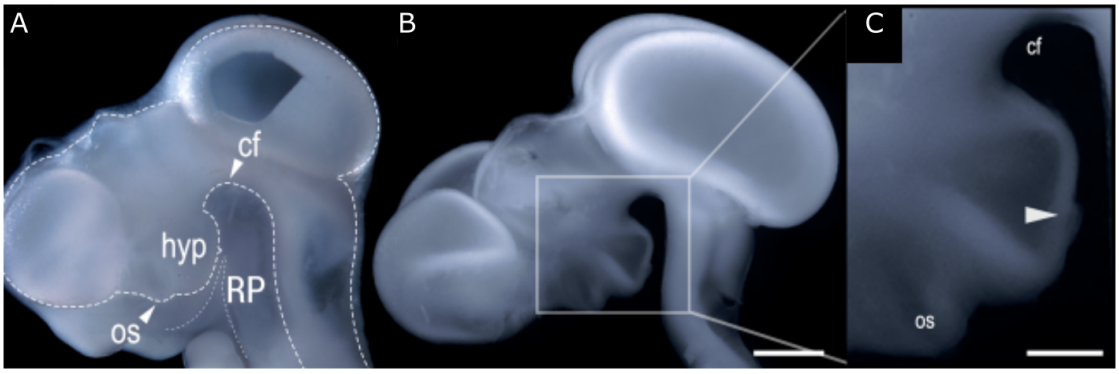

Figure 1.4 Neuroepithelial morphology of hypothalamic tissue in the developing chick. (A-C) show side views of the whole brain at E5 (D), after neuroepithelial isolation (E), and a zoom of the white square box (F). The hypothalamic morphology is only visible after isolation, and protrudes ventrally from the rest of the forebrain. LH: Lateral hypothalamus. AH: anterior hypothalamus. os: optic stalk. hyp: hypothalamus. RP: Rathke's pouch. cf: cephalic flexure. Scale bars: (E) 1000μm, (F) 200μm.

Interest in morphogenesis - the development of biological form or shape as a process - perhaps began with D'arcy Thompson's 'On Growth and Form' which contained mathematical descriptions and analyses of many natural phenomena e.g. shells and eggs (Thompson, 1917). However, interest in the shape and form of the embryo has since stemmed from the Turing's later pioneering work on morphogenesis, where he outlined how an embryo may generate form from *de novo* asymmetries in chemical concentration (and that these asymmetries would cause/allow shape change in an organism). Despite its abstract nature, Turing's work marked a shift in thinking about how embryos might develop (Turing, 1952).

More recently, studies of chick early forebrain morphogenesis have extracted 3-D meshes from biological data of tissue morphology (Garcia *et al.*, 2017, 2019). The authors here investigated the development of shape suggesting that the large structures of the chick forebrain are shaped through an interplay of morphogen gradients and mechanical stresses.

1.2.1 Development of hypothalamic morphology

The work of Garcia *et al.*, (2017) focused on the morphological development of the entire early forebrain, and therefore only included the hypothalamus as a minor consideration, grouping it with the telencephalon. As such, there is not yet a detailed morphological study of hypothalamus development. Such a study would be important because the neuronal populations that form the adult hypothalamus are arranged in a complex manner, and because the hypothalamus develops a distinct adult morphology, protruding ventrally from the rest of the forebrain (Lechan and Toni, 2000).

In chick, the onset of adult hypothalamus morphology might be best studied by investigating the tissue morphology of the ventral neuroepithelium around HH10. Not only does this stage mark the point at which hypothalamic progenitors expand, but it also marks the stage when the prosencephalon begins to close into the anterior end of the brain tube, concomitant with other morphological development such as formation of the optic vesicles (Fig 1.3B, Fig 1.4). Yet, studies on neuroepithelia at these stages have focused to date only on molecular expression and have only used 2-D images, where many ventral morphological features are largely lost (Fig 1.3; Manning *et al.,* 2006). In chick, by embryonic day 5 (E5) the hypothalamus is obscured by surrounding tissues (Fig 1.4A), but if isolated, it can be seen to show a morphology resembling that of the adult, where it has protruded ventrally from the rest of the forebrain (Fig 1.4B-C; Fu *et al.,* 2017).

However, when this adult-like protruding morphology develops is not well characterised, likely because morphological changes occur rapidly in the developing prosencephalon, which makes linking early morphological changes across developmental stages difficult.

A candidate signalling molecule which could mediate growth and differentiation (and therefore more broadly linking morphology to cell fate) in the developing hypothalamus is Sonic hedgehog.

1.3 Sonic hedgehog

Sonic hedgehog is a secreted glycoprotein with many critical roles in vertebrate development. Sonic hedgehog is encoded by the *SHH* gene, which was first cloned on the basis of its high conservation with the *Drosophila hedgehog* gene (Echelard *et al.*, 1993; Krauss *et al.*, 1993; Riddle *et al.*, 1993; Roelink *et al.*, 1994; Marigo *et al.*, 1995) .

Since then, Shh has become the most-studied member of the hedgehog family, and has been shown to play a key role in vertebrate development and organogenesis. Initial studies (described below) revealed the importance of Shh in patterning the embryonic ventral neural tube and posterior limb bud. Soon after, studies indicated that Shh plays an important role in directing a vast array of developmental processes in the embryo, including development of the somites (Fan and Tessier-Lavigne, 1994), foregut (Litingtung *et al.*, 1998), lung (Pepicelli *et al.*, 1998), brain (Ericson *et al.*, 1995; Hynes *et al.*, 1995; Dahmane and Ruiz i Altaba, 1999), and wider craniofacial development (Chiang *et al.*, 1996; Dubourg *et al.*, 2004; Nagase *et al.*, 2005; Haworth *et al.*, 2007).

Further investigation showed that SHH has diverse functional roles in mediating and directing cell proliferation in embryonic cell populations (Rowitch *et al.*, 1999), and has a role in both foetal and postnatal life in circuit wiring and stem cell regulation (Bhardwaj *et al.*, 2001; Palma *et al.*, 2005; Álvarez-Buylla and Ihrie, 2014, 2014; Garcia *et al.*, 2018)

Below, I summarise the current state of knowledge regarding the roles of SHH as both a morphogen and a mitogen in the embryo.

1.3.1 Sonic hedgehog as a morphogen

Turing introduced the concept of a morphogen (Turing, 1952), and subsequent studies (Wolpert, 1969; Crick, 1970) led to its conventional definition: a molecule that diffuses through cells and tissues to establish a concentration gradient that evokes discrete cell responses at particular threshold concentrations to confer position identity and pattern cell/tissue fields.

Classic grafting studies in the chick had suggested that the dorso-ventral (DV) axis of the posterior neural tube (the future spinal cord) and anterior-posterior (AP) axis of the limb bud

are patterned through the activity of a morphogen deriving from ventral midline cells of the notochord and floor plate (Yamada *et al.*, 1991), and the posterior zone of polarising activity (ZPA) (Tickle *et al.*, 1975), respectively. The cloning of SHH provided insight into the molecular identity of this morphogen: SHH showed restricted expression to the notochord, floor plate and ZPA (Echelard *et al.*, 1993; Krauss, *et al.,* 1993; Riddle *et al.*, 1993; Chang *et al.*, 1994; Roelink *et al.*, 1994).

The canonical SHH signalling pathway involves effector zinc-finger transcription factors of the Gli family: Gli1, Gli2, and Gli3. Gli1 exists only as an activator, whereas Gli2 and Gli3 can be converted proteolytically from activator (GliA) to repressor (GliR) forms (reviewed by Carballo et al., 2018). The signalling pathway is initiated when secreted SHH binds Patched1 (Ptc) at the surface of a responsive cell. Binding relieves inhibition of the transmembrane protein Smoothened (Smo) and ultimately triggers the activation of the Gli transcription factors. This in turn results in activation of SHH target genes, including *Ptc*, forming a negative feedback loop (Fig 1.5A).

Gain- and loss-of-function studies of SHH, or components of its signalling pathway, indicated that SHH acts as a stereotypical morphogen in both the neural tube and the limb bud, establishing a concentration gradient that is translated into a GliA-GliR gradient that patterns these tissues and instructs cell fates (although note that the precise regulatory role of each Gli is not fully elucidated) (Riddle *et al.*, 1993; Ericson *et al.*, 1996).

In the neural tube, SHH is secreted from the notochord and floor plate and diffuses through ventral regions of the neural tube, converting Gli2 and Gli3 to GliA forms, and inducing Gli1 (a GliA) (Briscoe and Thérond, 2013). In turn, this leads to the establishment of different progenitor cell types along the dorso-ventral axis (Fig 1.5B). In the developing limb bud, SHH is secreted from the ZPA, travels through the posterior limb bud, and confers posterior identity through canonical induction of Gli1 and prevention of Gli3R (Marigo *et al.*, 1996). (Fig 1.5C). Thus in both systems, the relative levels of GliA-GliR, and the balance between activation and repression of target genes, are the pivotal mechanism by which cells translate a gradient of SHH ligand into a discrete set of cell identities (Briscoe and Thérond, 2013; Tickle and Towers, 2017; Placzek and Briscoe, 2018).

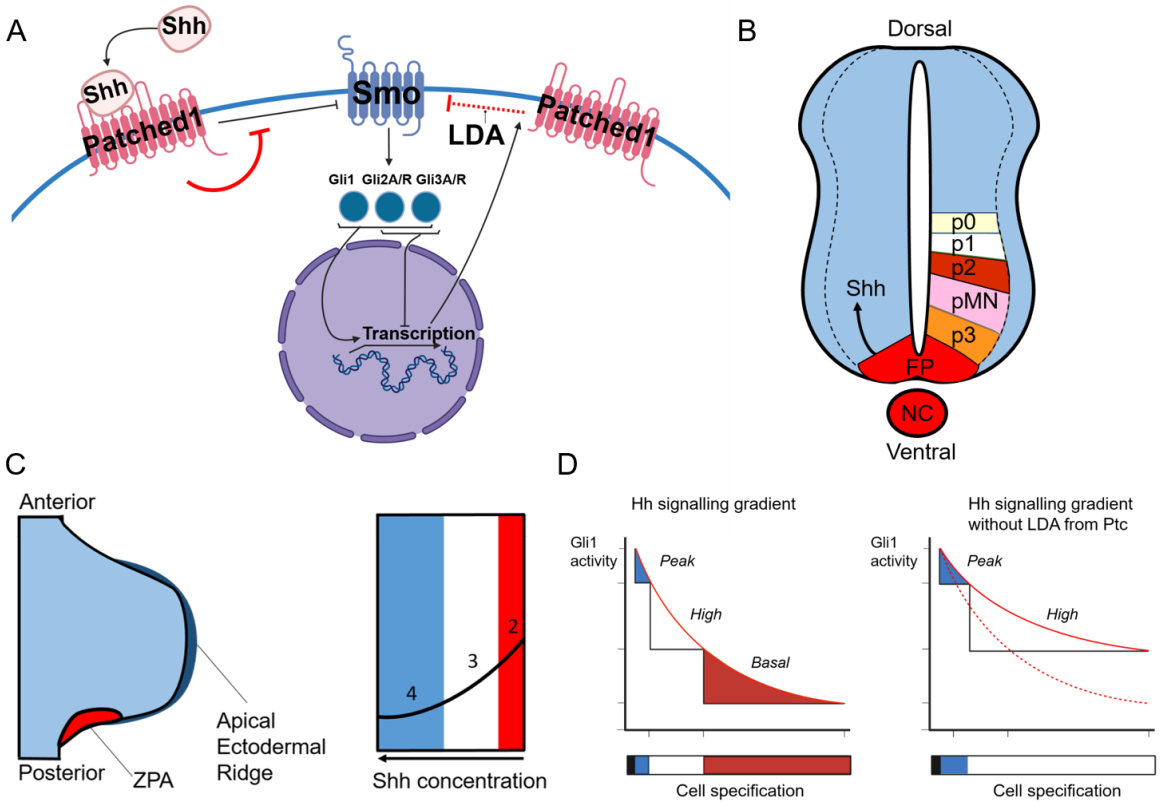

Figure 1.5 Key features of the SHH pathway. (A) Simplified schematic of the canonical SHH pathway. SHH binds to the membrane-bound receptor Patched1, relieving Patched1's constitutive inhibition of Smoothened (Smo). Upon SHH signalling, Smo is able to interact with Gli transcription factors, which initiate transcription of SHH target genes such as the gene encoding Patched1. This gives rise to ligand-dependent antagonism (LDA; red dotted flathead arrow), whereby SHH network activity stimulates the expression of its own repressor (Ptc). Red flathead arrows indicate effects that occur in the presence of SHH binding. (B) Simplified schematic of neural tube patterning by SHH. SHH is expressed by the notochord (NC), and movement of SHH into the floor plate (FP) induces SHH expression in the FP. From here, SHH forms a concentration gradient from ventral to dorsal in the developing neural tube, specifying neural progenitors (p0–3, pMN). Dotted lines indicate progenitor region. (C) Simplified schematic of limb bud digit patterning by SHH. SHH is secreted from the zone of polarizing activity (ZPA) and travels through the posterior limb bud, specifying posterior identity through Gli1 and Gli3 induction. (D) Experimental evidence for Patched1-dependent ligand-dependent antagonism on developing hair follicles, adapted from (Adolphe *et al.*, 2017). Left: The levels of Gli1 activity resulting from a proximo-distal SHH concentration gradient. Right: In a Patched1 genetic knockout, the Hedgehog gradient is no longer attenuated via ligand-dependent antagonism, so high concentration-dependent cell identities are found more distally. Red dotted line is the shape of the wild-type SHH gradient. Adapted from (Groves *et al.*, 2020).

The mechanisms through which SHH becomes spatially distributed in both the neural tube and limb bud remain poorly understood (reviewed by (Tickle and Towers, 2017; Placzek and Briscoe, 2018). Candidate mechanisms include free diffusion (e.g. that discussed in Crick, 1970), or diffusion that is modified by lipid modification of SHH, or its binding to proteoglycans in the extracellular matrix (Saha and Schaffer, 2006).

More recently, additional features of SHH signalling have been revealed, indicating a large amount of complexity to the signalling pathway (reviewed by (Briscoe and Thérond, 2013). SHH is modified by cholesterol, which appears to be vital to the formation of SHH multimers and permits SHH to move through hydrophilic environments (Zeng *et al.*, 2001). Further, cholesterol modification and multimer formation is important for binding to the cell membrane and increasing the range of SHH diffusion, respectively (Gallet *et al.*, 2006).

SHH has also been revealed to be associated with the primary cilia of vertebrate cells. Investigations into SHH signalling and cilia were prompted by comparison of genetic knockout experiments in both mouse and *Drosophila* of SHH signalling components (Goetz and Anderson, 2010). Additionally, diseases involving dysfunctional cilia resemble diseases involving dysfunctional SHH signalling, and studies have since revealed that the primary cilia is important in vertebrate SHH signalling (Briscoe and Thérond, 2013), and is enriched for Patched1 (Rohatgi, *et al.* 2007). Collective studies investigating the location of Gli-related processing components indicated that the primary cilia is the location of Gli proteolysis and therefore important in signal transduction. Additionally, recent studies have highlighted an interplay between Ptc transport through the cilium and cholesterol signalling (Weiss *et al.*, 2019).

Intriguingly, the timing of exposure of cells to SHH - in particular the length of their exposure - are critical to their development: cells are capable of measuring their own exposure to SHH and integrating this as meaningful information over time (Kohtz *et al.*, 1998; Chinnaiya *et al.*, 2014). This challenges the conventional definition of SHH as a morphogen, as it means that absolute levels of SHH are not directly translated into a spatial ‘positional’ value (Briscoe and Small, 2015).

This is perhaps most well characterised in the embryonic chick. Here, in both the neural tube and the limb bud, SHH -responsive cells integrate SHH levels over time and transiently progress through progenitor identities, promoting to sequential ventral, or posterior identities (Zhu and Mackem, 2011; Balaskas *et al.*, 2012). Furthermore, cells can become refractory to SHH over time, via the SHH-induced negative feedback loop described above. Thus, the

higher the amount of SHH signalling over time, the more the pathway is suppressed, a mechanism termed ligand-dependent antagonism (LDA) (reviewed by Dessaud et al., 2008; Groves et al., 2020) (Fig 1.5A, D). The dynamic nature of SHH, with multiple methods of regulation, indicates that to understand SHH‘s action as a morphogen, it is critical to study which cells are receiving SHH signalling, where they are, and for how long they are exposed to SHH.

1.3.2 Sonic hedgehog as a mitogen

A less well characterised role for SHH is as a mitogen, i.e. a regulator of cell proliferation/cell cycle progression (reviewed by Fuccillo et al., 2006; Groves et al., 2020). First described as being critical for proliferation of granule neuron progenitors in the developing cerebellum (Dahmane and Ruiz i Altaba, 1999; Rowitch *et al.*, 1999; Wallace, 1999; Wechsler-Reya and Scott, 1999; Kenney and Rowitch, 2000; Garcia *et al.*, 2018), SHH signalling is now known to govern cell proliferation in many tissues.

In the chick limb bud, classic studies suggested an integration of growth and patterning (Towers *et al.*, 2008), and more recently SHH‘s influence on the cell cycle has been characterised: SHH signalling first stimulates ZPA cell proliferation via Cyclin D2 before down-regulating proliferation in the ZPA through control of BMP2 signalling (Pickering *et al.*, 2019). This fine control of proliferation by SHH ensures that the correct number of digits form in the limb. In spinal cord progenitors, SHH signalling regulates the length of the G1 phase of the cell cycle, decreases cell cycle length and increases expression of Cyclin D1 and N-myc, to expand specific progenitor pools (Cayuso *et al.*, 2006; Ulloa and Briscoe, 2007). In the brain, SHH induces progenitor cell proliferation and the maintenance or growth of progenitor cell populations (Donovan and Dyer, 2005); similarly, SHH has a proliferative role in retinal, telencephalic, and hypothalamic progenitors (Xu *et al.*, 2010; Wilson *et al.*, 2012; Carreno *et al.*, 2017; Fu *et al.*, 2017). Moreover, an important feature of SHH control of proliferation is timing, as SHH first promotes cell cycle progression but then inhibits it (Chinnaiya *et al.*, 2014; Pickering *et al.*, 2019) and in this manner, can play a role in cell cycle exit. Indeed, in the hypothalamus SHH may ultimately upregulate p57, driving cell cycle exit (Fu et al., 2017).

In summary SHH has multiple roles in many developing organs. In the developing hypothalamus there is evidence that SHH may act as a morphogen, mitogen, and regulator

of differentiation. In the hypothalamus, SHH does not simply provide positional information by establishing a spatial morphogenic field, but instead, triggers complex downstream effects that control the entire process of morphogenesis: pattern, proliferation, growth and differentiation. As such, understanding more about the role of SHH in hypothalamus development in an integrated manner may provide clues as to early hypothalamic regionalisation and morphodynamics.

However, this multi-faceted role of SHH in hypothalamic development makes unpicking the relative contributions of SHH expressing hypothalamic progenitors to the overall development of the hypothalamus difficult. One challenge outlined in Section 1.1 is that the floor plate-like cells undergo concurrent specification and migration, all whilst *SHH* expression is dynamic: floor plate-like cells that migrate anteriorly retain, or upregulate *SHH*; central floor plate-like cells switch off *SHH*; posterior floor plate-like cells retain *SHH*.

Traditionally, the actions of SHH have been dissected through genetic or pharmacological interventions, conducted and analysed at specific time-points. Whilst these approaches have enormous merit and are highly tractable, consideration needs to be given to the idea that such studies will inevitably miss many dynamic events, given that SHH (and other developmental factors) are operating under tight timescales and have strong positive and negative feedback loops.

One approach to ameliorate this challenge is to develop a more fine-grained measure of development. In this way researchers could begin to unpick the function of SHH in the hypothalamus through careful experiments which are more finely discretized through development, so as to not miss key events. Below, I will discuss efforts to develop more fine-grained methods of staging development, before illustrating how this method could further our understanding of hypothalamus development.

1.4 Challenges in developmental staging

As discussed above, chick embryos have been used to drive our understanding of early brain development (Placzek and Briscoe, 2018). Yet, as with many model organisms in developmental biology, chick embryos are difficult to obtain in large numbers. As such, developmental biology datasets are typically small. As a further consideration in the chick, the rate of development is sensitive to both intrinsic and extrinsic factors (for instance,

temperature) so developmental staging is usually based on morphology, not chronological age.

In the chick, developmental stages are made with reference to the Hamburger-Hamilton (HH) 1955 staging guide, which assigns embryos to stages between HH1 (newly incubated egg) through 46 (newly hatched chick) (Hamburger and Hamilton, 1951). This classic staging guide is based on numerous morphological metrics, but for early stages when the brain is forming, relies on the number of somites – segmented pieces of tissue that are laid down at highly regular intervals on either side of the spinal cord (Palmeirim *et al.*, 1997). However, observational studies have shown that the rate/timing of development of different body structures, including the brain, is subtly uncoupled from somite number, and increasingly, researchers are attempting to develop bespoke staging methods for distinct embryonic regions (Newgreen and Erickson, 1986; Palmeirim *et al.*, 1997; Boehm *et al.*, 2011; Sáenz-Ponce *et al.*, 2012; Musy *et al.*, 2018).

In the neural tube, this asynchrony could be explained by the presence of a highly migratory type of progenitor cell called the neural crest cells. These cells migrate away from the developing neural tube and contribute to a wide variety of organs throughout the developing embryo (Newgreen and Erickson, 1986). However, unlike when using somite number, there is no clear timing of neural crest cell migration which has straightforward readouts.

One way to address this would be to use different classification schema for determining how developed an embryo is. A particularly promising approach is through the use of deep neural network based image classifiers.

1.5 Image classification

Image classification is the process of assigning an image into a class, which is a discrete grouping of images which share similar characteristics or features. Usually, image classification problems are *supervised* problems, where the images are manually labelled by a person. An early example of supervised image classification is the method of random forest classification, where satellite images were included as part of the cohort of test datasets (Breiman, 2001). The field of image classification has since expanded at a rapid pace since the popularisation of deep neural network (DNN) based image classifiers. This is

because all non-neural network based image classifiers (henceforth termed ‘traditional’ image classifiers) typically underperform compared to DNN based classifiers, and have a reduced ability to learn complex features about a dataset.

1.5.1 Neural networks for image classification

In classification problems, neural networks are statistical models which can be used to estimate the probability of input data belonging to a particular class . In the case of image classification, typically a neural network is trained on some subset of a labelled dataset, referred to as the training dataset (Goodfellow *et al.*, 2016). From this training dataset, the network learns features from the image, makes a prediction about which class the image image belongs to, checks this against the label, and then gives more weight to the components of the network which brings the estimation closer to the correct answer, or reduces the weight in the case of a wrong answer. In this way the network iteratively learns which parts of the dataset described the classes well. Adding several feature extraction layers creates a *deep* neural network (DNN), which has become the *de facto* method of use of neural networks (LeCun *et al.*, 2015).

DNN image classifiers have become popular for several reasons. They are well suited to supervised problems, i.e. a classification problem where there is a labelled dataset with the true classification. This is referred to as the *ground-truth* dataset. This forms the basis of a training dataset, from which a DNN can iterate through whilst learning increasingly complex non-linear features about the images in the training dataset, rather than having to work with more simple, pre-measured features. Perhaps most importantly for a developmental biologist, this means that training a DNN to solve a classification problem allows them to easily share a method for classifying their data without an exhaustive list of criteria.

1.5.2 Developmental biology applications

The use of DNNs in analyses of *in vitro* fertilisation (Khosravi *et al.*, 2019) and cell cycle (Eulenberg *et al.*, 2017) (reviewed by (Hallou *et al.*, 2021)) first pointed to the power of this approach in the field of developmental biology.

DNNs were recently used to classify the developmental stage of zebrafish tailbuds, an experimental model for posterior spinal cord growth (Pond *et al.*, 2021). In this study, networks were trained on 2-D and 3-D image datasets, Bayesian optimisation (introduced further below) was used to tune network architecture, and success was judged through classification accuracy. While this study provides proof-of-principle for using DNNs to classify developmental stages, it did not test the DNN's ability to classify unseen or out-of-distribution data – its capability to generalise (Rosin and Fierens, 1995). This aspect of DNNs in developmental biology is therefore yet to be fully leveraged, and an important goal is to determine the approaches that best improve generalisation.

It is conventionally thought that the training of a neural network requires a large amount of data. The challenge is however, in many areas of biomedical science, it is often impractical to generate large amounts of data due to cost, time, or ethics. In such cases, it is important to maximise the utility of limited data when training DNNs, but how best to do this remains an open question.

1.5.3 Data augmentation

When large datasets are not available, data augmentation (through transformations such as rotations) is a particularly useful technique for expanding the training regime, with the intention that a classifier will learn the class-defining features of the image, and will disregard irrelevant features, including image acquisition artefacts (Simard *et al.*, 2003).

Augmentation transformations include those that are 'label-preserving', i.e preserve the features of the image that originally assigned it to a given class. In addition, new data augmentation methods have been developed that only partially preserve labels, for instance, an approach where a 'cutout' is used to mask a random portion of the image (DeVries and Taylor, 2017). This approach reduces the classifier's reliance on those masked parts of the image. As a result, the classifier is encouraged to learn more general features, thus becoming more robust and less sensitive to artefacts in the training dataset.

Another augmentation method that partially preserves labelling are Möbius transformations, which are bijective conformal mappings (Zhou *et al.*, 2021) i.e. that lines and curves in the input are mapped to a transformed line or curve in the output but local angles are preserved. In this way, Möbius transformations are some combination of other simpler

transformations, e.g. translation, rotation, scaling. Möbius transformations have been used successfully in image classification in non-biomedical/developmental biology use-cases, and have been found to be useful in training networks on limited datasets. To date, Möbius transformations are untested on developmental biology datasets. This may be worth exploring as they may be particularly effective in accounting for user error in microscopy image acquisition. For example, if a user damages the sample during acquisition, Möbius transformations may be able to emulate this. By normalising the user error feature space, the DL algorithm is discouraged from learning these erroneous features.

Besides data augmentation, classifier performance may be improved by optimising parameters of the DNN that are set prior to training. These so-called *hyperparameters* include the number of computational units (neurons) in the network, and the rate at which these units update – the learning rate. Hyperparameter optimisation is typically carried out via systematic (LeCun *et al.*, 1998) or random (Bergstra and Bengio, 2012) testing of values. More recently, Bayesian optimisation techniques have been leveraged, with a surrogate probability model used to inform which values are tested (Shin *et al.*, 2020). An open question then, when training DNNs on microscopy images, is how to exploit data augmentation and network optimisation techniques to best exploit small datasets.

One way that this could be answered is through incorporation of domain expertise. In statistics, domain expertise is contextual knowledge or factual insight which relates specifically to the dataset which is being modelled (Hjørland and Albrechtsen, 1995). In the case of developmental biology, this could take many forms. For example, specific features of the development of a tissue down to a molecular or cellular level, or relatively higher level considerations, such as what microscope data were acquired on, etc. Intuitively, incorporating domain expertise when designing a strategy to deal with an image classification problem may improve the classification accuracy.

Another challenge in training image classifiers for specific applications in developmental biology is assessment and analysis of the resulting classifier. One way that this can be done is through saliency maps. These are visualisations which show parts of an input image the classifier is using to make a classification (Simonyan *et al.*, 2014), assessing both the efficacy of data augmentation, and a DNN's capability to generalise. In this way, saliency maps enable insight into the 'black box' approach of using a high accuracy DNN classifier, an important step in increasing uptake of DNN use in developmental biology.

1.6 Thesis aims

Recent studies have dramatically advanced our understanding of early hypothalamus development. Why these studies have only come recently is because the hypothalamus is relatively difficult to study. It is specified early compared to many other developing organs, and it appears that progenitor cells in the hypothalamus progress rapidly through different molecular states. Further, there has been relatively little characterisation of the tissue morphology at early time points, and how the development of that morphology may be influenced by and in turn influence further hypothalamus development.

There is now a good understanding of when the hypothalamus is specified, at around HH8. However the morphology of this stage (and others) is difficult to examine experimentally, requiring fine microdissection to preserve the 3-D neuroepithelium.

Further, whilst Kim et al. (2022), and Fu et al. (2017) made progress towards characterising hypothalamic progenitor locations and transitions in molecular identity, a complete understanding has not yet been achieved. This is likely due to the rapid and early development of the hypothalamus, making it easy to miss important developmental milestones and short lived molecular identities of the progenitor cell populations.

These considerations in mind lead to the following open questions:

1. Can DNNs be used to sub-stage the developing chick brain in a more fine-grained manner than conventional staging methods (i.e. Hamburger-Hamilton)?
2. What is the structure of the early tissue morphology when:
    a. The hypothalamus is being specified?
    b. The hypothalamus is being organised into distinct progenitor regions?
3. What are the earliest signs of regionalisation that prefigure the organisation of the hypothalamus into anterior and posterior tuberal, and mammillary progenitor domains?
4. To what extent is the regionalisation of the developing hypothalamus intrinsic, or does it rely on external factors (e.g. from the PM)?

To address these questions, I aimed to conduct the following research:

1) I began by subdividing HH10, a critical and dynamic stage in hypothalamus development. I sought to understand to what extent any morphology-based sub-stages I derived could be made reliable and consistent through the use of DNN-based image classification (Chapter 3).
2) With an accurate classifier, I then aimed to further characterise morphology in 3-D at and around my sub-stages (Chapter 4).
3) Having conducted a thorough morphological study of these stages, I next aimed to see whether these morphological structures could be explained/linked to early gene expression dynamics (Chapter 5).
4) Finally, I wished to test to what extent the morphological and molecular development I characterised in Chapters 4-5 was autonomous, through the use of *ex vivo* tissue culture (Chapter 6).

Chapter 2

Materials and Methods

2.1 Image classifier construction and training

2.1.1 Data acquisition

Ground-truth data used for training and validating the image classifier comprised bright-field and phase contrast microscopy images of HH10 (9-12 somite) chick embryos, and included published and unpublished data. Images were acquired using the following microscopes: Olympus BX60, Zeiss AxioImager.Z1, and a Leica dissecting microscope at 4x or 10x magnification. Training data were labelled into three sub-stages, termed 10.1, 10.2 and 10.3, based by Prof. Marysia Placzek, according to the gross morphology of the HH10 brain. Briefly, stages were assigned according to the overall shape of the prosencephalon, the angle of the posterior prosencephalon relative to the prosencephalic neck, and optic vesicle shape. There are 151 images in the dataset, with 54 sub-stage 10.1, 55 sub-stage 10.2, and 42 sub-stage 10.3 embryos respectively. The limb dataset contained 269 images, with 150 labelled as control, and 119 labelled as treated, and were acquired as described in (Towers *et al.*, 2008). The images of both datasets were JPEG format, and varied in resolution, from 188 x 188 to 1000 x 1000 pixels.

2.1.2 Statistical analysis of somite numbers

I did not assume that the variance of somite number with sub-stages is evenly distributed. Therefore, this relationship was analysed by an unpaired *t*-test with Welch's correction.

2.1.3 Clustering analysis of brain dataset

I first reduced the dimensionality of the raw images via principal component analysis (PCA) (Partridge and Calvo, 1998). I determined the appropriate number of PCs to be 2 by iteratively increasing this number from 1 until I found diminishing returns in the proportion of variance explained. I then performed *k*-means clustering on the dimensionally-reduced dataset (Ranjan *et al.*, 2017), determining the appropriate number for *k* to be 3 by iteratively increasing this number from 1 until I found diminishing returns in the reduction in within-cluster sum of squares (WCSS) (Bholowalia and Kumar, 2014). All clustering was implemented in Python 3.6 using scikit-learn 0.24.1 (Pedregosa *et al.*, 2011). Chapter 3, Figs 3.2-3.3 were generated using seaborn 0.11.2 (Waskom *et al.*, 2021) and matplotlib 3.2.2 (Hunter, 2007).

2.1.4 Data preprocessing

I tested a variety of data augmentation regimes (Tables 3.1-3.2 Appendix Tables 2-4, Fig 3.4). To make the trained model invariant to image features that are not classifying (e.g. scale, colour), various preprocessing methods were applied. Images were converted to grayscale, resizing to 200 x 200 pixels using openCV (3.4.2.17) and pillow (8.3.1) (Bradski, 2000; Clark, 2015). 200 x 200 is sufficiently small to be easily processed, whilst retaining sufficient spatial resolution to distinguish morphology. I normalised the histograms of each image, using the pillow function ImageOps.equalize (Clark, 2015). This served to brighten images that were too dark and vice versa. For sharpening (Table 3.1), I used the pillow function ImageFilter.SHARPEN (Clark, 2015).

2.1.5 Data augmentation

Following preprocessing, I constructed a baseline augmented dataset. For microscopy images, a common user-generated feature during data collection is the orientation of the sample. Thus I included rotation as a baseline augmentation, choosing to rotate each image by 36 multiples of 10°. The rotation method enlarged the images on rotation without cutting

off any part. This meant that in addition to rotational and colour invariance, scale invariance would be included into the baseline datasets. For the limb classification, I also incorporated flipped images as part of the baseline, ensuring the left/right symmetry. All augmentations were implemented with imgaug 4.0 (Jung *et al.*, 2020).

2.1.6 Traditional classifiers

To construct my Random Forest, Support Vector Machine (SVM), and *k*-Nearest Neighbour (KNN) classifiers, I used scikit-learn (Pedregosa *et al.*, 2011). For each, I fit 10 separate models, generating a new training and validation split for each model. The data splitting followed a 80:20 ratio (120 training, 31 validation images).

2.1.7 Cross-validation

Initially, I used hold out cross-validation, where a portion of the dataset (in my case, 20%) is held back and used as a validation set. I trained 10 models per augmentation regime, reshuffling the training/validation data each time. My results were substantially variable, e.g. for models trained on the Baseline dataset, the difference between the minimum and maximum validation accuracy was 26.9% (Appendix Table 4). I supposed that this variability was a product of the small dataset. As 20% of the dataset was being held back, even just a few skewed features present in the training or validation set would affect results. Therefore, I employed *k*-fold cross validation (Tables 3.1-3.2, Appendix Tables 2-3). This ensured that I made use of the entire dataset, as well as isolating the portions of the data contributing to variable results (Fushiki, 2011). Briefly, I partitioned the dataset into 10 non-overlapping folds of 15 images. I then trained the network on folds 2-10 and validated with the first fold. Following this, the network was then trained with folds 1 and 3-10, with the second subset used to validate. This proceeded until all folds were used. In this way, I averaged performance of the neural network across the entire dataset.

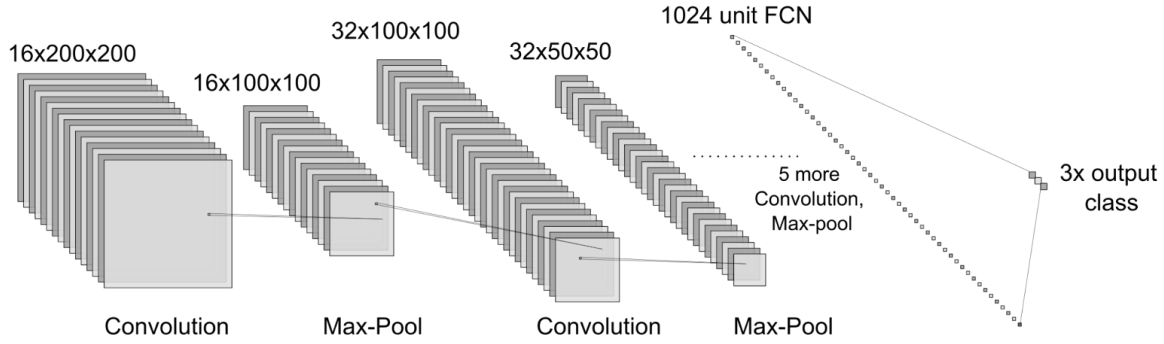

Figure 2.1 Image classifier network architecture. After the input layer, the image was processed following the VGG block style, i.e. through increasingly wide convolution and max pooling layer pairs (Simonyan and Zisserman, 2014). At each 'block' I used a single convolutional layer which retains resolution through padding. Following this, a max pooling layer is used as a method of spatial downsampling. Between each convolutional layer and max pooling layer there is a non-linear ReLU activation function and a dropout layer. For simplicity, only 2 of the blocks are shown. After the final max pooling layer, the data was passed through a wide fully connected layer. Lastly, the classification is made in the output layer. Diagram generated using NN-SVG (LeNail, 2019).

2.1.8 Neural network architecture

I based my bespoke DNN on the Visual Geometry Group (VGG-16) model architecture, which has been highly successful for image classification (Simonyan and Zisserman, 2014) (Fig 2.1). This architecture involves repeated functional units or VGG 'blocks', each comprising a convolution layer with resolution preservation followed by a max-pooling layer that performs two-fold spatial down-samplin. I depart here from VGG-16, as I only include one convolutional layer between each max pooling layer. Between the convolutional and max-pooling layers there is a Rectified Linear Unit (ReLU) activation function (Agarap, 2018). As the actual spatial resolution of the data decreases, the number of filters doubles. Thus, the first layer that receives the 200 x 200 image input has 16 functional units, which is repeated 6 more times resulting in a final convolutional layer with dimensions 4 x 4, with 1024 functional units. This follows a similar pattern to VGG-16, however the largest convolutional layer in VGG-16 is 512 wide, whereas I extend to 1024. Following these blocks, I include a fully connected layer of 1024 units, followed by a softmax classification

layer for the brain classification, or a sigmoid classification layer for the limb classification. Here, my model differs from VGG-16, which uses three wider fully connected layers. All neural networks were built with Keras 2.3.0 (Chollet and others, 2015) and trained using TensorFlow 2.2.0 (Abadi *et al.*, 2015).

2.1.9 InceptionV3 and ResNet50

I tested two common neural network architectures: InceptionV3 (Szegedy *et al.*, 2015) and ResNet50 (He *et al.*, 2016). First, I randomised the weights, before training for 1-50 epochs (full training cycles). The exact number of epochs varied as I implemented early stopping, halting training if 10 epochs had passed without a change in validation accuracy over a 0.01% threshold. The number of epochs to pass, and the early stopping threshold, were selected empirically based on the speed at which models that were allowed to run to 50 epochs converged. When this was triggered, I restored the highest scoring weights in training before saving the model. Following the typical approach (Goodfellow and Bengio, 2016) I inserted a softmax classification layer as the last layer in the model. The softmax activation performs the actual classification by transforming the input between 0 and 1 outputting three values which sum to 1, which effectively define probabilities of the input belonging to each sub-stage. This was necessary as both InceptionV3 and ResNet50 were designed around the ImageNet dataset (1000 classes). I used the Adaptive Moment Estimation (Adam) optimiser with an initial learning rate of 10^{-4} (Zhang and Mitliagkas, 2019), but decreased this to 10^{-5} after I observed overfitting. However, 10^{-5} is also commonly used for image classification (Zhang and Mitliagkas, 2019; Margapuri *et al.*, 2020). Hyperparameter fine-tuning was implemented using TensorFlow 2.2.0 (Abadi *et al.*, 2015) and Keras 2.3.0 (Chollet and others, 2015).

2.1.10 Training regime

As above, I trained for no more than 50 epochs, and implemented early stopping. I regularised the network with L_2 regularisation (weight decay), which penalises large weights in the neural network (Goodfellow and Bengio, 2016). The key parameter, λ, is a fraction of the sum of the squared weights of the network. As λ increases, the loss function value increases. Because a neural network is optimised by minimising the loss function, L_2 regularisation encourages smaller weights and thus less complex models. I chose the numerical value of λ through Bayesian optimisation (Appendix Table 6) as 10^{-4}. This value has been found to be effective in training image classifiers (Gabas *et al.*, 2016).

I also used dropout, which randomly turns off neurons in a layer at a given rate (Srivastava, 2013). This discourages individual neurons from becoming dominant, encouraging a classifier with better generalisability. I added a 20% dropout layer between each convolutional and max pooling layer, and a 50% dropout layer before the final classification; these percentages were also determined through Bayesian optimisation (S6 Table). I used the optimiser Adam, with a learning rate of 10^{-4}, determined through Bayesian optimisation (Appendix Table 6). I set the range of trialled learning rates to test during optimisation (10^{-1}–10^{-6}) according to my InceptionV3/ResNet50 learning rate of 10^{-5}. My model has fewer trainable parameters than both InceptionV3 and ResNet50. Due to this, training converged more slowly, and therefore it is unsurprising that my model performed optimally with a faster learning rate than ResNet50 or InceptionV3.

2.1.11 Saliency analysis

I generated saliency maps using tf-keras-vis 0.8.0 (Yasuhiro, 2021). In these, image pixels are coloured based on whether they contribute positively (hot colours) or negatively (cold colours) towards the output prediction. This produces a map of the features of an input the network deems most and least important towards a classification. I used the SmoothGrad method, which produces clean saliency maps by adding noise to the input image (Smilkov *et al.*, 2017). To understand the decision making of the classifier on real-world data, I generated the saliency maps using test images, which were not involved in model training or validation.

2.1.12 Software

The neural networks were built and trained using Python 3.6. The models were trained on a NVIDIA Tesla V100 GPU using the HPC system provided by the Joint Academic Data Science Endeavour (JADE) II. The code and software dependency list are publicly available at https://github.com/ianbgroves/chick_embryo_DCNN_classifier.

2.2 Chick embryo dissection and histological techniques

Fertilised Bovan brown chicken eggs (Henry Stewart & Co, Norfolk, UK) were incubated in humidified 37℃ incubators, collected from eggs, and staged according to the Hamburger and Hamilton staging criteria (Hamburger and Hamilton, 1951), or where stated according to my HH10 sub-staging system (labelled 10.1, 10.2, 10.3 for staging criteria see Fig 3.1).

All dissections used No.5 forceps (Dumont, 11251-20), spring scissors (Vannas, 15018-10), and tungsten needles sharpened via electrolysis.

All experiments involving live chick embryos conformed to the regulatory standards of the University of Sheffield, and were carried out according to the UK Animals (Scientific Procedures) Act 1986. No ethical approval or Home Office licensing was required, as chicks were not incubated beyond E3.5 (hatching is E21). Named Animal Care and Welfare Officers (NACWOs) had oversight of all incubated eggs.

2.2.1 Sagittal sectioning

Embryos were collected as described above, then washed in phosphate-buffered saline (PBS; Sigma, P4417), and equilibrated overnight at 4℃ in 30% sucrose (Sigma, S0389) for cryoprotection.

2.2.2 Neuroepithelia dissection

Hamburger-Hamilton stage 6-14 embryos were removed from the egg using and incubated in 1mg/ml Dispase I (Roche) at room temperature for 10-25 minutes depending on stage. Following this, neuroepithelia were extracted from the underlying mesoderm and endoderm tissue using tungsten needles (Fig 2.2).

2.2.3 Explant dissection

Neuroepithelia were acquired as described in Section 2.1.1, and hypothalamic tissue was explanted using tungsten needles. Four cuts were made, such that the explanted tissue is approximately a square of tissue around the ventral midline. At stages HH8-9, the explanted region was guided by the gene expression domains of *Sonic Hedgehog* (*SHH)* and *Patched-1 (PTCH1)*. At stage HH10 (i.e. 10.1-3), the explanting was guided by the A-fold/A-base morphology described in Chapter 4.

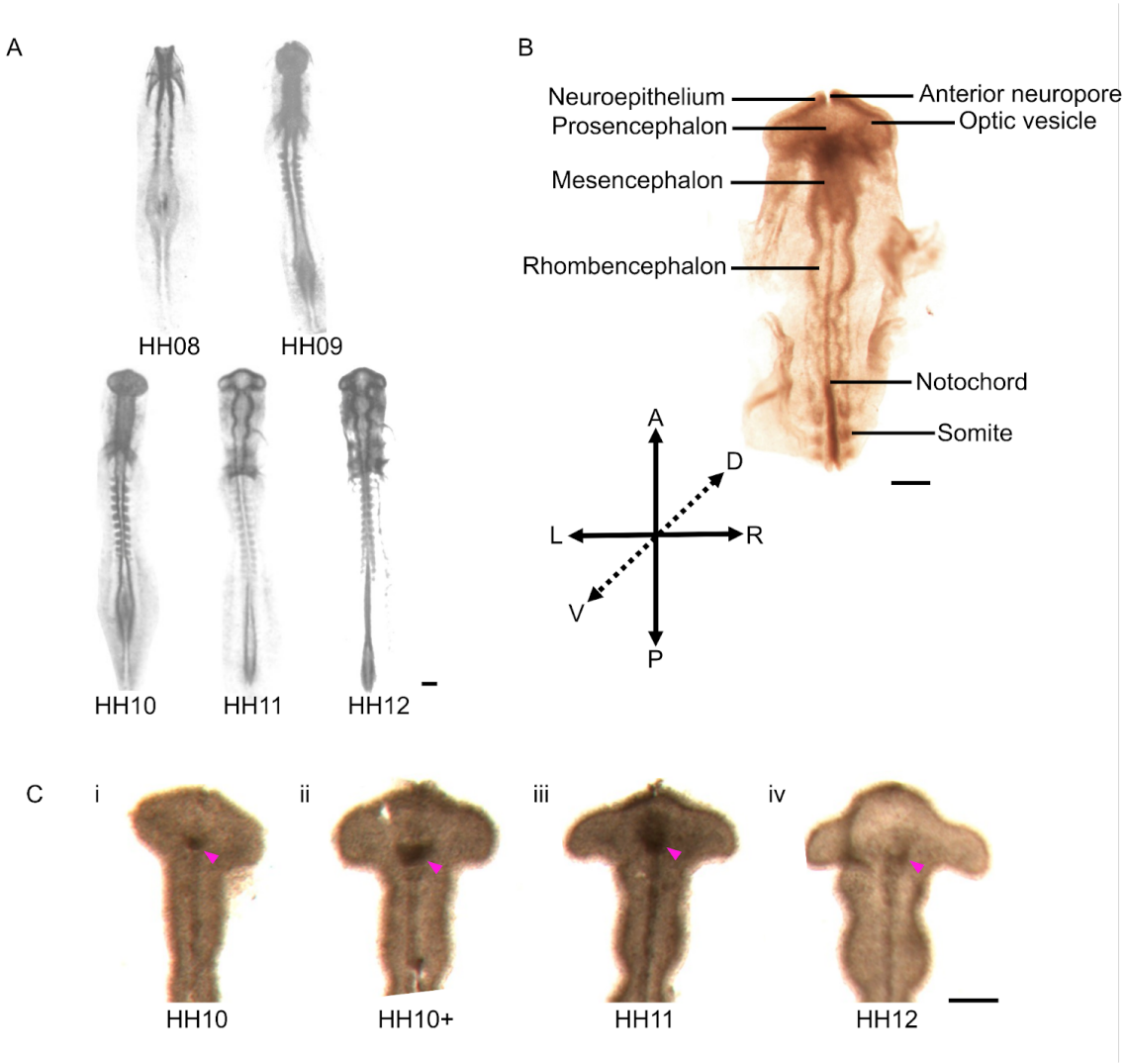

Figure 2.2 Dissection of chick embryonic neuroectoderm. (A) Bright-field images showing dorsal views of wholemounted HH8-HH12 embryos reproduced from (Hamburger and Hamilton, 1951). (B): Bright field image showing a ventral view of an HH11 embryo partially dissected following protease digestion, with key anatomic features labelled. A-P: Anterior-posterior. D-V: Dorsal-ventral. L-R: Left-right. (C) Dissection of neuroectoderm allows for visualisation of hypothalamic morphology. (i-iv) Bright field images showing ventral views of HH10-12 isolated neuroepithelia. Magenta arrowheads indicate a thickening of tissue in the rostral diencephalic ventral midline. Magnification – 5.4x. Scale bars: 200μm.

2.2.4 Hybridisation Chain Reaction *in situ* hybridization

Samples were fixed in 4% Paraformaldehyde (PFA) at 4℃, dehydrated in a methanol series and stored (minimum) overnight at -20℃. Following dissection, the samples were rehydrated in a reverse methanol series and washed in phosphate-buffered saline + 0.1% Tween-20 (PBST). The samples were then incubated in Proteinase K (10µg/mL) for 120-210 seconds (depending on sample developmental stage), refixed in 4% PFA at 4℃ which was then washed off with PBST, followed by washes with 5X Saline-Sodium Citrate (SSC).

Following this, the neuropethelia were incubated in hybridisation buffer for 30 minutes at 37℃. Next, the samples were incubated at 37℃ overnight with mRNA probes targeting the gene of interest, which contained an I1 initiator sequence with the ability to bind to fluorescently tagged DNA (Fig 2.3A).

The following day, the samples were washed as follows: 4 times with HCR wash buffer, 2 times with 5X SSC buffer. The samples were then pre-incubated with amplification buffer for 5 minutes. Fluorescently tagged DNA Hairpin pairs matching the probes were snap-cooled by heating to 95℃ for 90 seconds and allowed to cool to RT in the dark for 30 minutes. Snap-cooling is a necessary step, as it removes any aberrant polymerisation of the hairpins that may have occurred in storage, ensuring that the hairpins form monomeric strands (Choi *et al.*, 2018). Following this, hairpin pairs were mixed with the amplification buffer and the solution was added to the samples (Fig 2.3B). These were incubated overnight at RT, in the dark. Here, the chain reaction took place, whereby the hairpins bound to the I1 initiator sequence assembled long sequences with multiple fluorophores, amplifying the fluorescent signal (Fig 2.3C). The following day, samples were washed 5 times in 5X SSC, followed by a final wash of PBST + DAPI (1µL/mL).

For probe stripping, the samples were washed in 2X SSC + Tween 20 (SSCT), preincubated in DNAse buffer for 15 mins (100µL/mL in H20) (Fig 2.3D). After this, the samples were incubated overnight in DNAse I in solution (10µL DNase I, 50µL DNase buffer, 440µL H20). The next day, the samples were washed three times with 30% formamide in 2X SSC and three times with 2X SSC. After this, the samples were labelled via the HCR method detailed above.

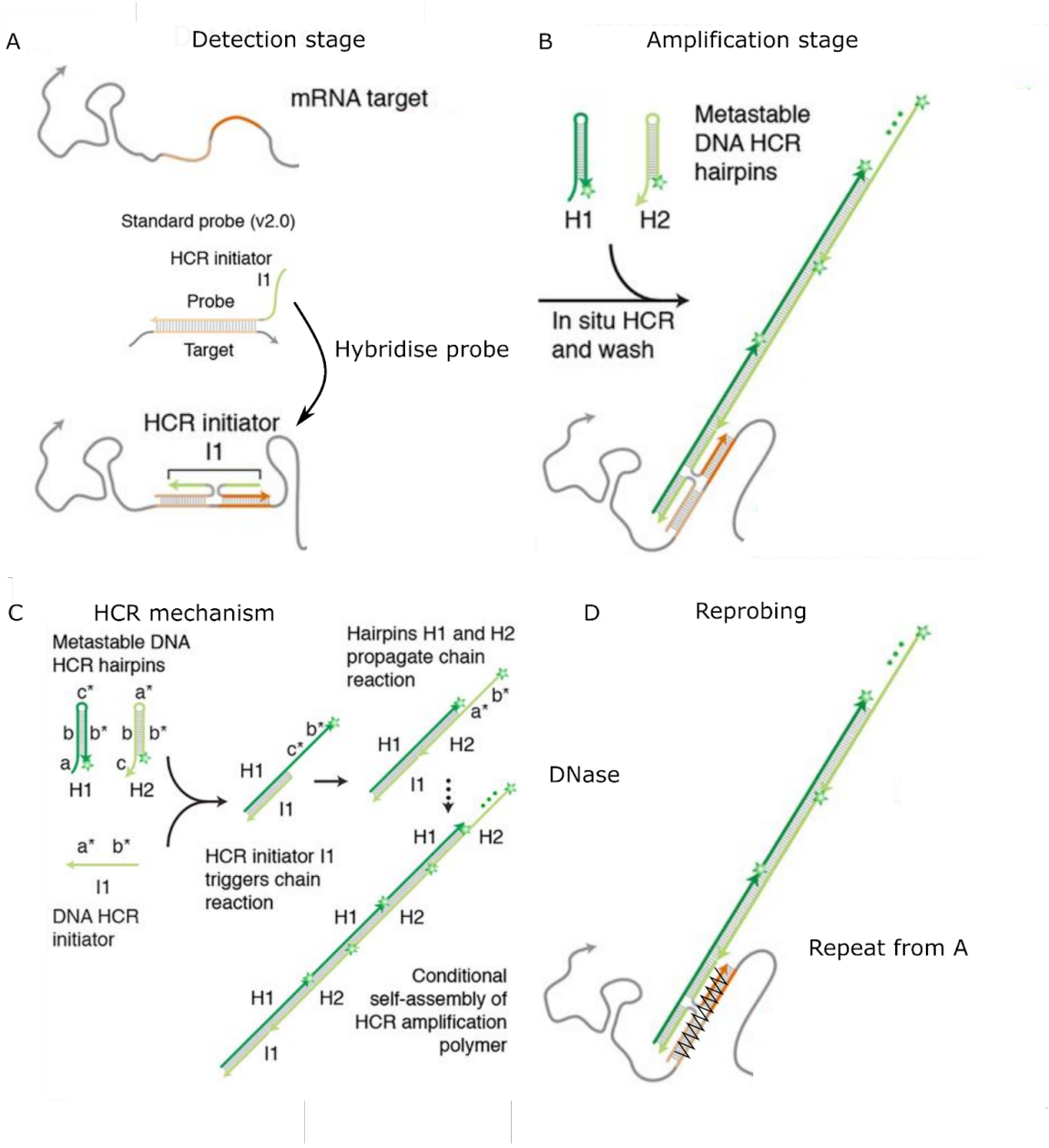

Figure 2.3 Hybridisation chain reaction protocol. (A) mRNA probes containing an initiation I1 sequence, designed against the target mRNA are hybridised to the target. (B) After hybridisation, hairpin DNA pairs are added to the solution, which bind to the I1 sequence. (C) The mechanism through which the chain reaction is propagated. The bound probe containing the HCR initiator I1 sequence triggers the chain reaction, a self-assembly of the hairpin DNA molecules, which are attached to a fluorophore for visualisation. (D) After imaging, the samples can be re-probed through incubation with DNase, which detaches the hairpin sequence and probe. Adapted from (Choi *et al.*, 2018).

2.2.5 Proliferation analysis

For the proliferation analysis in Section 4.2.3, I detected proliferating cells in two ways: First, using the Click-IT EdU Alexa Fluo 488 kit (Life Technologies, C10337). HH10-12 embryos were incubated *in ovo* by windowing, applying 0.5mM EdU, resealing and incubating at 37C for 1.5h. Embryos were then fixed and neuroepithelia dissected as described above. EdU staining was performed according to the manufacturer's instructions.

Phospo-histone H3 (pH3) labelling was performed as follows: Embryos were collected, neuroepithelia dissected, and fixed as described in Section 2.2-2.2.2. Neuroeptihelia were then washed with PBS three times, and preblocked with a blocking buffer (PBS + 1% Triton-X-100, 10% Heat inactivated goat serum (HINGS)). Neuroepithelia were then incubated overnight with primary anti-pH3 (raised in rabbit) diluted 1/1000 in the blocking buffer. The next day, the neuroepithelia were washed twice with PBS at room temperature, before being washed overnight in PBS + 10% HINGS. On the next day, secondary antibodies were added overnight in the dark, on a rocker at 4℃ (Alexa Fluo 488 at 1/500 dilution, Molecular Probes). Finally, neuroepithelia were washed twice with PBS and imaged.

2.3 Image acquisition and processing

All fluorescent images (Chapters 4-6) were processed using FIJI (Schindelin *et al.*, 2012).

2.3.1 Whole embryo imaging

Stage 10.1-10.3 embryos were imaged under a Leica dissecting microscope using a 4x objective, dorsal side down.

2.3.2 Wholemount neuroepithelia imaging

Wholemount neuroepithelia were imaged under a Zeiss Apotome 2 using a 10x objective. Neuroepithelia were imaged dorsal side down in a depression slide, immersed in Fluoroshield and captured by the Zen AxioVision software.

2.3.3 Imaging sagittal sections

Sagittal sections were imaged under a Zeiss Apotome 2 in Fluoroshield and captured by the Zen AxioVision software.

2.3.4 Confocal imaging

Membrane labelled neuroepithelia were imaged under a Zeiss LSM 980 Airyscan 2 dorsal side up in a depression slide, immersed in Fluoroshield and captured by the Zen blue software.

2.3.5 Lightsheet imaging

The HH12 embryo used for surface mesh reconstruction was imaged under a Zeiss LSM 980 Airyscan 2 confocal microscope.

2.3.6 Mesh processing

All surface meshes were reconstructed from fluorescent images of DAPI labelled nuclei using the 3D viewer plugin for FIJI (Schmid *et al.*, 2010). Meshes were exported, and processed initially in Meshmixer (Autodesk). Here, the meshes were simplified (for tractability of processing), and minor holes were filled automatically. These meshes were then imported into MeshLab (Cignoni *et al.*, 2008), smoothed, and the mean curvature of the tissue was computed. Outliers were removed by capping the range of the data, and the curvature values for each vertex were rescaled between 1 and -1 through the function

$$2 \cdot \frac{(q - q_{min})}{(q_{max} - q_{min})} - 1$$

where q is the mean curvature of a given vertex in the mesh and q_{max} and q_{min} are the maximum and minimum values of q over all vertices.

2.3.7 3-D cell segmentation

The image of the β-catenin labelled neuroepithelium was downscaled using FIJI, resized to a voxel resolution of z = 0.235um, xy= 0.15um to match the input resolution of the confocal 3-D-U-Net. Segmentation was completed using the included in the cell segmentation pipeline PlantSeg (Wolny *et al.*, 2020). Briefly, membrane predictions were generated using the pre-trained 3-D confocal U-Net (Ronneberger *et al.*, 2015), These predictions were then segmented into labelled objects (representing cells) using the partitioning method GASP (Bailoni *et al.*, 2019).

2.3.8 Morphometric analysis

Segmented cells were analysed using the FIJI plugin MorpholibJ (Legland *et al.*, 2016). The total number of voxels for each segmented object was calculated and used to filter out objects which were too large or too small and the remaining objects analysed for sphericity, surface area, and volume. Surface area was calculated using a discretised Crofton formula (Lehmann and Legland, 2012). Volume was calculated by counting the number of voxels (weighted by the size of an individual voxel). Sphericity was calculated the normalised ratio of the squared velocity over the cubed surface area, i.e.

$$\text{Sphericity} = 36\,\pi\,\frac{V^2}{S^3}$$

Chapter 3

Using image classification to characterise a novel staging system for the developing chick brain over HH10

3.1 Introduction

As described in Chapter 1, chick embryos have been used to drive our understanding of early brain development. In the chick, the rate of development is sensitive to extrinsic factors – for instance, temperature – developmental staging is based on morphology, not chronological age. Developmental stages are made with reference to the Hamburger-Hamilton (1955) staging guide, which assigns embryos to stages between HH1 (newly incubated egg) through 46 (newly hatched chick) (Hamburger and Hamilton, 1951). This classic staging guide is based on numerous morphological metrics, but for early stages when the brain is forming, relies on the number of somites - segmented pieces of tissue that are laid down at highly regular intervals on either side of the spinal cord (Palmeirim *et al.*, 1997). However, careful observational studies show that the rate/timing of development of different body structures, including the brain - is subtly uncoupled from somite number, and increasingly, researchers are attempting to develop staging classifiers for distinct embryonic regions (Boehm *et al.*, 2011; Sáenz-Ponce *et al.*, 2012; Musy *et al.*, 2018).

Recent studies in the chick show that the developing hypothalamus undergoes a significant expansion over HH10 (a period that encompasses ~5 hours), accompanied by subtle changes in its morphology (Fu *et al.*, 2017, 2019; Kim *et al.*, 2022). Molecular studies show that the expansion is accompanied by the first signs of its regionalisation into distinct functional domains (Kim *et al.*, 2022). This means that, for the accuracy of future experiments, it is important to develop a finer-grained classification of the HH10 hypothalamus. However, even after spending several weeks' dissecting, I still found it difficult to recognise the subtle changes that occur in brain morphology over HH10, and to order the chicks accordingly with confidence. I therefore asked if I could develop an image classifier. This refers to the branch of computer vision related to analysis of an image and assignment/categorising images into predefined classes.

Recently, Deep Learning (DL) based neural networks have been used extensively to extract meaningful information from images. Their application includes image classification, but also related tasks such as object localisation and segmentation classification. These techniques are increasingly becoming embedded in biomedical research (LeCun *et al.*, 2015), and have been used to powerful effect in, for example, classifying histological samples (Iizuka *et al.*, 2020), and nucleus segmentation (Caicedo *et al.*, 2019).

A common maxim for training DNN-based image classifiers is that performance improves with increasing amounts of training data (Thompson *et al.*, 2020; Jacquemet, 2021). However, in many areas of biomedical science, it is often impractical to generate large amounts of data due to cost, time, or ethics. In such cases, it is important to maximise the utility of limited data when training DNNs, but how best to do this remains an open question.

In this chapter, I address this in the context of microscopy images of HH10 chick embryos. I set out to develop a reproducible, rapid, and automatable classifier that subdivides images of embryos at different developmental sub-stages at HH10, which would provide an important tool for conducting experiments into hypothalamus development. (Note this work took place in Years 2-3 of my PhD, when access to the lab was limited).

3.2 Results

3.2.1 Somite number does not explain variation in HH10 neural morphology

Up to this point, I referred to HH10 embryos as early/middle/late, based on the number of somites (as is usual and per the Hamburger-Hamilton staging guide (Hamburger and Hamilton, 1951). However, my analysis in Section 3.2.2-3 incorporated overall brain morphology, and I next investigated to what extent I could codify this into a more concrete sub-staging system for HH10, to aid more precise investigation of hypothalamic development.

My visual inspection of images suggested that the chick HH10 brain could be divided into three sub-stages, according to the morphology of the developing prosencephalon (the forebrain), which I termed 10.1, 10.2 and 10.3. Three reference images illustrating these sub-stages are shown in Fig 3.1A. At 10.1, the developing brain is kite-shaped, the optic

vesicles (developing eyes) are shallow, and the angle of the prosencephalic neck, the anatomical landmark where the forebrain meets the posterior brain, is obtuse (Fig 3.1A, Fig 3.1B iii, left columns). At 10.2, the developing brain is hammer-shaped, the optic vesicles are more pronounced, and the posterior prosencephalon-prosencephalic neck are aligned (Fig 3.1A, Fig 3.1B iii, middle columns). At 10.3, the angle of the posterior prosencephalon-prosencephalic neck is acute, and there is a significant amount of curvature in the optic vesicles (Fig 3.1A, Fig 3.1B iii right columns).

The overall shape profiles that I picked out for my sub-staging, including the prosencephalic neck, are schematised in Fig 3.1B.

I next investigated the relationship between the sub-stages and the classic Hamburger-Hamilton staging chart (Hamburger and Hamilton, 1951), where developmental stage is determined by somite number: HH10 embryos have 9, 10 or 11 somites, and are traditionally termed HH10- (9 somites), HH10 (10 somites), or HH10+ (11 somites) (Hamburger and Hamilton, 1951). First, I quantified somite number at each sub-stage (Fig 3.2A). I observed that each sub-stage (10.1, 10.2, 10.3) can have a wide range of somites (8-12 somites) (Fig 3.2B). I also found significant differences in somite number between 10.1 and 10.3 (*** p=0.0002), and between 10.2 and 10.3 (* p=0.015), but found no significant difference in somite number between 10.1 and 10.2 (p=0.079) (Fig 3.2B). In conclusion, somite number is a poor predictor of chick HH10 brain development, underscoring the need for a finer-grained classification approach.

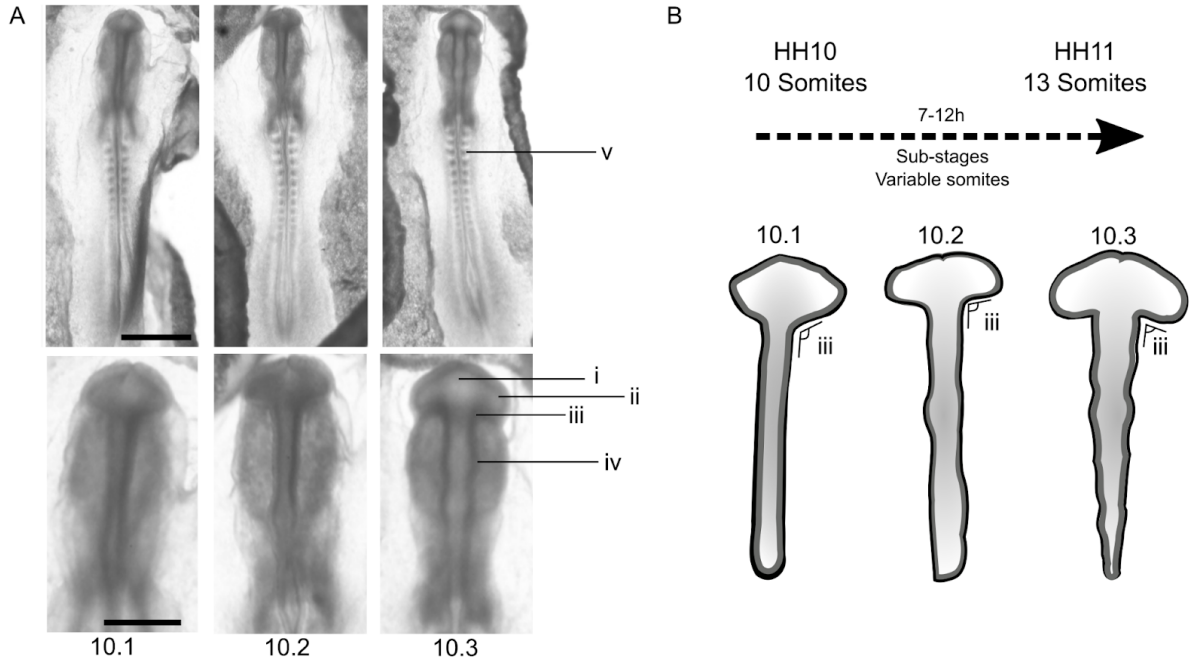

Figure 3.1. Sub-staging the HH10 chick embryo brain based on expert visual inspection of morphology. (A) Example brightfield microscopy images of stage 10 sub-stages (top panels), with close-ups of the developing brain (bottom panels). These images were used as the original reference point for ground truth labelling, and were not used as part of the DNN classifier training dataset. (i-iii) show key anatomical markers used for sub-stage labelling. (i): prosencephalon, (ii): optic vesicle, (iii): angle of prosencephalon and prosencephalic neck. (iv, v): show other anatomical features relevant to this study: (iv) somites; (v) neuromere. Scale bars: upper 1000μm, lower 500μm. (B) Schematic indicating morphological profiles of sub-stages.

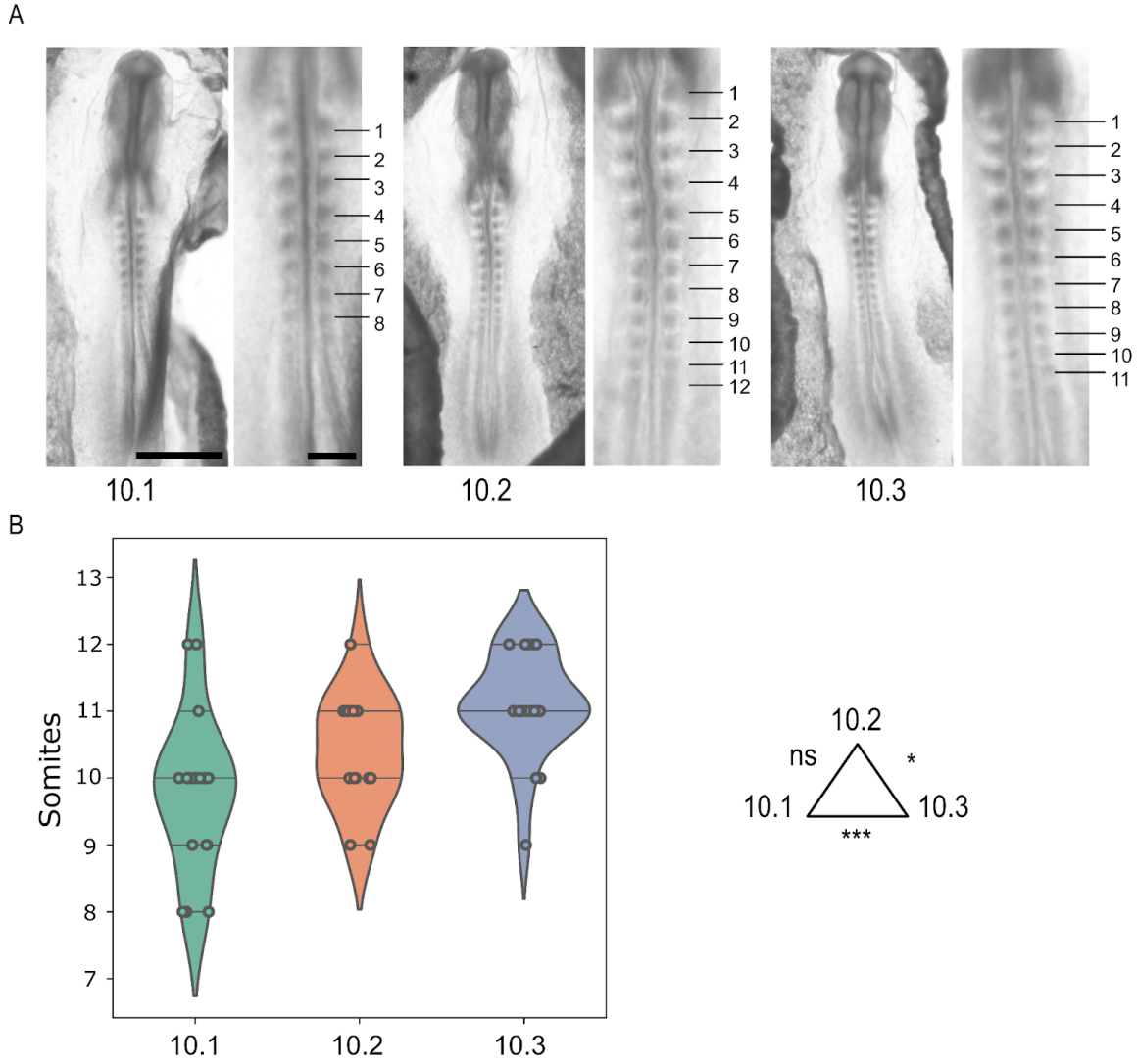

Figure 3.2 The number of somites at the 10.1, 10.2, and 10.3 sub-stages does not account for the variation seen in HH10 brain morphology. (A) Manual quantification of somite number for the reference images shown in Fig 3.1A. Right hand panels show close-ups of somitic regions. Scale bars: left 1000μm, right 250μm. (B) Violin plot of somite count across sub-stages 10.1, 10.2 and 10.3. (n= 18 10.1, 14 10.2, and 21 10.3 embryos respectively: note the data used for these quantifications were not included as training data). There are statistically significant differences in somite numbers between 10.1 and 10.3, and 10.2 and 10.3, but not 10.1 and 10.2. Despite these differences, each sub-stage can have 9, 10, 11, or 12 somites.

3.2.2 Unsupervised learning via *k*-means clustering supports three sub-stages, but performs poorly as a classifier

I next examined whether the choice of three sub-stages could be supported through clustering approaches. Inspired by an approach used to classify cell types in histology images (Krueger *et al.*, 2019), I combined principal component analysis (PCA) and *k*-means clustering. My aim was to derive an appropriate number of classes for further supervised classifiers and test the efficacy of unsupervised classifiers.

A dataset of 151 chick brain images was labelled as per reference images (Appendix Fig 1A; 54 at 10.1, 55 at 10.2, and 42 at 10.3). I then used PCA for dimensionality reduction, to ensure comprehensible and robust clustering (Ben-Hur and Guyon, 2003). To empirically determine an appropriate number of PCs, I generated a scree plot (Fig 3.3A), calculating the total variance explained by reducing the chick embryo sub-stage dataset into increasing numbers of PCs. I found that two PCs explained 81% of the dataset variance, and increasing the number of PCs further led to substantially diminishing returns.

I next clustered my data via *k*-means. To determine the number of clusters to use, I used the elbow method (Fig 3.3B): I clustered the dataset, with 1-10 clusters, and selected the ideal number of clusters as the inflection point in the within-cluster sum of squares (WCSS), where increasing *k* showed diminishing returns in WCSS. This was reached at $k = 3$, which I then visualised (Fig 3.3C). I found substantial differences in the number of images within each cluster. Between the three clusters, clusters 1-3 contained 84, 18, and 49 images respectively (Fig 3.3D). I assumed that the sub-stage most represented in each cluster was the true classification for that cluster. Thus, sub-stages 10.1, 10.2 and 10.3 corresponded to clusters 2, 1 and 3, respectively (Fig 3.3D). Therefore, the classification accuracies achieved by PCA followed by *k*-means clustering were: 10.1: 38.9%; 10.2: 41.7%; 10.3: 44.9%.

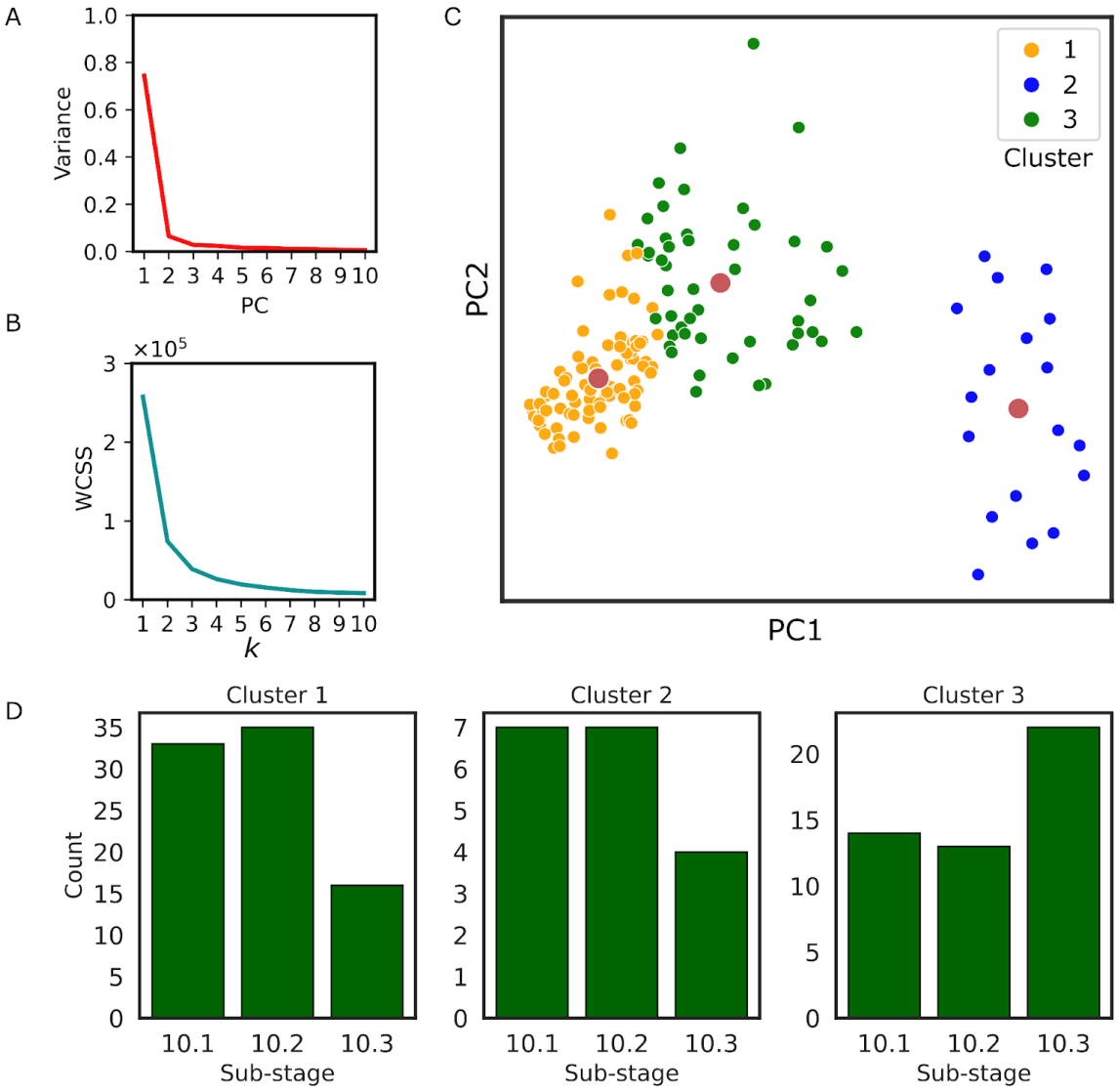

Figure 3.3 *k*-means clustering supports classification of the image dataset into three sub-stages. (A) Scree plot for principal component analysis (PCA) with increasing numbers of PCs. The elbow point is at 2 PCs, which explain 81% of the variance in the dataset. (B) The elbow method for determining the optimal number for *k*. The within-cluster sum of squares (WCSS) score is calculated for *k*-means clustering on increasing values of *k*. The optimal number of *k* is determined by the inflection point of the graph, which occurs around *k* = 3. (C) Scatter plot of the *k*-means clustered dataset, with *k* centroids (red circles). (D) Number of sub-stages present in each cluster. Despite unsupervised methods identifying three groups of images, the number of embryos in each cluster does not match the number of embryos in each labelled sub-stage of the training data.

As *k*-means clustering is unsupervised, it is difficult to determine whether the method may group data similar to a human observer. Looking beyond the classification accuracies, the

distribution of images between clusters is skewed. The ‘10.3’ cluster, cluster 3 performed best, but the accuracy and image distribution in the clusters suggest poor efficacy for classifying sub-stage (Fig 3.3D). This is likely because feature(s) are being used for clustering which are irrelevant to the true class. Whilst I confirmed that three sub-stages is an appropriate number of sub-stages to use, I next aimed to substantially improve the classification accuracy achieved by using DCNNs.

3.2.3 A DCNN trained using ResNet50 achieves a classification accuracy of up to 75% using a combined data augmentation regime of rotation & Gaussian blur

Initially, to reduce overfitting in my relatively small dataset (comprising 151 images), I tested supervised simple classifiers: random forest, support vector machine (SVM), and *k*-nearest neighbour (KNN). However, I was not able to train a sufficiently accurate classifier, with the highest individual and highest average validation accuracies achieved being 54.8% (RFC) and 38.3% (KNN) respectively (Appendix Table 1).

I therefore opted to construct a strategy which would enable me to train a DCNN based classifier. Due to the limited datasets, I carefully considered each step of training and evaluating the DCNNs. First, I considered pre-processing. As the datasets consisted of both brightfield and phase-contrast microscopy images (bright and dark backgrounds respectively), I reasoned that a useful pre-processing step would be to normalise the histograms of each image.

Next, I augmented the dataset through transformations, which both expanded the number of datapoints for training, and normalised skewed image features unimportant for classification. For instance in microscopy images, subject orientation often varies greatly. Henceforth, I refer to the dataset augmented with rotations as the baseline.

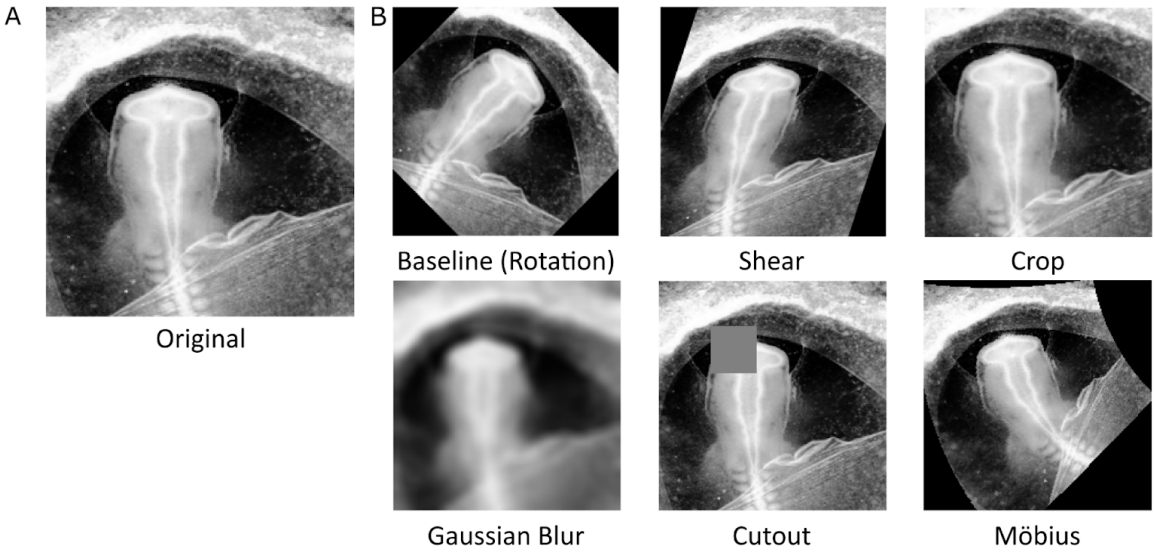

Figure 3.4 Examples of different augmentations on an image of a 10.2 sub-stage embryo. (A) An example image of a 10.2 embryo from the dataset (base), with (B) the augmentation regimes tested for classifier training: geometric (e.g. rotation), photometric (e.g. contrast), and complex (e.g. cutout) augmentations.

I then determined my cross validation approach. I deemed that the widely used hold out validation, (where some amount of the dataset, often 20%, is unavailable for training), was unsuitable for my purposes, as with a limited dataset it is key to use every data point possible for training. I verified this empirically, showing a large amount of variability between highest validation accuracy achieved by models trained on the brain dataset with hold out validation (Appendix Table 4). Therefore, I used *k*-fold cross validation with $k = 10$, (i.e. 15-16 images per fold, using the whole dataset for training) for all subsequent training.

For training a DCNN classifier, I first tested training using the widely used network architectures from InceptionV3 (Szegedy *et al.*, 2015) and ResNet50 (He *et al.*, 2016). These two neural networks have achieved high classification accuracies on ImageNet, a large database of over 14 million images. I aimed to understand to what extent these established architectures could be used with limited microscopy data.

I then trained, using the InceptionV3 and ResNet50 architectures (Appendix Tables 2-3), on a variety of augmentation regimes (Fig 3.4). Generally, InceptionV3 performed poorly, with similar averages across various data augmentations, and a maximum validation accuracy of 60.5%. This is more successful than *k*-means, which was 44.9% (Fig 3.3D), however the average validation accuracies achieved by InceptionV3 are in the range of 44-46%, so that

overall, performance is similar to that achieved through *k*-means. With ResNet50 training, I saw a marked improvement in validation accuracies over InceptionV3 and the *k*-means clustering accuracy across all augmentations (except for crop, which only improved by an average of 3%). The baseline & Gaussian blur augmentation regime (hereafter referred to as Gaussian blur) had the highest average validation accuracy, (69.2%), and highest fold accuracy (75.9%). Additionally, this regime achieved the second lowest standard deviation, an important metric in light of a limited dataset (Appendix Table 3). Taken together, these results suggest that training with commonly-used image classification architectures is not effective in classifying small microscopy datasets. However this underperformance was substantially ameliorated by data preprocessing, and the Gaussian blur regime.

3.2.4 A bespoke neural network classifies developmental sub-stages of a small dataset of chick embryo brains with up to 90.9% accuracy

ResNet50 has been used successfully for image classification on datasets other than ImageNet, for example on ChestX-ray14, a dataset of X-ray images (Baltruschat *et al.*, 2019). ChestX-ray14 is substantially larger than my dataset, comprising 112,120 images. Therefore, considering that I did little fine-tuning of the hyperparameters of ResNet50, and that ResNet50 was constructed for large datasets, ResNet50 performed surprisingly well (up to 75.9%) when trained on the brain data. However, this performance leaves room for improvement so I set out to understand whether a bespoke network would achieve even higher classification accuracies. I aimed to incorporate domain expertise, by specifically considering the types of problems encountered in developmental biology datasets.

I constructed a model with a wide, VGG-16 block-style architecture (Fig 2.1), which has been successful in image classification (Simonyan and Zisserman, 2014). I used Bayesian optimisation (Appendix Table 6) and examples from the applied deep learning literature to tune the hyperparameters (Zhang and Mitliagkas, 2019; Margapuri *et al.*, 2020). I then determined the most useful and robust augmentation regimes (Table 3.1). The baseline usually performed well, surpassing my best ResNet50 results with an average validation accuracy of 76.2%. However, for each fold, one of the various augmentations always had higher validation accuracy than the baseline. The poorest performing augmentation was baseline & crop, with an average validation accuracy of 47.1%.

Aug	Fold											
	1	**2**	**3**	**4**	**5**	**6**	**7**	**8**	**9**	**10**	**Avg.**	**SD**
1	69.3	68.1	79.3	78.9	72.6	84.8	74.6	68.0	90.9	75.2	76.2	7.5
1 Sharpened	78.7	80.9	77.0	70.2	80.2	80.7	70.7	76.7	90.0	76.9	78.2	5.6
1 + 2	68.9	75.5	78.8	79.8	75.1	84.5	78.8	69.1	90.3	83.1	78.4	6.7
1 + 3	75.7	67.1	58.2	64.2	66.2	67.4	68.6	36.6	79.6	68.0	65.2	**11.6**
1 + 4	81.0	73.8	80.6	**79.1**	**81.7**	**86.9**	**79.0**	71.9	88.9	81.9	**80.5**	**5.1***
1 + 5	73.6	76.6	79.9	76.7	76.9	86.1	78.0	68.1	**91.7**	83.3	79.1	6.6
1 + 4,5 RC	**86.3**	**81.0**	78.2	74.2	77.6	82.2	73.2	**77.6**	89.0	83.2	80.3	**5.1***
1 + 2,4,5 RC	84.6	75.5	**82.1**	70.1	81.2	83.1	75.9	77.1	90.9	**84.2**	**80.5**	5.9
Fold Avg.	70.5	69.2	74.7	73.7	72.3	79.5	71.8	66.7	83.2	74.6		

Table 3.1 Augmentation exploration of the brain dataset using the bespoke model. I explored the data-space using *k*-fold cross validation, the individual fold validation accuracies that each network achieved are shown in columns 1-10, and the averages and standard deviation of these accuracies is shown in the rightmost columns. As a baseline processing step, all images were rotated 15 times, at equally spaced degrees. I then tested augmentations on top of this baseline, before a final test whereby each image was randomly augmented. Augmentations (Aug) as follows: (1) rotation (baseline); (2) shear; (3) crop; (4) Gaussian blur; (5) cutout; (RC) random combination of rotation + cutout, or shear, or blur. Highest validation accuracies for each fold, highest average for each augmentation (Avg.), and lowest standard deviation (SD) are shown in bold. (1 Sharpened), baseline with a preprocessing sharpen filter; (1+ 4,5 RC) random combination of baseline, Gaussian blur, and cutout.

The best performing individual augmentation was baseline & Gaussian blur, with the highest average validation accuracy of 80.5% and the lowest standard deviation (excluding crop, which performed substantially below baseline). Baseline & cutout provided the best individual fold validation accuracy, of 91.7% at fold 9 (vs. Gaussian blur 88.9%). Despite baseline & cutout achieving the highest individual fold validation accuracy, I conclude that

baseline & Gaussian blur overall performed best, as it achieved the highest validation accuracy on folds 4-7.

I also tested the efficacy of Möbius transformations, which have proven successful in other contexts (Zhou *et al.*, 2021) but are untested for microscopy image classification. I reasoned that Möbius transformations could introduce the DCNN to common microscopy artefacts, e.g. tissue bending during sample preparation. However, the baseline and Möbius transforms performed more poorly than the baseline alone, and that sparse inclusion of Möbius transformations also decreased validation accuracy (Appendix Table 5).

My cross validation (Table 3.1) shows dataset partitions that lead to low accuracies, indicating that these partitions contain images with features that are not shared with the images in higher scoring partitions. These are likely artefacts introduced in chick dissection/preparation or imaging, e.g. due to tearing of the fragile tissue. As such, I sought to mitigate this invariance. Whilst the good performance of the baseline is intuitive, both the shear and Gaussian blur regimes also achieved high validation accuracies. For shear, I reasoned that this could reflect increasing the robustness of the network by introducing it to distortions similar to the types of tissue deformations routinely introduced in chick dissection/preparation or imaging Similarly, Gaussian blur could increase robustness by introducing the DCNN to data that resembles out-of-focus images, a common microscopy artefact.

To test whether Gaussian blur is having this effect, I applied the inverse operation by sharpening the images during preprocessing before the baseline augmentation (Table 3.1, 1 Sharpened). I found that sharpening increased average validation accuracy from 76.2% (baseline) to 78.2% (baseline sharpened). Further, I saw that poorly performing baseline folds (e.g. 2 and 8) had substantially higher validation accuracies. However, the results from sharpening as a preprocessing step do not entirely explain the discrepancy in validation accuracies between the baseline & Gaussian blur. This suggests that Gaussian blur is not only introducing the DCNN to out-of-focus images, but could be masking tissue tearing artefacts through smoothing of geometric lines or curves in the tissue structure. Moreover, these augmentations may be assisting the network to focus on a true sub-stage characteristic, rather than features arising from biological inter-sample variation. This suggests that these poorly scoring dataset partitions contain features that lead to an inaccurate classification, but this can be mitigated with reasoned preprocessing and augmentation.

Since different augmentations had scored highest on different folds, I next tested different combinations of these augmentations as an approach to reduce variability (Table 3.1, 1+4,5 RC, 1 + 2,4,5 RC). I identified an informed combined regime as a useful approach when dealing with high variability, small datasets. For example, folds 2 and 8 had the lowest average validation accuracies across all augmentations. For both, mixing the baseline with shear, Gaussian blur, and cutout resulted in substantially higher validation accuracies, allowing the network to learn 'difficult' features of the images.

In summary, I found training a bespoke neural network suits my classification problem, and that reasoned augmentations enhance network performance, achieving >90% validation accuracies, despite a small dataset. Whilst the focus of this thesis is on hypothalamus development, I include below an analysis of developing limb data, as a test of whether my classification strategy can also be applied straightforwardly to other limited, developmental biology datasets.

3.2.5 The bespoke neural network classifies a small dataset of developing chick limbs with up to 94.4% accuracy

I next set out to see if my pre-processing, architecture, and data augmentation approach could be applied to other small datasets. For this, I used published data comprising 269 developing chick limb images (Towers *et al.*, 2008a), separated into two labelled categories: 'control' (corresponding to the normal limb development), and 'treated', where growth had been transiently inhibited by the drug trichostatin A. I sought to determine whether my approach could be used to train a DCNN to classify control versus treated limbs.

Aug	Fold											
	1	**2**	**3**	**4**	**5**	**6**	**7**	**8**	**9**	**10**	**Avg.**	**SD**
1 (Flipped)	89.5	**87.0**	83.1	88.0	**91.0**	90.0	91.3	**94.4**	92.9	89.2	89.6	3.2
1 + 2	93.1	80.7	**88.2**	**91.1**	90.1	81.5	**93.6**	92.9	**94.4**	88.9	89.5	4.9
1 + 3	89.1	77.4	83.2	85.9	80.1	81.2	85.2	86.1	87.3	86.9	84.2	3.7
1 + 4	91.1	85.3	82.2	90.1	90.4	**93.6**	90.5	93.0	92.4	90.2	**89.9**	3.5
1 + 5	**93.2**	81.4	88.1	88.6	90.1	85.1	90.7	93.2	93.6	89.8	89.4	3.9
1 + 2,4,5 RC	92.0	84.5	87.5	89.4	90.4	85.5	91.4	93.1	93.6	**91.4**	**89.9**	**3.1**
Fold Avg.	91.3	83.7	85.4	88.9	88.7	86.2	90.5	92.1	92.4	89.4	88.7	

Table 3.2 Augmentation exploration of a limited, developing limb dataset using the bespoke model. I explored the data-space using *k*-fold cross validation, the individual fold validation accuracies that each network achieved are shown in columns 1-10, and the averages and standard deviation of these accuracies is shown in the rightmost columns. As a baseline processing step, all images were rotated 15 times, at equally spaced degrees and flipped. I then tested augmentations on top of this baseline, before a final test whereby each image was randomly augmented. Augmentations (Aug) as follows: (1) rotation & flip (baseline); (2) shear; (3) crop; (4) Gaussian blur; (5) cutout; (RC) random combination of rotation + cutout, or shear, or blur. Highest validation accuracies for each fold, highest average for each augmentation (Avg.), and lowest standard deviation (SD) are shown in bold.

I set up the problem in a similar fashion to the brain classification, with minor changes as warranted by the switch from a multi-class to a binary classification problem. In addition to the baseline augmentation regime, I introduced flipped images along the horizontal axis, as the experimental protocol in (Towers *et al.*, 2008) used the left limb as control, and treated the right limb. The validation accuracies achieved were generally higher than for the brain classification, especially across the baseline, which for folds 2, 5, 8 achieved the highest validation accuracies -- something not seen in the brain classification (Table 3.2). However, the mixed regime performed best, with the joint highest average classification accuracy and lowest standard deviation of all the regimes tested. Additionally, the mixed regime only marginally underperformed the fold average once at fold 5. Thus, my strategy of reasoned

data augmentations, derived for training classifiers on the chick brain dataset, extended well, classifying another limited microscopy dataset of developing limbs with high accuracy.

3.2.6 Saliency maps identify novel class-specific features

I next performed saliency analysis (Simonyan *et al.*, 2014) on the brain datasets, to determine to which region(s) of the images my classifiers were sensitive. I selected the baseline model, and a range of models trained on different augmentation regimes (Table 3.1), and first visualised their saliency maps for test images of each brain sub-stage (Fig 3.5Ai-vi, Fig 3.6Ai-vi, Fig 3.6Bi-vi). The baseline model focused on the brain at 10.2, with scattered attention peripherally. (Fig 3.5Ai). This was reflected in the 10.1 maps (Fig 3.6Ai), but not the 10.3 maps (Fig 3.6Bi). Models trained with Gaussian blur (Fig 3.5Aii), cutout (Fig 3.5Aiii), and shear (Fig 3.5iv) honed focus substantially, leaving several focal points (compare Fig 3.5Ai with Fig 3.5Aii-iv). Similar effects were seen in the 10.1 and 10.3 maps (Fig 3.6Aii-iv, Fig 3.6Bii-iv). Gaussian blur also introduced focus on the 10.2 prosencephalic neck (Fig 3.5Aii). I included crop as a negative control, as it showed the worst performance of all augmentations tested (Table 3.1). Crop either produced very little focus (Fig 3.5Avi) or scattered attention throughout the image (Fig 3.6Avi, 3.6Bvi). These results confirm that the choice of augmentation results in different image features being picked out by a classifier, but also that biologically relevant features e.g. the prosencephalic neck can be focused on after augmentation with Gaussian blur.

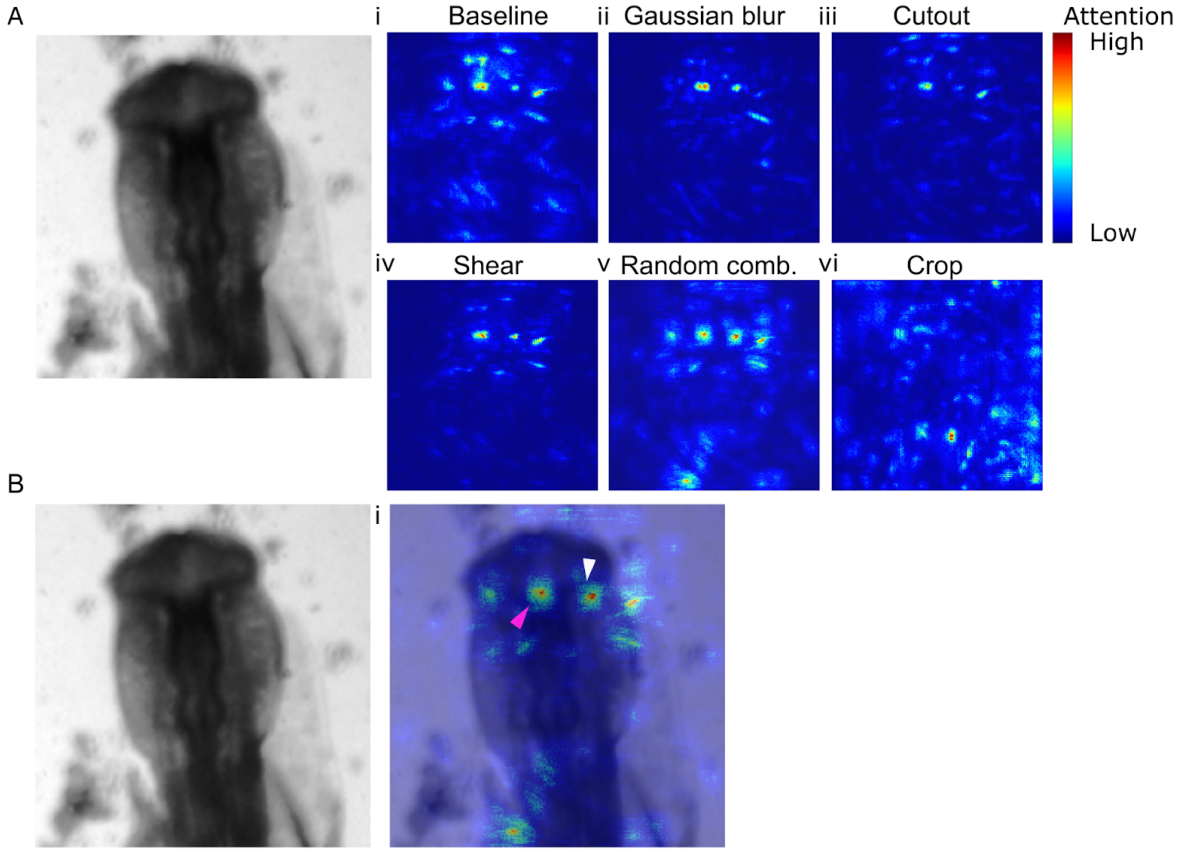

Figure 3.5 Saliency maps of a 10.2 substage identify focal differences between models trained on different augmentations. (A) A test 10.2 image not used in training/validation of any DCNN. (i-vi) Saliency maps generated from training a DCNN on the baseline rotationally augmented data (i), with a further augmentation (ii-vi, listed above each image). Baseline (i) leads to a large amount of attention spread over the prosencephalon. Gaussian blur (ii) cutout (iii), and shear (iv) increase focus to a few focal points on the prosencephalon. The maps generated by the augmentations i-v contrast with crop (vi). This performed the worst of all the augmentation regimes, and has very little focus on the prosencephalon. (B) (i) The saliency map generated by the combined regime as shown in (Av), overlaid with the test 10.2 image. The combined regime increases the focus on points introduced by the various augmentations, and the focus is highest on the region of the embryo (i, magenta arrow) central to the prosencephalic neck (white arrow), also a region of high focus. The combined regimes of various augmentations increase the focal attention. Highest focal points are the centre of the prosencephalic neck (magenta arrow) and the junction of the prosencephalon-prosencephalic neck (white arrow).

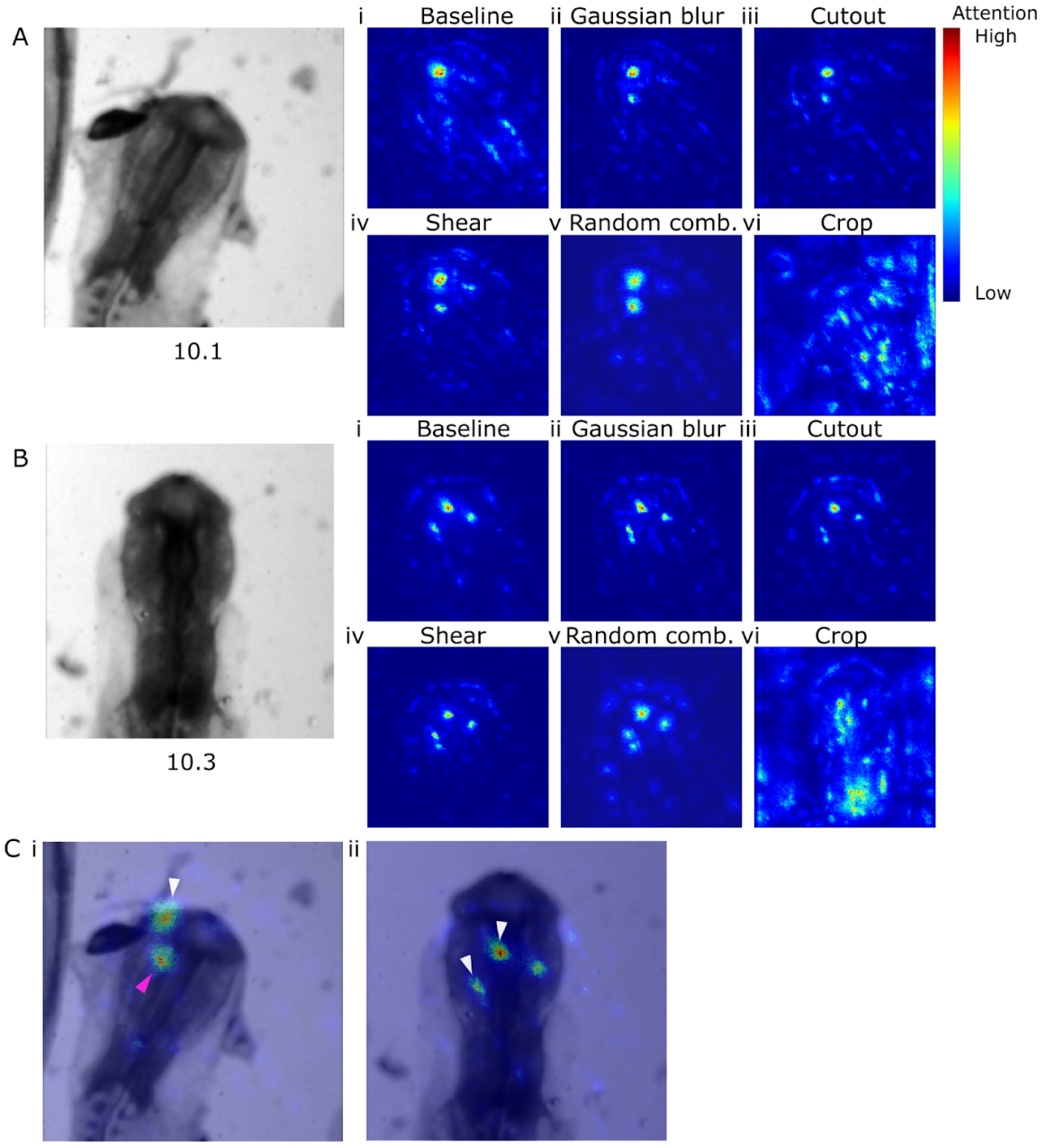

Figure 3.6 Saliency maps of 10.1 and 10.3 substages identify focal differences between models trained on different augmentations. (A-B) Test images of 10.1 and 10.3 embryos. (i-vi) Saliency maps generated from (A-B) and assessed through models trained on different augmentation regimes, following the bespoke architecture (from Table 3.1), trained on the baseline rotationally augmented data, with a further augmentation (listed above each image). Random comb. refers to a model trained on the baseline and a random combination of Gaussian blur, cutout, and shear augmentations. The random combination results in attention which is discrete and focused e.g. (Av), (Bv). Conversely, models trained on baseline & crop show scattered attention, where the attention map shows high attention pixels scattered throughout the image can be seen (Avi,Bvi). A scattered attention map

suggests that the model is focusing on various image features unrelated to the subject. (C) Saliency maps as in (A,B v) overlaid with the test image. Here, for 10.1, the model focused most on the angle of the prosencephalic neck (Ci magenta arrow) and the anterior prosencephalon (Ci white arrow). For 10.3 the focus was shifted to more posterior regions of the embryo, including the neuromeres (Cii, white arrows).

I next tested the DCNN trained on the combined regime, applying either Gaussian blur, cutout, or shear over the baseline per image. This regime produced a similar average validation accuracy and standard deviation to Gaussian blur (Table 3.1, the highest scoring individual augmentation). The saliency maps show large focal points on the centre of the prosencephalic neck (Fig 3.5Bi, magenta arrow) and the junction of the prosencephalon-prosencephalic neck (Fig 3.5Bi, white arrow). I also saw a 'combined map' effect, where the combined regime produced focus resembling larger versions of focal points from the individual augmentation regimes (Fig 3.5A, Fig 3.6Av, 3.6Bv). In particular I found clear differences in the focal points paid to each class.

For 10.1, the combined augmentation regime-trained DCNN focused on the prosencephalic neck and the prosencephalon (Fig 3.6Ci, magenta and white arrow respectively), while for 10.3, focal points were more posterior and confined to the neuromeres (structures delineating future brain regions) (Fig 3.6Cii, white arrows). Contrastingly, for 10.2 the focus was spread over the prosencephalon and more peripherally (Fig 3.5B), indicating that this sub-stage shares similarities with both 10.1 and 10.3, being between them in developmental time. Exemplifying the utility of my approach, I found that the sub-stage specific features of 10.3 focused on these more posterior regions (compare Fig 3.6Cii and Fig 3.5B, Fig 3.6Ci), which were not explicitly part of the labelling criteria.

In summary, the brain classifier saliency maps confirmed the labelling intuitions (for the 10.1 and 10.2 sub-stages), and provided insight into novel morphological features that best defined the sub-stages, outside of any preconceptions.

I then generated saliency maps in a similar fashion for the limb classifier. For the control limb my baseline augmentation regime produced a tight focus on the posterior distal tip (Fig 3.7Ai). Gaussian blur and shear introduced some focus more anteriorly in the limb (Fig 3.7Aii, iv). Cutout produced a similar map to baseline, albeit with slightly reduced focus (Fig 3.7Aiii). Whilst crop performed relatively better than in the brain classification, I again included it for comparison, as it continued to underperform every other augmentation regime. The crop saliency map resembled the baseline, but with a reduced focus (Fig 3.7Avi).

For the treated limb, I saw more attention paid to the anterior proximal edge in the baseline, Gaussian blur, and shear regimes (Fig 3.7Bi, ii, iv). Again this was reduced slightly in the cutout map (Fig 3.7Biii). Shear introduced a focal point more distally, whilst retaining the focal points that the other maps exhibited. Again, crop produced very little focus, with one large point at the corner, likely reflecting the expanded field of view of the test image compared to the cropped augmentation regime.

I next tested the combined regime, augmenting each baseline regime image with Gaussian blur, shear, or cutout. For both the control and treated limbs, I saw a large increase in focus from this regime (Fig 3.7Bv). Intuitively and similar to the brain saliency maps, I saw a combined map effect - where the combined regime introduced focal points from each other augmentation regime. Additionally, I see clearest in the combined regime saliency maps that the classifiers define the two classes based on different aspects of the tissue morphology. For the control limb, I saw this regime focus on the overall width of the limb (Fig 3.7Ci upper white arrow, Fig 3.7Bi) and the posterior distal edge (Fig 3.7Ci, lower white arrow). For the treated limb, I saw a focus on a more anterior distal edge (Fig 3.7Cii, magenta arrow), as well as a strip of focus running from proximal to distal, suggesting that the width of this axis in the limb was important in classification.

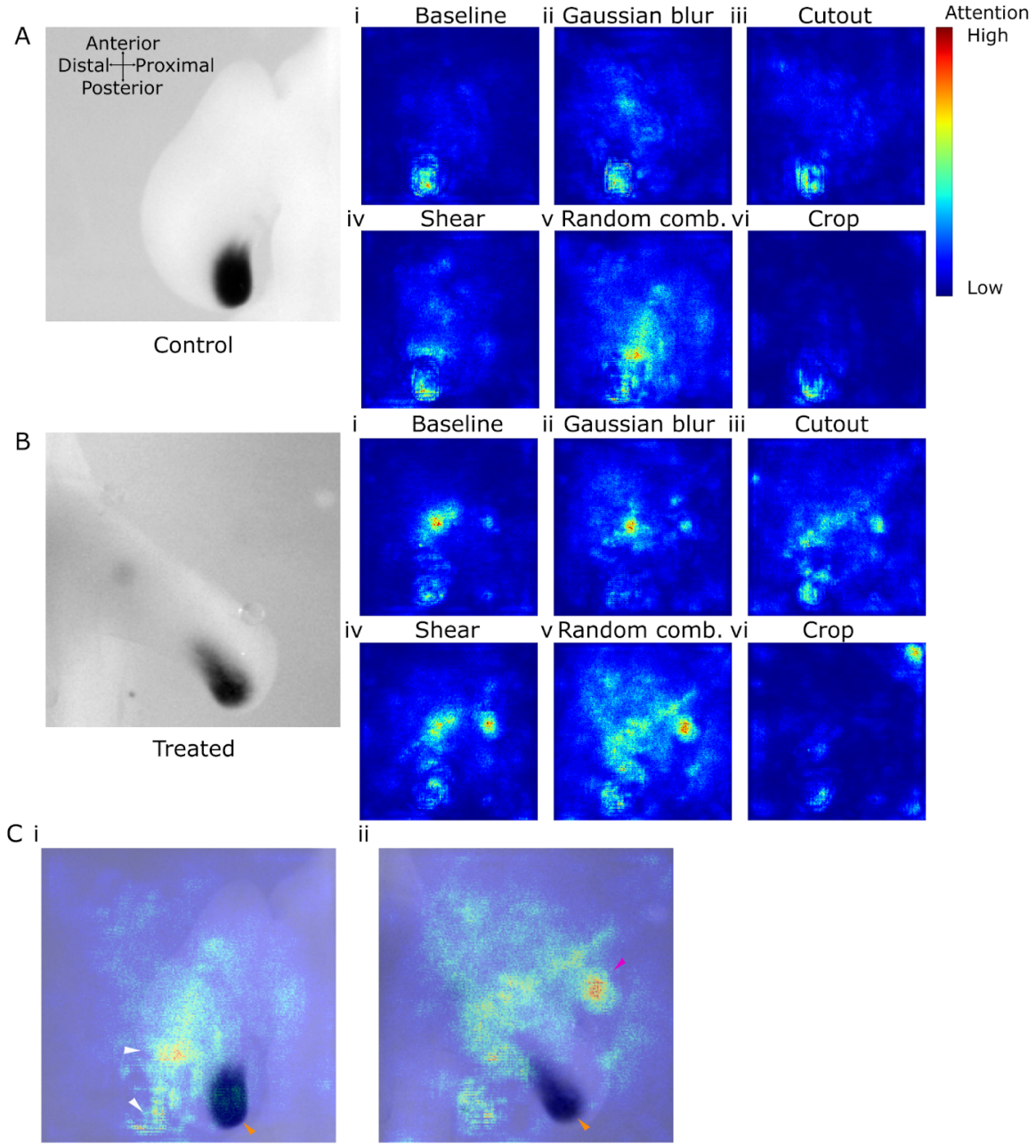

Figure 3.7 Saliency maps from images of developing chick limbs identify morphology as a class-defining feature. (A) A test control limb image not used in training/validation of any DCNN. (i-vi) Saliency maps generated from training a DCNN on the baseline of flipped and rotationally augmented limb data (i), with a further augmentation (ii-vi, listed above each image). Baseline (i) leads to a tight focal point on the posterior distal edge of the limb. Gaussian blur (ii) cutout (iii), and shear (iv) share this focal point, but for gaussian blur and shear there are focal points added more anteriorly and toward the centre of the developing limb. The maps generated by the augmentations i-v contrast with crop (vi) which performed the worst of all the augmentation regimes for the brain classification, and has reduced focus from baseline. (B) (i-vi) A test image with augmentations as in (A) but with a treated limb.

Baseline (i) exhibits a large focal point in the proximal anterior portion of the limb, with a smaller, posterior distal point. Gaussian blur (ii) resembles baseline, but with smaller additional points of focus introduced throughout the limb. Cutout, and Shear (iii, iv) produce similar saliency maps, with attention paid to both posterior and anterior proximal regions, as well as some posterior distal regions. Again, crop (vi) contrasts with the other saliency maps, in that focus is substantially reduced over Baseline alone. Finally, the combined regime for both control and treated limbs (C) increases focus throughout the limb. For control, the focus is throughout the posterior distal tip, with the highest attention paid to the edges of the limb (C i, white arrows). For the treated limb, I see that focus is generally more anterior and proximal, with the highest focal point being the distal long edge of the developing limb (C ii, magenta arrow).

Surprisingly, despite the fact that both the control and growth inhibitor-treated limbs had been processed to visualise the expression of the *Sonic Hedgehog (SHH)* gene (Fig 3.7Ci-ii, orange arrows, Fig 3.8A-Bi), the classifier did not pay attention to these regions of the image. This is important, as SHH is intricately linked to developing tissue fate and growth in the limb (Groves *et al.*, 2020) (and other contexts). In the limb dataset, there were images which have no SHH expression.We also found that *SHH* presence was not a classifying feature in test cases where *SHH* was switched off (Fig 3.8A-Bii).

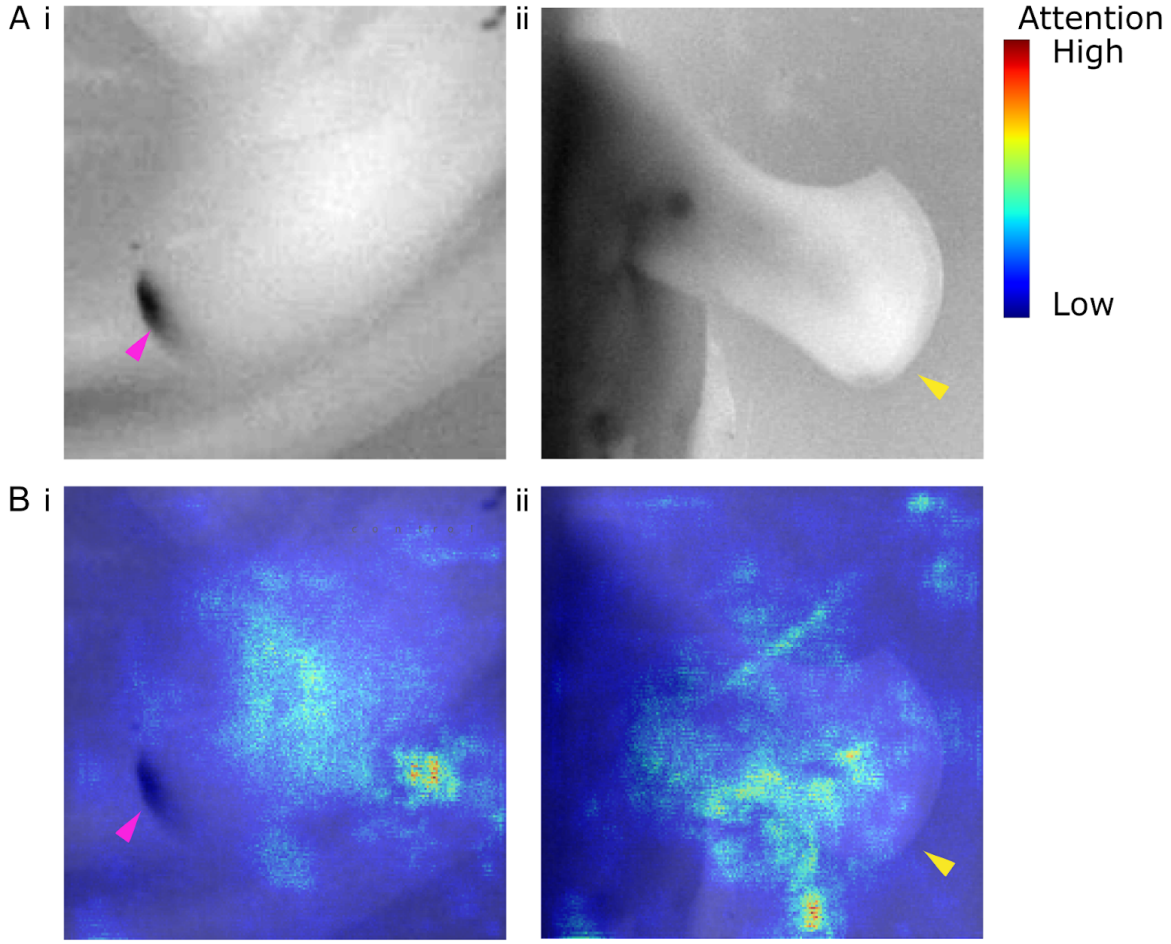

Figure 3.8 SHH expression is not used to classify between control and treated limbs. (A) Test images of control (i) and treated (ii) chick embryo limbs, not used in the model training/validation pipeline. The control limb has expression of SHH (i, magenta arrow), whilst the treated limb does not (ii, yellow arrow). (B) Saliency maps generated using the test images in (A), classified using the same mixed augmentation model used to generate Fig 4C i-ii. The network pays little attention to the SHH expression (i, magenta and ii, yellow arrows), instead focusing on the broader shape of the limbs and specific points of curvature.

These results suggest that rigorous examination of classifier attention gives insight not only into data processing and augmentation efficacy, but also into the features of the embryo which most define the classification, with the potential for insights which help examine the relationship between morphology and other biological factors, including gene expression.

3.2.7 Classification of an independent test dataset

The classification accuracy results presented thus far in this chapter were prediction accuracy on multiple folds of the entire training dataset. The saliency analyses presented in Section 3.2.6, however, were conducted on samples unseen during any training. To understand the extent that the trained models generalise to data outside of the training dataset, I next set out to test classifiers trained on different augmentation regimes on a separate, independent dataset.

To do this, I used the dataset generated for the analysis in Section 3.2.1. This comprised 57 brightfield images of 10.1-10.-3 sub-stage embryos. I then evaluated the models trained in Section 3.2.4, with ten separate models trained per augmentation regime, and took the average classification accuracy across these (Table 3.3). The classification accuracy on this test dataset was generally poor, with the previously concluded best performing augmentation regime (combination of baseline with cutout and gaussian blur) achieving at best 32.1% test accuracy.

This was surprising, as the accuracy during training was generally high (Table 3.1). There are several possible explanations for the poor test accuracy. Firstly, all images in the test dataset were taken using a brightfield microscope. The training dataset did contain brightfield images, but at a low frequency (ratios of 6/54 at 10.1, 6/55 at 10.2, and 4/42 at 10.3 brightfield/phase contrast images). By retrospectively inspecting the data this way, I saw that not only is there a low representation of the test data modality in the training dataset, but also that the representations are imbalanced.

There are two potential solutions to this that future work should seek to address. Firstly, combining the 57 brightfield images of the test dataset into the training dataset, and then randomly holding back a proportion of that mixed dataset as a new test dataset. This would create a more balanced proportion of phase contrast vs. brightfield images in the test dataset, and the trained models would similarly be more robust to inference on non-phase contrast images.

Aug	AVG Accuracy (%)
1	30.7
1 + 2	**32.8**
1 + 3	29.3
1 + 4	32.1
1 + 5	**32.8**
1 + 4,5 RC	32.1

Table 3.3 Classification accuracy on an independent test dataset for brain classification, using the bespoke models trained in Section 3.2.4. I tested the models that were trained during *k*-fold cross validation, and averaged their prediction accuracy (AVG). Models trained with the following augmentations (Aug) are as follows: (1) rotation (baseline); (2) shear; (3) crop; (4) Gaussian blur; (5) cutout; (RC) random combination of rotation + cutout, or shear, or blur. Highest validation accuracies for each fold, highest average for each augmentation (Avg.), and lowest standard deviation (SD) are shown in bold. (1 Sharpened), baseline with a preprocessing sharpen filter; (1+ 4,5 RC) random combination of baseline, Gaussian blur, and cutout.

Secondly, future work should aim to resolve imbalanced classes in the training dataset (i.e. the imbalance from fewer 10.3 samples than 10.1 or 10.2), and one way to do this could be making use of over-sampling techniques, which balance the dataset by favourably increasing the number of (in this case) 10.3 samples until it matches the number of 10.1/10.2 samples. One particularly promising approach would be to use the Synthetic Minority Oversampling Technique (SMOTE) (Chawla *et al.*, 2002) on the 10.3 samples which are misclassified, as these likely represented ‘confusing’ samples which are near the boundary between two classes

3.3 Summary

The aim of this chapter was to characterise a more fine-grained staging system for the HH10 chick brain, which is an important developmental stage for hypothalamus development, where many dynamic events occur rapidly (discussed in Chapter 1). To address this, I first had to determine the relationship between somite number and overall brain morphology, finding that somite number was an unreliable predictor of sub-stage. I then developed an image classifier to automatically sub-stage an embryo given a picture of its developing brain. This is useful, as it both speeds up analysis, and ensures consistency of staging between experiments. To do this, I had to perform a systematic exploration of various methods to ameliorate the limited dataset, finding that using my experimental/biological domain expertise helped to design effective strategies.

Over HH10, the developing forebrain undergoes substantial morphological changes. At 10.1, the brain is kite-shaped, and the angle of the prosencephalic neck obtuse. At 10.2 the optic vesicles have extended laterally, resulting in a hammer-shaped brain, and the prosencephalic neck angle is now more right-angled. Finally, at 10.3 the optic vesicles have both extended laterally and curved substantially, and the apex of their curve is in-line with the prosencephalic neck, the angle of which is now acute.

Up to this point, the images of the developing brain have been of the overall profile, and typically the hypothalamus is obscured due to perspective or surrounding opaque tissue. Therefore, the overall gross morphological changes occurring during my sub-stages were a proxy for changes in hypothalamic development. Now that I was confident that I could reliably sub-stage an embryo at HH10, and that this staging system could easily be used by others, I set out to explicitly link my sub-stages to changes in hypothalamic morphology and molecular expression (Chapters 4 and 5).

Chapter 4

Characterisation of chick hypothalamus morphology over HH8-HH12

4.1 Introduction

As discussed in Chapter 1, recent work in chick has significantly advanced our understanding of hypothalamus growth and development (Fu *et al.*, 2017; Kim *et al.*, 2022). These studies overturned the working model that adult hypothalamic neuronal populations are generated through isotropic growth of embryonic progenitor cell populations, instead suggesting an anisotropic growth model involving simultaneous tangential migration and specification of neuronal precursor cells from a *SHH/FGF10*-expressing progenitor population(s). Neither study, however, examined the consequences of anisotropic growth on the development of the 3-D morphology of the hypothalamus. Further, although the studies performed a cursory analysis of the expression patterns of *SHH, FGF10* and *BMP2*, neither investigated their expression patterns in detail, nor paid attention to changes in their expression that might occur over the stage 10 sub-stages (10.1, 10.2, and 10.3) that I characterised in Chapter 3.

Recently, researchers have been attempting to integrate mechanical events and morphogen signalling in other areas of embryonic development in order to develop novel morphogenetic theories of development (Collinet and Lecuit, 2021; Valet *et al.*, 2022). As discussed in Chapter 1, the mid-embryonic/adult hypothalamus has a complex 3-D morphology. However, the morphogenetic events underlying this morphology are not well characterised. I hypothesised that morphogen-like signalling ligands might play an important role in the development of the 3-D morphology of the hypothalamus.

As outlined in the Introduction, the hypothalamus begins to form around HH8-HH10. I therefore sought to first characterise the 3-D morphodynamics of the developing hypothalamus at stages HH8-HH12 (this Chapter), and to then relate these to the spatio-temporal expression of key morphogen genes, including *SHH*, *FGF10*, and *BMP2*, and to SHH signal pathway components (Chapter 5). These were chosen as they are known to be expressed in the early hypothalamus (Dale et al., 1997; Manning et al., 2006; Fu et al.,

2017; Kim et al., 2022) and to be important for early hypothalamus development. SHH and FGF10 are critical to the induction, anisotropic growth, and specification of hypothalamic progenitors, which occur over HH8-HH12 (Dale *et al.*, 1997; Fu *et al.*, 2017), while BMPs regulate *SHH* in the hypothalamus (Manning *et al.*, 2006). My overall goal was to determine whether their expression profiles might predict early tissue morphology.

I began with cross-sectional data (Fig 4.1A), which I then planned to reconstruct in 3-D. However, I found that the variability in the precise orientation of the sample, and damage caused by slicing, affected my ability to align and reconstruct these in 3-D. As a result, I then focused on wholemount 3-D imaging of isolated neuroepithelium. This provided a robust and reproducible picture of morphology in the developing chick brain and hypothalamus. Further, through this analysis I characterised a novel, complex morphology of the developing chick prosencephalon, which includes the developing hypothalamus. For the sake of brevity I include only the initial analysis of sagittal sections, and focus primarily on analyses of the 3-D wholemount images in Section 4.2.

4.2 Results

4.2.1 Dissection of the chick neuroectoderm reveals ventral folds

I initially set out to visualise the morphology of the developing hypothalamus at HH10, a critical stage of hypothalamus development, when regionalisation is about to begin (Fu *et al.*, 2017, 2019; Kim *et al.*, 2022).

While the neuroepithelium along the length of the neural tube at HH10 is largely cylindrical, the tissue in the vicinity of the developing hypothalamus is more complex, and in fact a fold has previously been noted in 2-D sagittal sections (Fig 4.1B, adapted from (Fu *et al.*, 2017)). To assess if this fold is characteristic of HH10 embryos, I re-examined the sagittal profile of the developing hypothalamus at HH10, incubating sections with DAPI as a proxy for overall tissue morphology (see Section 2.2.1). A prominent fold was detected in all HH10 embryos (n = 4). I termed the prominent fold the *anterior fold* (A-fold; Fig 4.1B-C, green square bracket; magenta arrowheads mark posterior limit of fold) and I termed the tissue anterior to the A-fold the *ventral face* (V-face; Fig 4.1B-C, blue square brackets). Analysis of previously published work ((Fu *et al.*, 2017); Fig 4.1B) led me - at the start of my thesis - to tentatively suggest that in an 11-somite embryo, the A-fold is composed of *FGF10*-expressing

progenitors, while the V-face is composed of nascent anterior tuberal progenitors that have downregulated *Fgf10*.

It proved difficult to reconstruct these structures in 3-D from sequential sagittal sections, due to variability in sample orientation and slicing angle. As a result, I turned to wholemount analyses of isolated neuroepithelia to get a clearer picture. To remove the neural tube from its surrounding tissues I applied dispase (a protease treatment that dissociates tissue layers), then dissected away mesodermal, endodermal and ectodermal tissues, leaving only the neuroepithelium. This was then incubated with DAPI, placed in a well (dorsal down) and visualised using fluorescence microscopy to enable 3-D reconstruction of the tissue through optical sectioning (see Section 2.2-3).

Again, due to the dense packing of cells in the neuroepithelium, their DAPI-labelled cell nuclei were a sufficient proxy for overall tissue shape. 3-D imaging revealed the extent and position of the A-fold and V-face. In a stage 10.3 embryo the A-fold was U-shaped with its posterior apex at the ventral midline, and in line with the posterior extent of the optic vesicles, and the V-face extended towards the anterior neuropore (Fig 4.1D, magenta arrowhead, green and blue square brackets respectively). The 3-D reconstruction also showed the ventral extent of the A-fold and V-face (Fig 4.1D)..

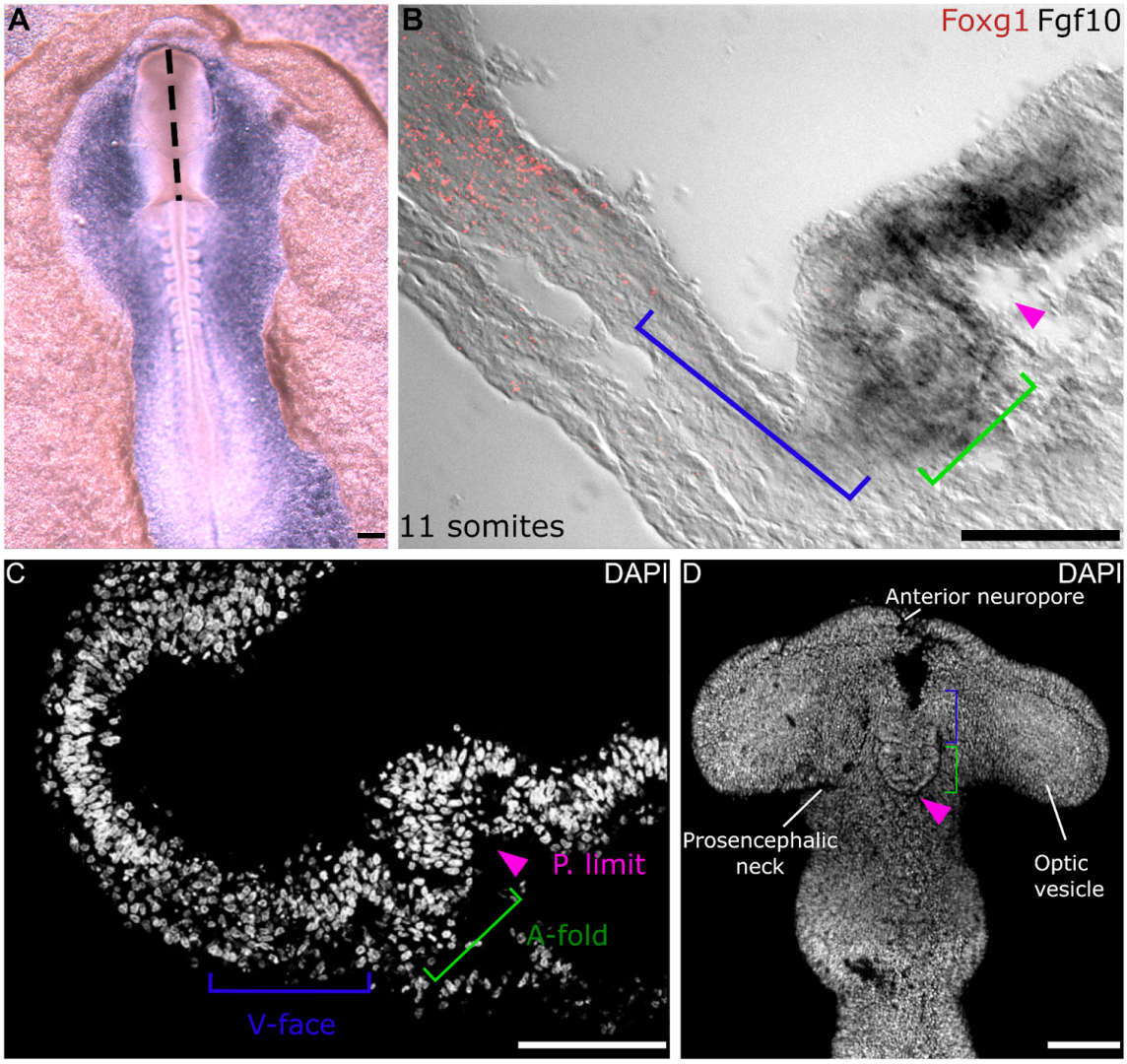

Figure 4.1: The developing hypothalamus at HH10 has a characteristic 3-D morphology. (A) Dorsal view of a stage 10.1 chick embryo, demonstrating the sectioning plane for (B-C) (black dotted line) (4x). (B) Mid-sagittal views labelled via *in situ* hybridisation for *Foxg1*-expressing telencephalic cells and *FGF10*-expressing hypothalamic progenitors (40x), reproduced from (Fu *et al.*, 2017). (C) Mid-sagittal views of the neuroepithelium labelled with DAPI (20x). (D) Ventral wholemount view of a 10.3 embryo (10x). Magenta arrowheads indicate the posterior limit of the A-fold, green square brackets indicate the A-fold, and blue square brackets delineate the ventral face (V-face) Scale bars: (A) 200μm; (B) 50μm; (C-D) 100μm.

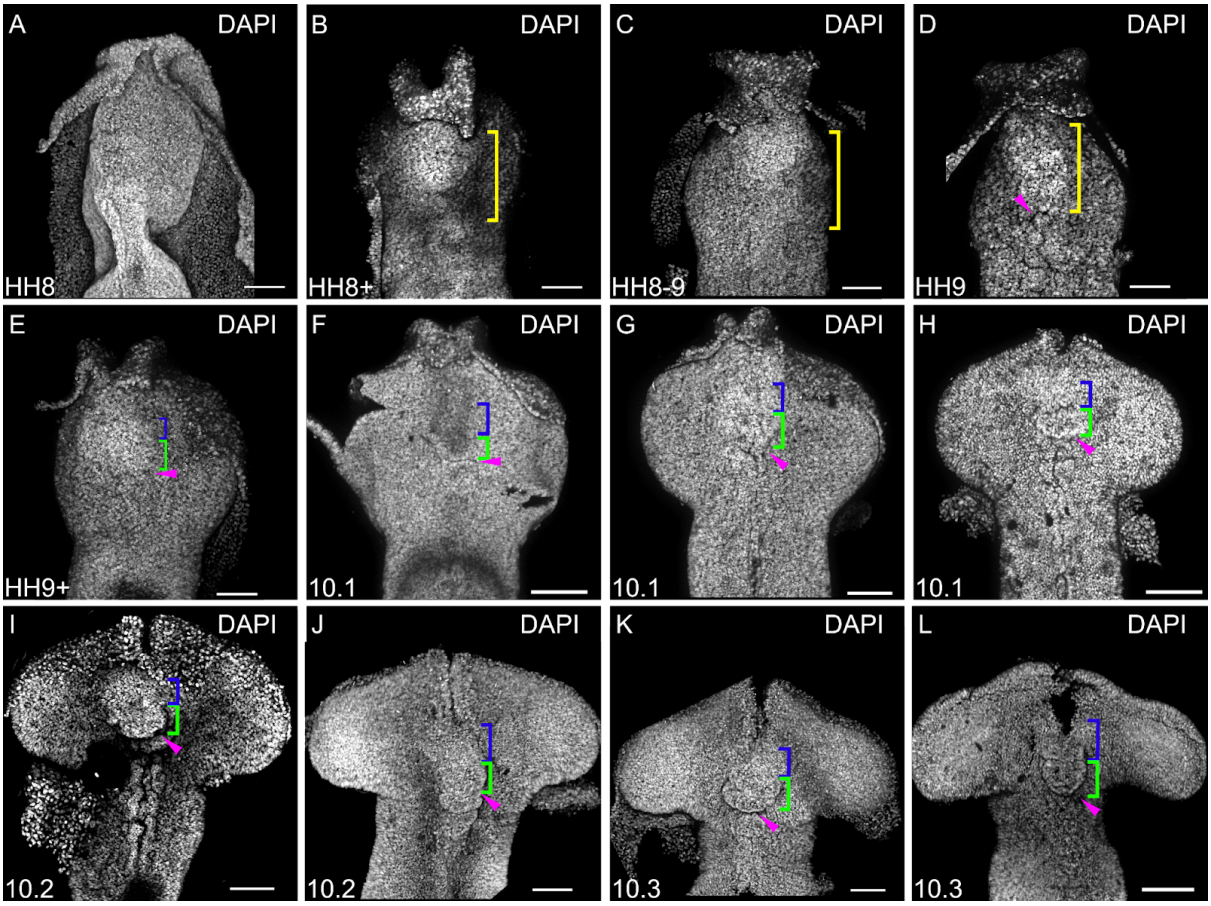

Figure 4.2: 3-D imaging of wholemount isolated neuroepithelia reveals complex tissue morphology, including a ventral indentation and tissue fold(s). Images arranged in increasing developmental stages (from A-L), determined through somite number and overall morphology of neuroepithelium. All images show ventral views. During HH8, a ventral indentation forms (A-C, yellow square brackets) At early HH9, the ventral midline begins to fold (D, magenta arrow), which was the earliest detectable sign of the A-fold. From HH9-10, an A-fold in the ventral midline was detectable, initially appearing as a horizontal fold (E-F, green square brackets then becoming U-shaped (G-H green square brackets. Magenta arrows point to posterior apex of A-fold. The tissue anterior to the A-fold was the V-face (E-L, blue square brackets). During HH10 sub-stages, multiple folds appear, transiently (I-L). Scale bars: 100μm.

Next, I asked when the A-fold/V-face first become apparent, by examining wholemount images of dissected embryos between HH8 and HH12. The prosencephalon was morphologically distinct throughout these stages, because it broadens from a pinch-point at the prosencephalic neck (Fig 4.2A-L).

At HH8, the ventral surface of the prosencephalon appeared to be flat (Fig 4.2A). By HH8+ (6 somites) to HH9, however, a wide, shallow indentation was apparent around the anterior

ventral midline (Fig 4.2B-D, yellow square brackets, n=3). From HH9 to HH10, this indentation became progressively more focal, and represented a smaller proportion of the ventral tissue (Fig 4.2F-L). Beginning at HH9, a fold appeared in ventral midline tissue at the posterior part of the indentation (n=3/ 6; Fig 4.2D-L, magenta arrowheads). By HH10, all embryos exhibited this fold, agreeing with the cross-sectional data (n=18). Transiently, over stage 10.1 and 10.2, multiple posterior folds were detected, but at stage 10.3 these were no longer detected, and only the single prominent U-shaped A-fold was observed (Fig 4.1K-L, magenta arrowhead).

While the size and extent of the A-fold appeared dynamic throughout HH10-11 (Fig 4.2E-L, green square brackets), this was most likely an artefact of tissue orientation. The anterior limit of the V-face tissue was harder to define, as there were fewer morphological landmarks. However, side-views suggested that, at its anterior limit, the V-face began to curve and turn dorsally (Fig 4.1B-C), and I tentatively labelled the wholemount views accordingly (Fig 4.2E-L, blue square brackets).

4.2.2 3-D morphometric analyses of hypothalamic morphology at the tissue and cellular level

While the wholemount analyses showed that the A-fold and V-face are characteristic features of the ventral midline, their exact position and shape was difficult to pinpoint, and the anterior limit of the V-face was not obvious. A better understanding of the position and shape of these structures is of potential importance, as these landmarks could represent important boundaries between distinct progenitor populations. I therefore next sought to define the anterior limit of the V-face, and pinpoint the positions of the A-fold and V-face as discrete morphological landmarks by examining their morphometric characteristics relative to surrounding forebrain tissue.

To do this, I examined the tissue-scale mean curvature of the ventral prosencephalon (Fig 4.3), reconstructing the epithelial surface from the DAPI images of densely packed nuclei. I then investigated first the indication from the 3-D imaging that the indentation arises after HH8, and transitions from a broad indentation into a midline structure which exhibits folds; and second, whether any tissue-wide morphological characteristics could be used to help demarcate an anterior boundary for the V-face.

To examine curvature, I extracted surface meshes for neuroepithelia at stages HH9, 10.1, 10.3, and HH13 and computed the mean curvature of each mesh, rescaling these values from 1 to -1 (corresponding to the points of highest and lowest curvature in each mesh, respectively). I then isolated the highest regions of curvature in the embryo, and manually filtered out the surfaces with curvatures below a threshold of 60% of the maximum curvature value (the 60% threshold was tuned empirically, scaled to each embryo such that the flat and negatively curved regions were omitted), leaving the highest points of curvature.

Reconstruction of the surface at HH9 revealed a small oblong region in the anterior-most ventral neuroepithelium that appeared to have relatively higher curvature than the adjacent neuroepithelium, especially at its posterior end (Fig 4.3A', white dotted outline). Nonetheless, the difference was subtle, confirming the conclusion from optical sections that the curved indentation was just forming (Fig 4.3A''). Reconstruction at stage 10.1 showed areas along the anterior ventral midline that transitioned from low to high curvature. The largest was anterior-most, i.e. marking the A-fold (Fig 4.3B', green and magenta arrowheads). Thresholding confirmed this large circular region to be of high curvature relative to the rest of the embryo (Fig 4.3B''). Comparison with HH9 suggested that the onset of high curvature in the anterior ventral midline was concomitant with a decrease in curvature of the tissues lateral and anterior to this region (Fig 4.3B'', blue arrowhead). These analyses support the conclusion from optical sectioning that by 10.1, multiple folds appear in the anterior ventral midline, with the most prominent being the A-fold.

At stage 10.3, the optic vesicles in the forebrain appeared pronounced and the developing hindbrain began to bulge, relative to earlier stages (Fig 4.3C). Despite these profound tissue-scale changes in morphology, a high point of curvature was still apparent along the ventral midline, with a high point at the posterior edge of the A-fold (Fig 4.3C', magenta arrowhead). When thresholded, the A-fold was apparent as a U-shape (Fig 4.3C'-C'', green arrowhead), with the V-face detected as a flattened area of tissue anteriorly (Fig 4.3C'-C'', blue arrowhead, note this embryo is the same shown in Fig 4.1D, 2L). Despite a tear in the tissue, the anterior limit of the V-face was apparent through a transition from medium to low curvature (Fig 4.3C' white dotted line).

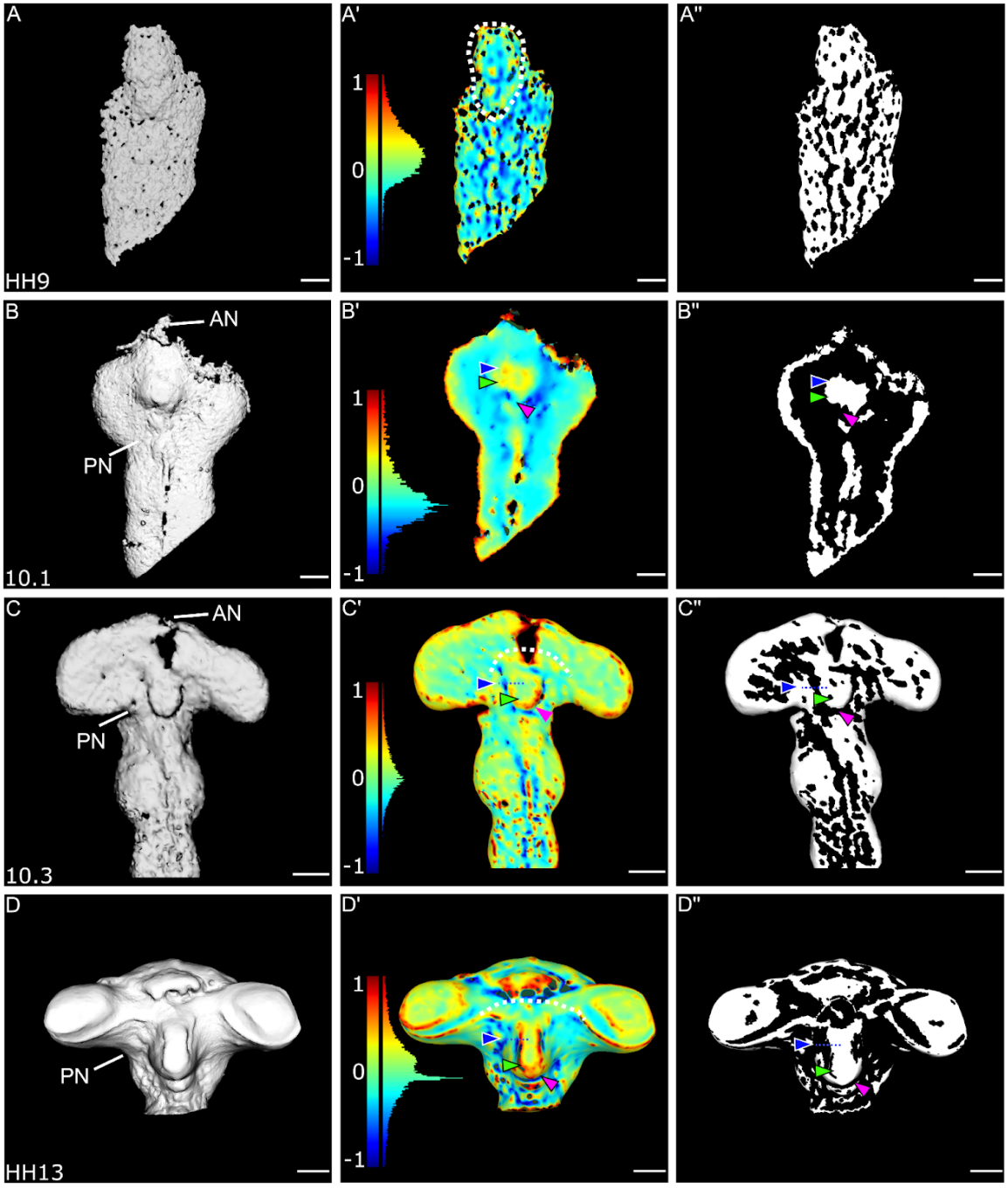

Figure 4.3: 3D morphometrics show that from HH9-HH13, the hypothalamus becomes more highly curved. Surface reconstruction 3D models of HH9 (A), stage 10.1 (B), stage 10.3 (C), and HH13 (D) embryos, obtained from thresholding the DAPI signal. 3D mean curvatures are coloured from cool to warm (lowest to highest curvature); histogram height corresponds to the number of mesh vertices with that curvature (A'-D'). Points of highest relative curvature are shown in white (A''-D''), with regions whose curvature is less than 60% of the maximum filtered out. The A-fold (green arrowhead), its posterior apex (magenta arrowhead), the V-face (blue arrowhead), and its anterior limit (white dotted line) are indicated (n=1 per stage). Scale bars: 100μm.

By HH13, the oldest stage examined, there were three regions with substantially higher curvature than adjacent regions. Two of these were within the optic vesicle; the third was the ventral midline. Here, the mean tissue curvatures that had been detected at earlier stages were greatly increased (Fig 4.3D'). Similar to the profile of stage 10.1 and 10.3, the A-fold was easily detectable as a sudden transition from low to high curvature (Fig 4.3D'-D'', magenta and green arrowheads) and the V-face was a relatively flatter region anterior (Fig 4.3D'-D'' blue arrowhead). Similar to the stage 10.3 embryo, the anterior limit of the V-face was defined by a transition from high to low curvature anteriorly (Fig 4.3D', white dotted line). Strikingly, the A-fold showed a similar level of curvature to the optic vesicles, and both remained when thresholded (Fig 4.3D'').

A key finding from these curvature analyses was that the relative position of the A-fold (as marked by the transition from low to high curvature in the anterior ventral midline) moved posteriorly, relative to the prosencephalic neck over HH9-HH13. At the same time, the V-face lengthens, judged through the position of the A-fold/V-face boundary respective to the anterior neuropore (Fig 4.3B-D AN), or most anterior point pictured. At stage 10.1 the V-face was in-line with anterior regions of the optic vesicle; and progressively between 10.1-3 the V-face became closer to, before becoming in-line with the prosencephalic neck, the region where the most posterior regions of the optic vesicle outpocket laterally. Re-examination of the wholemount neuroepithelia confirmed this (Fig 4.2F-L).

In summary, the curvature analyses support and extend the observations made in Section 4.2.1 that the anterior ventral midline undergoes discrete changes in morphology around HH10, characterised by a pronounced U-shaped A-fold that abuts the flatter V-face at its anterior edge. The A-fold moves backwards relative to the prosencephalic neck, and concomitantly, the V-face lengthens. As discussed in Chapter 1, the late embryonic / adult hypothalamus protrudes from the ventral surface of the forebrain, anterior to the cephalic flexure and ventral to the forming zona limitans intrathalamica. The rapid, stark changes in developing ventral morphology reported here could thus be the first sign of this more protruded morphology.

I next examined the geometry of cells within the ventral prosencephalon, to identify any morphometric patterns. I focused on cell shape, an important indicator of cellular function in epithelial morphogenesis (Gillard and Röper, 2020). This analysis was limited to a single embryo at stage 10.2. To outline cell shape, I labelled the lateral cell membrane using an antibody for the membrane-bound protein β-catenin (Fig 4.4A). At low magnification

(10-20x), individual cells could not be discerned easily, due to the dense cell packing within the tissue (Fig 4.4A, A'). To address this, I used high-magnification confocal microscopy (63x), tiling multiple fields of view. For tractability, I only analysed the A-fold/V-face cells, which were the most ventral of optical sections (and cover the area delineated by the dotted outline in Fig 4.4A''). This showed that high β-catenin labelled a trapezoid-shaped area, widest most anteriorly (Fig 4.4A''). Comparison of the tiled and DAPI views suggested the narrow area was the A-fold (demarcated with green dotted outline) and the wider area was the V-face (blue dotted outline). I then performed 3-D segmentation using the DNN U-Net (Ronneberger *et al.*, 2015), as part of PlantSeg, a morphometric analysis pipeline for measuring properties of membrane-labelled cells (Wolny *et al.*, 2020). This yielded predictions about whether each pixel belonged to a cell membrane (Section 2.3.6). I then conducted morphometric analysis on these regions (Fig 4.4A''), computing cell sphericity (Fig 4.4B), surface area (Fig 4.4C), and volume (Fig 4.4D); see Section 2.3.7 for details).

At stage 10.2, there was substantial heterogeneity in each of the metrics between the A-fold and V-face. Cells in the anterior part of the A-fold were more spherical than those in its posterior part; while cells in the posterior-central part of the V-face were more spherical than cells towards its peripheral regions. This might be important: epithelial cells round up as they enter mitosis (Taubenberger et al., 2020), hence the spherical cells could be more proliferative than other adjacent cells. Quantitative analyses showed that cells of high sphericity were also of highest volume, but of lowest surface area (Figs 4.4B-D).

In summary, I identified a novel morphological structure - an anterior ventral midline indentation - which appears to give rise to distinct morphological regions: the U-shaped A-fold and the V-face. These arise between HH9 and HH10.

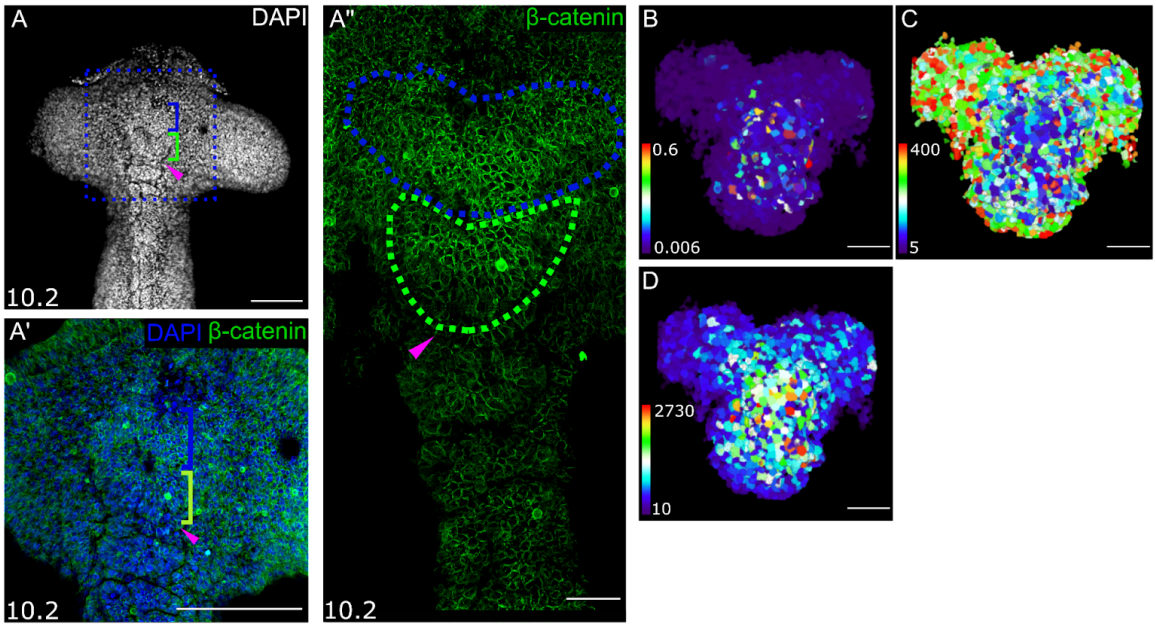

Figure 4.4: Cell shapes differ within the A-fold and V-face of the stage 10.2 embryo. (A-A') Ventral view of an isolated stage 10.2 neuroepithelium at 10x (A) and 20x (A'). Blue dotted square in A shows the view in A'. At these magnifications and resolutions, it was challenging to perform 3D cell segmentation due to overlap in cell boundaries delineated by an immunolabel for the cell membrane protein β-catenin. Magenta arrowhead: posterior apex of A-fold, Green square bracket: A-fold; blue square bracket: V-face. (A''): 63x high magnification ventral view of the same embryo as in A-A'. The higher power and increased resolution allowed for more robust 3D segmentation of cell shapes. Blue and green dotted lines delineate the V-face and A-fold respectively, and together they form the quantified area in B-D. (B-D): 3D cell segmentation colourised from cool (low values) to warm (high values) colours according to: sphericity (B); surface area (C); and volume (D). Scale bars: (A-A') 100μm; (A'', B-E) 25μm.

4.2.3 A-fold and V-face cells are proliferative at HH10-12

My morphometric analyses showed spherical cells (i.e potentially proliferative as mitotic cells adopt spherical morphologies (Cadart *et al.*, 2014)) in the anterior part of the A-fold, and in the posterior-central part of the V-face. I therefore examined proliferation in these regions over HH10-13. I sought to determine if V-face and/or A-fold cells are proliferative, whether levels of proliferation are substantially different in any particular part of the A-fold or V-face, and more generally if proliferation patterns correlate with particular aspects of hypothalamic morphology.

I characterised proliferation in dissected 3-D neuroepithelia. I analysed cells in G2-M phase using an antibody against phospho-histone H3 (pH3) (Fig 4.5A-B, A'-B'), which is produced by cells undergoing the G2 to M phase cell cycle transition (Hans and Dimitrov, 2001), and cells in S-phase, using EdU (Fig 4.5C-D, C'-D'), a thymidine analogue incorporated during DNA synthesis (Yu *et al.*, 2009)

I did not discern any clear patterns of proliferation. Fig 4.5 shows representative images from n=6 embryos. I identified proliferating cells in both the A-fold and V-face at all stages analysed (Fig 4.5A-D). Relatively few M-phase cells were detected, in comparison to S-phase cells. In general, lower numbers of dividing cells were detected in the A-fold/V-face in comparison to other brain areas: high levels of proliferation were detected in the telencephalon and optic vesicles. Potentially, there was a subtle pattern to cells in M-phase, which were detected most abundantly at the A-fold/V-face border, and at the V-face periphery. However, there was no discernable pattern to S-phase cells

The combination of sparse pH3 labelling (Fig 4.5A-A', 5B-B') and high numbers of EdU+ cells (Fig 4.5C-C', 5D-D'), as well as the high sensitivity of the EdU methodology, meant the study was difficult to interpret and underpowered, and I would therefore require larger amounts of data to draw firm conclusions about patterns of proliferation within and relative to the V-face cells. Nevertheless, my results indicate that the folds (including the A-fold) do not appear to be due to hyperproliferation, as in all cases there were fewer pH3/EdU positive cells in the A-fold than in the surrounding developing brain.

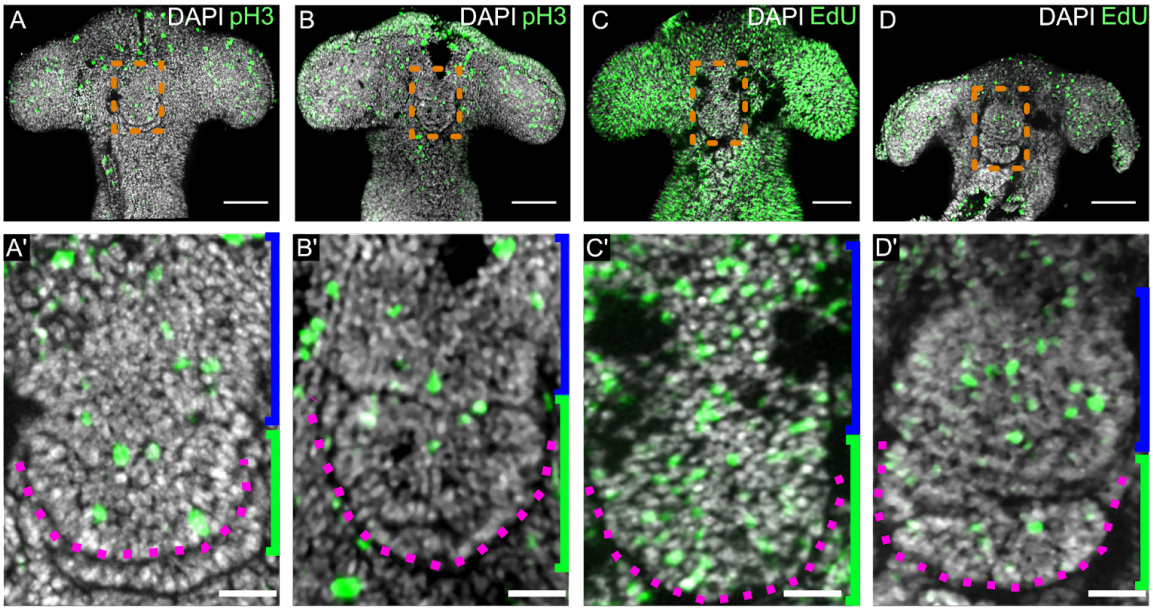

Figure 4.5: V-face cells are proliferative at HH10-13. (A-D): Ventral views of isolated neuroepithelia at HH10 (A), stage 10.3 (B), HH11 (C), and HH13 (D), labelled for markers of the cell cycle. (A'-D') show zoomed views of blue boxed regions, the purple dotted line represents the A-fold, the green square bracket the anteroposterior extent of the A-fold and the yellow square bracket the V-face. (A-B, A'-B') Phospho-histone H3 (pH3) labelling shows cells undergoing a G2/M phase transition of the cell cycle. At HH10-11 there are proliferating cells in the A-fold (A'-B', green square brackets; magenta dotted lines demarcate posterior limits of the U-shaped A-fold. At HH10-11, pH3 positive cells are also detected in the V-face (A'-B', blue square brackets). (C-D, C'-D') EdU labelling marking cells in S-phase of the cell cycle. At HH11, there was proliferation in the V-face cells (C'), yet at a lower frequency than the surrounding tissue (C). At HH13, this difference was reduced (D'). Scale bars (A-D): 100μm, (A'-D'): 50μm.

4.3 Summary

The overall hypothesis that I have investigated in this, and Chapter 5, is that morphogen-like signalling ligands might play an important role in the development of the 3-D tissue morphology of the hypothalamus. To begin to address this I first had to examine when I could detect the first obvious signs of 3-D morphology in the ventral prosencephalon. To do so, I developed a novel approach, isolating neuroepithelia and analysing wholemount ventral views.

I detected the first signs of development of 3D morphology at HH8-HH9, when a large ventral indentation becomes obvious. This occurs at the same time that the prosencephalic neck becomes obvious, and the optic vesicles start to form. Over HH9 and stage 10.3, the ventral indentation rapidly forms a series of ventral folds, as detected visually and through curvature analyses. I defined the anterior-most fold as the A-fold. The A-fold has a characteristic U-shape by stage 10.3. Immediately ahead of the A-fold is a relatively flatter tissue I defined as the V-face. This elongates over HH10-12, and at the same time, the A-fold moves relatively backwards within the prosencephalon. My 3-D cell morphometric analysis showed that cells in the central anterior part of the A-fold and central posterior part of the V-face are more spherical than other regions of these tissues. They may be more frequently undergoing mitosis, but my proliferation assays did not provide useful data on this.

With a clearer picture of the morphological changes that occur over HH8-12, I next aimed to answer whether this morphology correlated with, or could be predicted by, expression of key signalling factors that are known to operate in the developing hypothalamus.

Chapter 5

3-D imaging of signalling ligand expression in the developing hypothalamus

5.1 Introduction

I next investigated whether the expression profile of known signalling ligands might prefigure the morphology of the developing hypothalamus, ie. the U-shaped A-fold and the V-face.

The Fu et al (2017) study, described in Chapter 1, suggested complex and dynamic expression of *SHH* and *FGF10* in the developing hypothalamus. This study concluded that they are co-expressed at HH9-10, then, between HH10-12, they largely resolve into: *SHH*-expressing anterior tuberal progenitors, which migrate/grow anteriorly; *FGF10*-expressing posterior tuberal progenitors, which do not expand extensively; and SHH-expressing mammillary progenitors, which expand. At the same time, pharmacological studies, using cyclopamine, indicated an ongoing role for SHH in directing the proliferation and differentiation of anterior tuberal progenitors (Fu et al., 2017) and their progression to tuberal neuronal precursors. The relative expression patterns of *FGF10* and *SHH*, however, were limited to analyses of sagittal sections and were mostly performed using chromogenic *in situ* hybridisation rather than sensitive double-labelling (Fu *et al.*, 2017).

The fact that (i) *SHH* and *FGF10* had not been previously imaged in 3-D, and (ii) they had complex expression profiles over HH10-12 (the stages where the A-fold/V-face are developing in earnest) led me to first focus on analysing the expression of *SHH* and *FGF10* in ventral wholemount views of isolated neuroepithelia.

5.2 Results

5.2.1 *SHH* and *FGF10* are reciprocally expressed as the hypothalamic A-fold forms

I analysed the expression profiles of *SHH* and *FGF10* in 3-D using double-labelled hybridisation chain reaction (HCR) *in situ* hybridisation, a sensitive technique that allowed me to accurately compare their expression profiles. I performed these analyses over HH9-HH13 in collaboration with a postdoctoral researcher in the Placzek group, Dr K. Chinnaiya, who optimised the wholemount HCR technique while I optimised the 3-D imaging.

My ventral wholemount views provided a detailed picture of the extent and shape of gene expression domains. Moreover, since the morphological features I had described in Chapter 4 (forming folds, A-fold, V-face) were still apparent after HCR and DAPI labelling, I was able to assess the patterns of expression of *FGF10* and *SHH* relative to these features. My results indicated a consistent pattern of expression of *FGF10*, relative to expression of *SHH*, which was expressed in the U-shaped A-fold. My results also (Fig 5.1A'-C'') showed that the conclusions of Fu *et al*. (2017) - that *FGF10* and *SHH* are initially co-expressed - were not correct.

At HH9+ and 10.1, *SHH* and *FGF10* did not show the same anterior limit, but instead, showed almost reciprocal expression along the A-P axis, overlapping in the developing (HH9+) or clearly-formed (10.1) A-fold (Fig 5.1A'-A''', B'-B'''). *FGF10* expression extended from close to the anterior neuropore into the A-fold (Fig 5.1A', B'). By contrast, *SHH* was detected in the ventral midline of the posterior neuroaxis, through the forming folds (at HH9+) and the clearly-formed A-fold (at 10.1), terminating just ahead of this in V-face (Fig 5.1A''-B''). The expression levels of *SHH* appeared to vary. Since the views are maximum intensity projections, the seemingly strong *SHH* expression in the A-fold (and the other transient folds) is most likely an artefact of imaging that reflects the depth of the A-fold. Overlaid, *FGF10* and *SHH* appear therefore to overlap in the posterior V-face and the A-fold (Fig 5.1A'''-B''').The position of *SHH* and *FGF10*, relative to the A-fold and V-face were independently confirmed by Dr Sarah Burbridge (a postdoc in the lab), through examination of mid-sagittal sections.

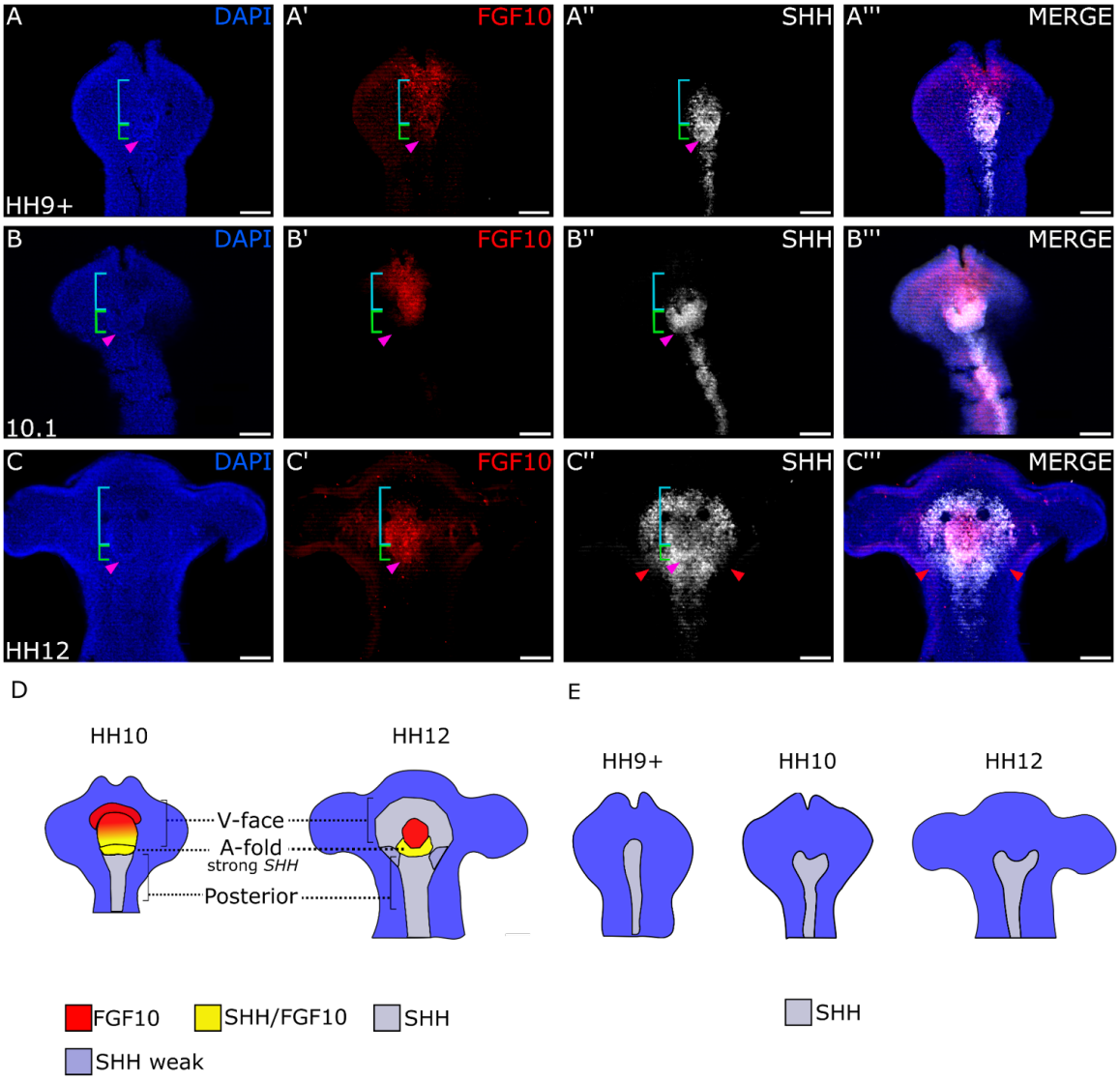

Figure 5.1 A-fold and V-face cells express genes encoding key hypothalamic signalling ligands SHH and FGF10. Magenta arrow: posterior apex of A-fold. Green square bracket: A-fold. Blue square bracket: V-face. All images show ventral views of isolated neuroepithelia. (n=1 per stage). (A) At HH9+ (late HH9), *SHH* and *FGF10* expression domains are not coincident (A-A''). (B) At stage 10.1 *FGF10* extends more laterally, and *SHH* more anteriorly and laterally than at HH9+ (B'-B''). (C) Ventral view of an isolated neuroepithelium from a HH12 embryo processed as in (A-B). *FGF10* is expressed highly in the centre of the V-face, and weakly laterally (C'). *SHH* is expressed highly in the anterior V-face, and the A-fold, and is downregulated in the centre of the V-face (C''). (D) Schematic summarising the observed transition in expression domains over HH10-12: a *SHH*/*FGF10* co-expressing domain remains, but *SHH* and *FGF10* otherwise resolve into discrete populations along the anteroposterior axis. (E) Schematic of the observed expression transition of *SHH* from a rod-shaped to a Y-shaped pattern. Scale bars: 100μm.

In situ analyses for *SHH* and *FGF10* were performed by Dr K. Chinnaiya, and images were acquired in collaboration with Dr K. Chinnaiya.

From HH10 to HH12 the profile of *FGF10* changed, resulting in an oval region of expression at HH12. However, throughout HH9-HH12, the relative positions between the *FGF10* and *SHH* expression domains remained the same: *FGF10* was nestled within (i.e. partially surrounded by), and overlapped with, the U-shaped *SHH* expression domain. Strikingly, the A-fold appeared to consistently be coincident with *SHH* expression (Fig 5.1C'), suggesting that SHH (at least) may prefigure the development of the hypothalamic morphology described in Chapter 4. My imaging also showed the progression/development of *SHH* expression over the period HH9-HH12. Previous chromogenic studies have shown that SHH expands from a rod, to an oval, then to a torus (Fig 1.2). My imaging demonstrated how these expression profiles link to morphological features. The SHH-negative torus 'hole/interior' coincided with the posterior V-face, where *FGF10* was detected. The outer torus of SHH was not uniform. A strong arc of expression was detected towards the anterior edge of the V-face, but expression of *SHH* was much weaker in the part of the torus lateral to the A-fold, at the level of the prosencephalic neck (Fig 5.1C"-C'", red arrowheads). The A-fold itself, and more posterior regions, expressed *SHH* strongly.

Taken together, these results showed that whereas *SHH* is initially expressed uniformly in ventral midline cells, it comes to be expressed in a non-uniform manner in the developing hypothalamus (high-low-high expression from anterior to posterior and low expression in the radially-expanded domain, lateral to the A-fold (Fig 5.1D). In addition, these results showed that while *FGF10* was initially anterior to *SHH,* by HH12 *FGF10* and *SHH* had swapped relative positions (Fig 5.1D).

These findings support my hypothesis that the expression of signalling ligands might prefigure morphology. In particular, at HH9+ I detected reciprocal patterns of expression of *FGF10* and *SHH* whose overlap predicts the A-fold and V-face. Further, these studies show that throughout the period HH10.3- HH12, the *SHH/FGF10*-expressing overlapping domain marks the A-fold.

5.2.2 *BMP2* is transiently detected at the V-face/A-fold interface

I next examined the relative expression patterns of *SHH* and *BMP2*, to ask whether their profiles might predict any aspect of hypothalamic morphology. BMP2 has previously been shown to downregulate *SHH* in the developing hypothalamus (Manning *et al.*, 2006), and has recently been identified as important to hypothalamus development from a scRNA-seq study (Kim *et al.*, 2022), but to date its expression has not been studied in detail in the developing hypothalamus.

I began by analysing embryos from HH8 until late-stage HH11 (HH11+). Unlike in Section 5.2.1, all subsequent analyses were performed by me alone (see front matter: acknowledgement of collaborative work within the thesis for details). In a first round of HCR *in situ* studies, triple-label analyses were performed to simultaneously detect *GLI1/BMP2/PTCH1* (discussed in this chapter) and in a second round (same embryos), triple-label analyses were performed to detect *SHH/FST/GLI3* (*SHH* discussed here; others discussed in Chapter 6).

At HH8-9, *BMP2* showed an expression profile that was highly similar to *SHH* in developing hypothalamus cells (Fig 5.2A'-B''''). However, by 10.1, the expression profile of *BMP2* had changed drastically: *SHH*-expressing cells had lost *BMP2* expression, which was now confined to a heart-shaped arc around them (Fig 5.2C'-C''''). Very transiently, BMP2 expression was highest in the anterior-most part of the arc (Fig 5.2D'', Fig 3C'').

From 10.1- HH11, however, the expression of *BMP2* became more tightly focused, fading in the anterior part of the heart-shaped arc, and becoming restricted to two lateral bands of expression running along the tissue lateral to the midline. (Fig 5.2C''-F''). The lateral bands of expression of *BMP2* were situated directly adjacent to the *SHH*-strong A-fold, possibly delineating their mediolateral border (Fig 5.2C'''-F''', orange dotted line).

In terms of morphological features, then, initial expression of *BMP2* predicts the folds (including the A-fold), The transient high level BMP2 expression in the anterior part of the heart-shaped arc correlates with the V-face/A-fold boundary. The sustained lateral expression of *BMP2* correlates with the medio-lateral border of the A-fold.

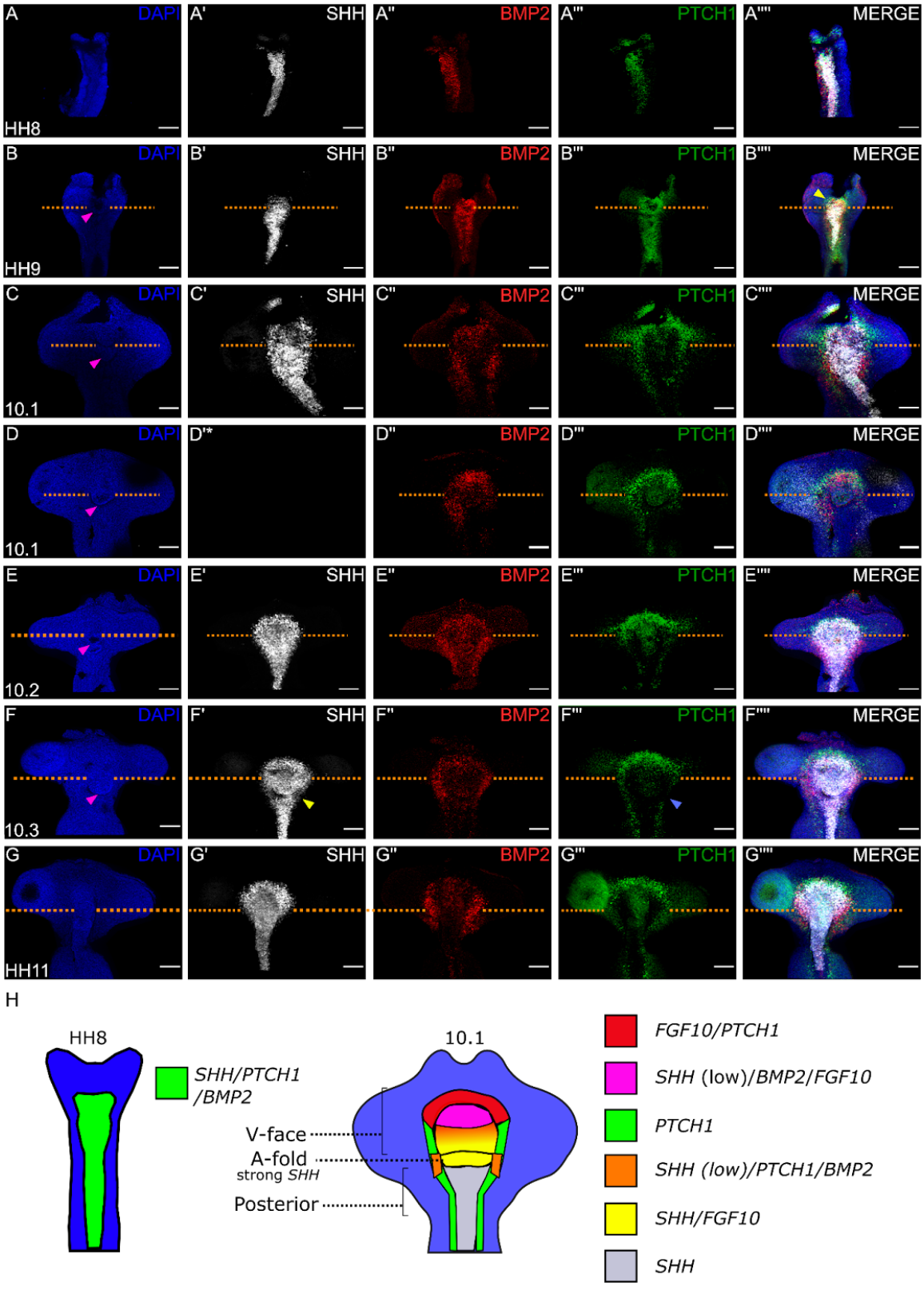

Figure 5.2: Early regionalisation of *SHH*, *PTCH1*, and *BMP2* in the HH8-11 developing hypothalamus. Wholemount ventral views of HH8-11 neuroepithelia from embryos processed by HCR in situ hybridisation for *SHH* (A'-F'), *BMP2* (A''-F''), and *PTCH1* (A'''-F''').

with morphology shown by the DAPI signal (A-F). Magenta arrowheads indicate posterior apex of the A-fold, orange dotted lines indicate the A-fold/V-face boundary at HH9-11. At HH8, *SHH* extends anteriorly, and marks the developing hypothalamus (A'). There was some expression of *PTCH1* in the gut endoderm at the most anterior tip or the embryo, but otherwise *BMP2* and *PTCH1* are expressed in the *SHH* positive cells (A''-A'''). At HH9, in the centre of the V-face, *PTCH1* has been downregulated, whereas *SHH* and *BMP2* remain similar to the HH8 profile (B'-B'''). For the 10.1-10.3 sub-stages, there was a clear regionalisation between *SHH*, *PTCH1*, and *BMP2* positive cells. *SHH was* expressed in the A-fold and the V-face (C'), and *BMP2* surrounds the *SHH* expressing cells (C''), sharing a similar profile to *PTCH1*, which extends further anteriorly (C'''). Throughout my sub-stages 10.1-3, a progressive widening mediolaterally of the *SHH* domain occurs (C'-E'), and simultaneously *BMP2* positive cells showed a progressive weakening anteriorly with a strengthened expression along the tissue lateral to the posterior midline in the tissue which downregulates *SHH* (D''-F''). *PTCH1* expression mirrored this, as it was reduced along the posterior midline and laterally, becoming a strong mediolateral strip of cells anteriorly by 10.3 (C'''-F'''), these shape profiles then persisted in HH11 (G'-G''''). (H) Summary panel of patterning events between HH8-10.1. N.B. Merge panels in A''''-G'''' were aligned manually as the samples were imaged multiple times (due to reprobing - note that * represents an embryo lost in reprobing) and imaging orientations differed slightly. Scale bars: 100μm.

5.2.3 *PTCH1* expression suggests regionally-distinct levels of SHH signalling in the developing hypothalamus

I have shown so far that the expression profiles of *SHH, FGF10* and *BMP2* change concurrently with the development of the A-fold/V-face morphology. Yet, my hypothesis that these factors influence the development of 3-D morphology implies that these ligands signal actively over HH8-11. Ideally, I would have sought evidence for active signalling of each ligand, but as time was limiting, I focused on analysing read-outs of the SHH signalling pathway.

To investigate SHH signalling, I first investigated the expression of *PTCH1.* PTCH1 is the canonical SHH receptor, and its relationship with SHH is relatively well characterised in early neural development. In the developing posterior neuraxis, *SHH* and *PTCH1* are initially co-expressed, and following this *PTCH1* becomes downregulated in *SHH*-expressing cells in the midline floor plate (Marigo and Tabin, 1996). This is thought to be due to specific motifs

of SHH/PTCH1 signalling: SHH signalling induces *PTCH1*, PTCH1 then represses the expression of *PTCH1*. Thus, where SHH signalling is highest, *PTCH1* is induced highly, and as a result *PTCH1* expression is eventually downregulated. Additionally, PTCH1 inhibits *SHH* through ligand dependent antagonism (Dessaud *et al.*, 2008; Groves *et al.*, 2020), resulting in a complex and non-linear interaction.

Investigating the expression *PTCH1* would therefore simultaneously provide me with an indication of whether SHH signalling is active, whether *PTCH1* is regulated at equivalent levels in all parts of the developing hypothalamus, and also whether there is any indication of spatial regulation between *PTCH1* and *SHH.* To this end, I visualised *PTCH1* expression alongside *SHH* and *BMP2* (Fig 5.2A’’’’-G’’’’).

At HH8, before the development of the A-fold/V-face, *SHH* and *PTCH1* were co-expressed in the ventral midline of the prosencephalon, suggesting high levels of SHH signalling in the nascent hypothalamus. By HH9, however, *SHH* and *PTCH1* started to become regionalised, as the A-fold/V-face boundary began to become detectable (Fig 5.2B-B’’’, orange dotted line). Each was still expressed in the A-fold, but *PTCH1* was not expressed in the weakly *SHH*-positive V-face cells, and instead, was detected in an arc around these (Fig 5.2B’, B’’’), suggesting the beginning of a regionalisation between *SHH/PTCH1* expression.

Over 10.1-10.3 *SHH* and *PTCH1* almost completely resolved into discrete domains of expression, reflecting an expression profile seen elsewhere in the neuraxis (Marigo and Tabin, 1996). *PTCH1* was barely detectable in *SHH*-expressing cells, but instead was detected around these (Fig 5.2 C’’-F’’). Merged views however showed an overlap, i.e. outermost *SHH*-expressing cells appeared to co-express *PTCH1*. Strikingly, however, expression of *PTCH1* was not uniform, and instead, highest expression levels were detected in the hemi-arc around the *SHH*-expressing V-face cells (Fig 5.2C’’’-F’’’). The regionalisation between *SHH* and *PTCH1* expression persisted into HH11 (Fig 5.2G’’’’). Comparison with *BMP2* expression suggested that the regions of weaker *PTCH1* expression were coincident with the lateral bands of *BMP2* described above (Fig 5.2E’’’’-G’’’’).

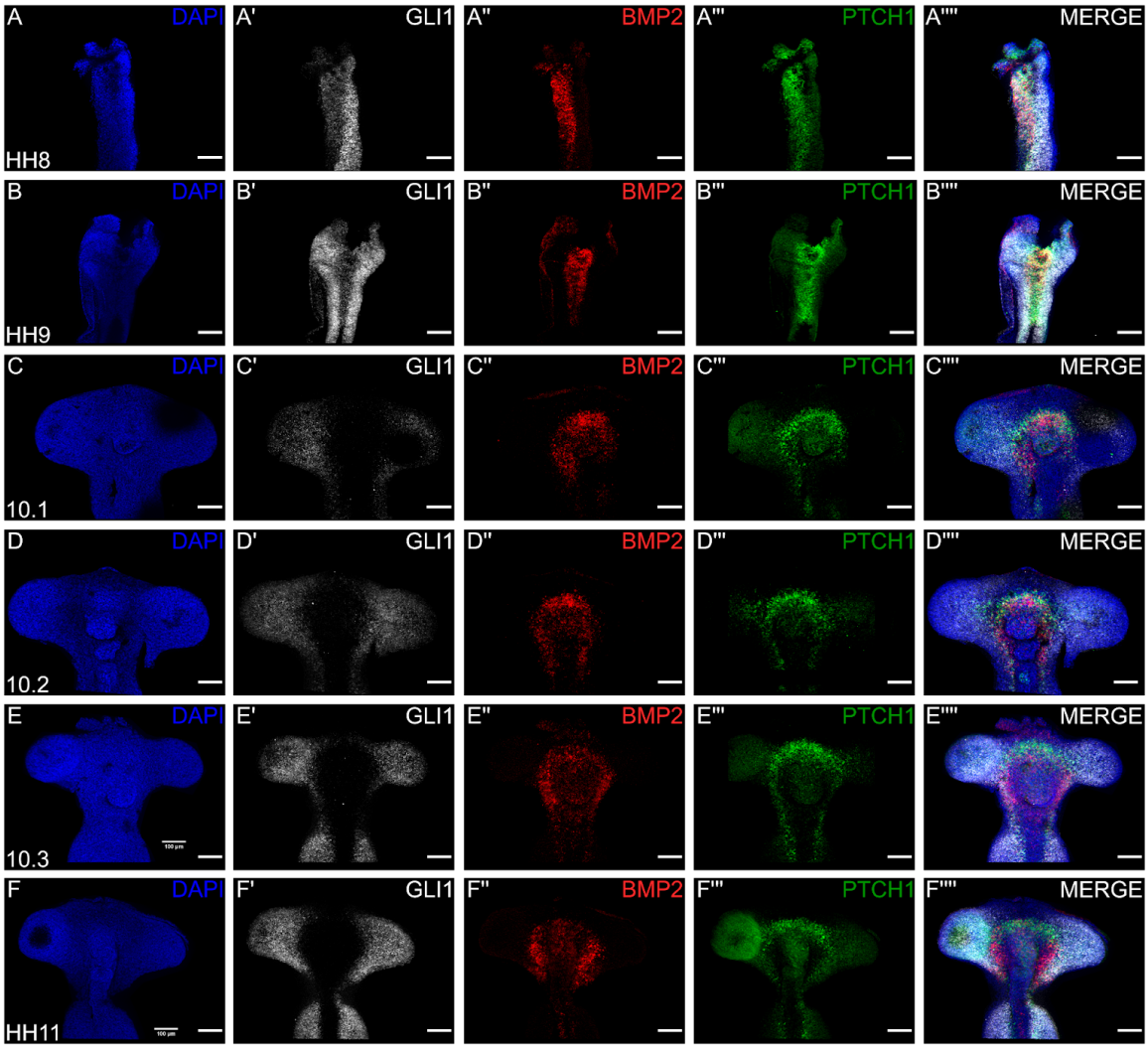

Figure 5.3 The spatial pattern of GLI1 does not explain regionalisation of *BMP2* and *PTCH1* in the developing hypothalamus at HH8-11. (A-F). All images show wholemount ventral views of isolated neuroepithelia analysed with HCR *in situ* hybridisation for *GLI1* (A'-F'), *BMP2* (A''-F''), and *PTCH1* (A'''-F'''). At HH8, *GLI1* was expressed in the midline, in the *PTCH1* and *BMP2* positive cells (A'), *BMP2* was also expressed in the developing hypothalamus, but not the gut endoderm (A''), and *PTCH1* was detected in the developing hypothalamus as well as more anteriorly in the gut endoderm (A'''). At HH09, *GLI1, BMP2, and PTCH1* continue to be expressed in developing hypothalamus cells. (B'-B'''). By HH10, *PTCH1* has begun to be downregulated posteriorly (C'''), with low expression in the centre of the V-face. At this stage, *BMP2* was still expressed in V-face (C''), and GLI1 expression was not detected (C'). Throughout HH10, *BMP2* shares a similar expression profile to *PTCH1*, with a radial arc of expression in the hypothalamic anterior V-face, but extends more posteriorly (D''-F''). *GLI1* expression continues to be undetected (D'-F'). At HH11, *PTCH1* expression had declined laterally and was detected as a band of expression running mediolaterally at the anterior edge of the developing hypothalamus (F'''), *BMP2* expression

was complementary to this, having declined anteriorly/medially, and strengthened laterally (F'').

These observations suggest the following hypothesis of *SHH, BMP2,* and *PTCH1* interactions that lead to the expression profiles detected. *PTCH1* becomes rapidly downregulated in midline-situated (A-fold and V-face) *SHH*-expressing cells. Potentially, the lack of PTCH1 supports the more efficient spread of SHH, which then induces further *PTCH1* expression in anterior and lateral cells, which in turn upregulate *SHH*. Concurrently, *BMP2* is becoming confined to posterior-lateral strips, where it inhibits *SHH* expression which in turn, results in the downregulation of *PTCH1* in that lateral tissue. This dynamic regulation of induction and cessation of SHH signalling, and *SHH* upregulation, could explain the radial expansion of *SHH*, and more generally how *SHH* is shaped in the developing hypothalamus.

5.2.4 *GLI1* expression supports the idea that there are different levels of SHH signalling in the V-face vs the posterior-lateral hypothalamus

The complex profiles of *SHH* and *PTCH1* prompted me to next examine the spatial organisation of a second SHH-target gene, *GLI1*. Transcription of *GLI1* in the nervous system is dependent on SHH (Bai *et al.*, 2002). Consequently, *GLI1* is normally not present to transduce initial SHH signalling, but I reasoned that it might provide clues as to the levels of active SHH signalling in different parts of the developing hypothalamus.

At HH8 and HH9, very low levels of *GLI1* were detected in *PTCH1/SHH*-expressing ventral midline cells, whereas high levels of *GLI1* were detected beyond these, in the ventral optic vesicles, where *PTCH1* is only weakly detected (Fig 5.2A', A''', Fig 5.3A'-B', 5.3A'''-B'''). Over stage 10.1-HH11, when *SHH* and *PTCH1* expression patterns had broken initial symmetry, *GLI1* is detected throughout the ventral optic vesicles and overlaps with *PTCH1* in lateral cells that express low levels of *PTCH1* (Fig 5.3C'-F', C'''-F''''); however, *GLI1* was not detected adjacent to the anterior arc of high *SHH/PTCH1* expression (i.e. in the V-face). These analyses support the idea that there are different levels of SHH signalling in the V-face, compared to posterior-lateral parts of the developing hypothalamus.

5.2.5 Early patterns of signalling ligands, and early morphologies, prefigure distinct hypothalamic progenitor populations

Having identified PTCH1 as a candidate for anterior spatial control of *SHH,* and BMP2 as a candidate factor for the control of posterior/lateral *SHH* expression in the developing hypothalamus at HH10-11, I next investigated whether these expression profiles persisted, predicting later progenitor regionalisation of the hypothalamus. As outlined in Chapter 1, by HH14, scRNA-seq analyses show that distinct hypothalamic progenitor cell types have formed: mammillary progenitors; posterior tuberal progenitors; and anterior tuberal (neurogenic) progenitors (Kim *et al.*, 2022). Previous studies that performed *in situ* hybridisation for *SHH* (including HCR), analysing side-views, have shown that these cell types occupy regionally-distinct domains, and have revealed the pattern of *SHH* in each (Manning *et al.*, 2006; Kim *et al.*, 2022). I now wanted to match my ventral wholemount views to these side-views. To do this I obtained an extended image series, analysing ventral wholemount views of *SHH* expression patterns relative to *PTCH1* and *BMP2* at later stages, from HH11-14 (Fig 5.4).

Throughout HH12-14, the developing hypothalamus expanded in size (Fig 5.4B-F). Despite this increase in size, I saw a consistent pattern in *SHH*, *PTCH1*, and *BMP2*. By HH12, *PTCH1* was expressed anteriorly in a mediolateral arc (Fig 5.4B'-F', G), with weak expression in the *SHH* expressing cells in the ventral midline cells (Fig 5.4C'-E', G). By HH14, *SHH* resolved into two populations: an anterior arcing population overlapping with the most medial *PTCH1* positive cells (Fig 5.4F'', blue arrowhead), and a posterior Y-shaped population of cells (Fig 4F'', green arrowhead), the lateral limits of which coincided with the lateral limits of the fold morphologies and the medial limits of *BMP2* expression (Fig 5.4F''', green arrowhead).

At the same time that I was conducting these studies, others in the Placzek lab were: (i) analysing *BMP2, FGF10* and *SHH* within the context of other markers; and (ii) performing fate-mapping studies. Briefly, these showed two points that are pertinent to my work. First, the transient high *BMP2* expression level that I observed at 10.1 coincides with the expression of *TBX2*, a marker of posterior tuberal progenitors. Second, the A-fold/V-face boundary marks a transition point, where floor plate-like cells undergo a profound change, migrating anteriorly and giving rise to tuberal progenitors that constitute the V-face (Figure 5.4F); cells that remain in the A-fold (and regions posterior and lateral to it) give rise to the mammillary hypothalamus.

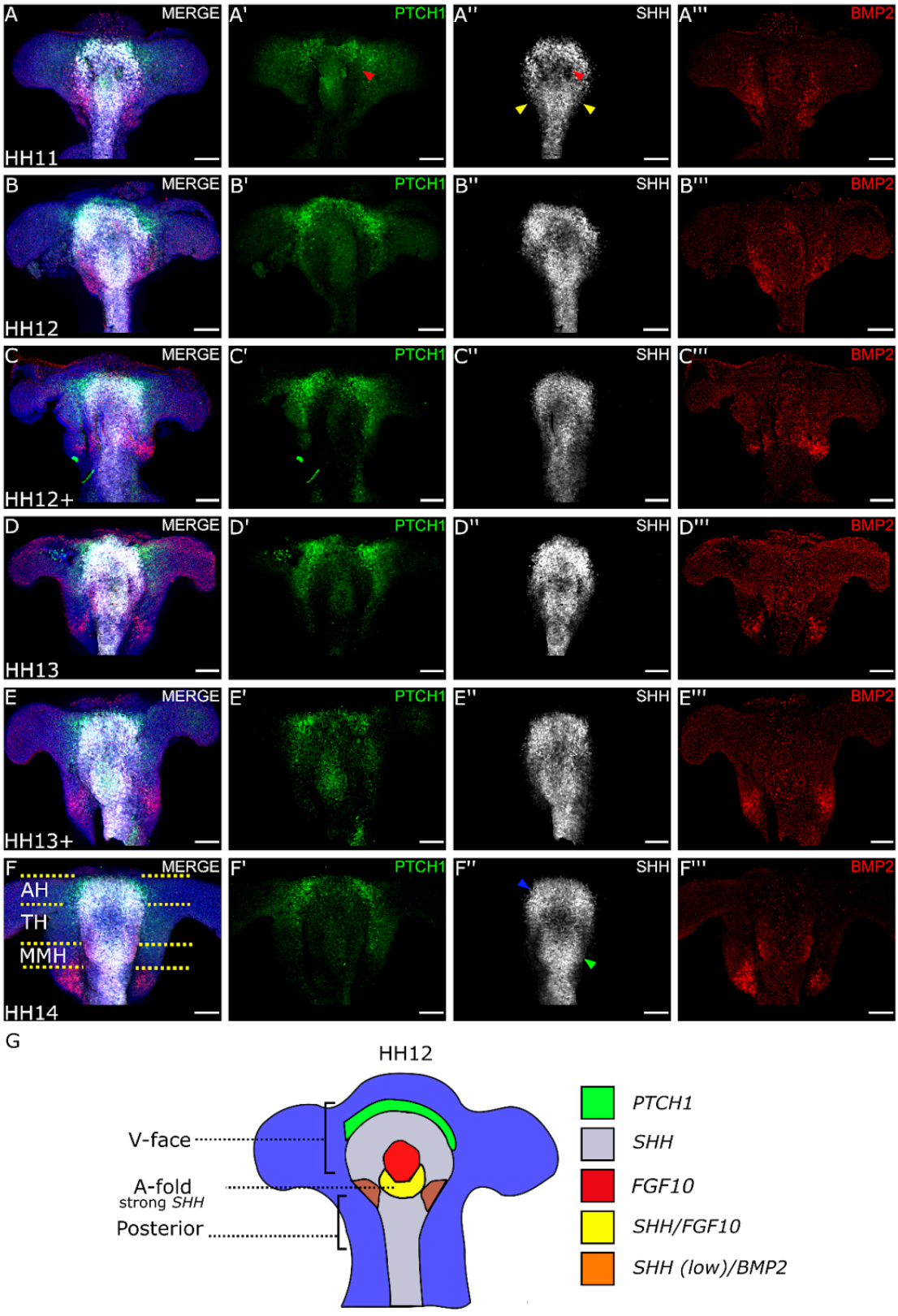

Figure 5.4: *PTCH1*, *SHH*, and *BMP2* organise in the developing hypothalamus throughout HH11-14. (A-F) Ventral views of isolated neuroepithelia from embryos at stages HH11-14. At HH11, *PTCH1 was* expressed in an anterior arc and has begun to decrease

lateral to the ventral midline (A'). *SHH was* expressed narrowly and has some overlap with *PTCH1* (A''). Similarly, *BMP2* overlaps, but extends more posteriorly and laterally (A'''). Between HH11 and HH12, the overlap between the *PTCH1* and the *SHH* domains was less pronounced, and *SHH* extends more laterally (B'-C'-B''-C''). *BMP2 was* no longer detected in the A-fold/V-face and was instead seen as two small bands of posterior, lateral expression (B'''-C'''). After HH12, the pattern is more stable, with the only marked difference that there were greater distances between the populations (E'-F', E''-F'', E'''-F'''). (G) Schematic summarising the regionalisation seen at HH12 in relation to the morphology identified in Chapter 4. Scale bars: 100μm.

These analyses revealed how the early subtle changes in expression detected over HH9-11, and the early morphological features that I described in Chapter 4, prefigure the regionally distinct domains at HH14. The region where *SHH* and *FGF10* overlap anteriorly (in the posterior V-face) predicts where tuberal progenitors appear as they develop from floor plate-like cells. The A-fold (where *SHH* is high, and *FGF10* is weakly detected) predicts the hypothalamic floor plate and future mammillary hypothalamus (Fig 5.4F, MMH; Fig 5.4F'', green arrowhead). Cells lateral to this domain expressed *PTCH1* only weakly, but expressed *BMP2.* Finally, the anterior arc of *SHH* and *PTCH1* appears to predict the anterior tuberal progenitor/neurogenic domain. No *BMP2* was detected at this axial level from HH11-14.

5.3 Summary

In this Chapter, I have investigated the molecular landscape of core morphogen-like signalling ligands relative to developing 3-D morphological features that I characterised in Chapter 4. In these Chapters, my overall hypothesis is that these ligands prefigure this morphology.

In contrast to previous conclusions (Fu *et al.*, 2017), *FGF10* and *SHH* were not initially co-expressed. Instead, *FGF10* and *SHH* initially showed reciprocal expression. Their overlap correlated with, and may predict the A-fold and the posterior V-face (Fig 5.5B). Additionally, I saw subtle regionalisation occurring across HH8-14. *SHH* breaks symmetry along the A-P axis, but does so only after the first signs of overt 3-D morphology (Fig 5.5B). Thus, after formation of the A-fold, SHH is downregulated in the posterior V-face and upregulated in an arc in the anterior V-face (Fig 5.5C).

As elsewhere in the neural tube, I observed that *SHH* expands laterally (Placzek *et al.*, 1993), and *a priori*, I expected to see a uniform radial expansion of *SHH*. However, the wholemount views showed a more complex pattern of *SHH* expression. Expression is weak in the regions next to the U-shaped A-fold (forming mammillary hypothalamus): these regions co-express *BMP2,* but strong in a more anterior arc (Fig 5.4F).

As also would be expected from expression in the neural tube, *SHH* and *PTCH1* are transiently expressed together in the ventral midline, then *PTCH1* is downregulated in *SHH*-expressing cells, and upregulated in adjacent cells (Marigo and Tabin, 1996). Surprisingly, levels of *PTCH1* are not uniform. Instead, a strong anterior arc is detected, beyond the *SHH*-expressing V-face arc (Fig 5.5B-C).

Prior to the development of any overt 3-D morphology, *SHH* and *BMP2* are co-expressed in developing hypothalamic cells (Fig 5.5A). As the A-fold and V-face become apparent, BMP2 begins to be expressed in a heart-shaped ring, overlapping with outermost SHH-expressing cells.

Multiplex analysis of *SHH, BMP2* and *PTCH1* show *BMP2* expression medial to *PTCH1*-domains (Fig 5.5B-C). In the apex of the heart-shaped ring - a region that marks/predicts the posterior V-face - *BMP2* is transiently expressed at high levels, before being downregulated here. *BMP2* expression then persists only lateral to the A-fold (Fig 5.5C).

In contrast to *PTCH1*, a second SHH-target gene, *GLI1,* was not detected in the ventral hypothalamus, but instead was detected in more lateral regions, where *PTCH1* levels are very low. No *GLI1* was detected in the forming V-face.

My studies suggest that at HH12, there are (at least) two *SHH* populations which are discrete spatially. One population comprises antero-tuberal progenitors and the second comprises mammillary progenitors that lie posterior/lateral to the *FGF10*-expressing cells. The spatial relationships of *SHH/PTCH1/BMP2* set up at HH10-11 appear to be consistent until HH14. This is surprising because the prosencephalon and generally the hypothalamus expands in size, but the relative proportions are kept constant, implying a degree of scaling in their expression.

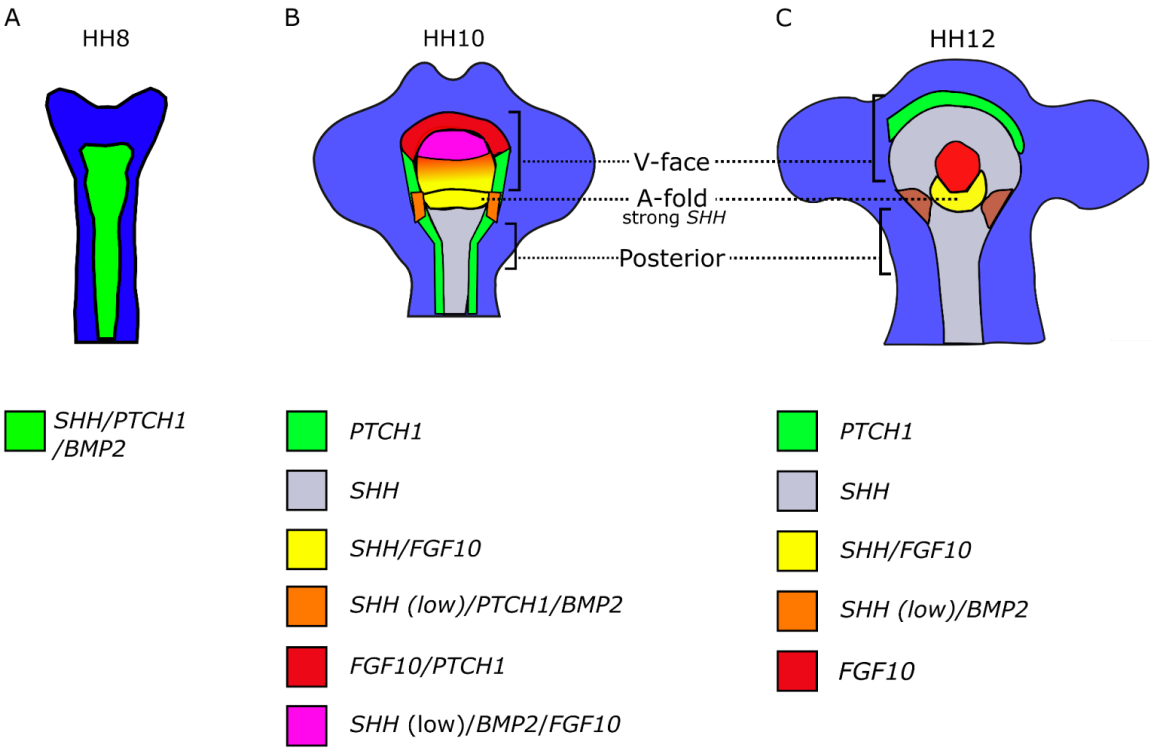

Figure 5.5 Summary schematic of symmetry breaking and regionalisation of *SHH*, *PTCH1*, *BMP2* in the early developing hypothalamus. (A) At HH8, *SHH*, *PTCH1*, and *BMP2* were expressed in the developing ventral midline hypothalamic cells. (B) During HH8-9, there was an onset of regionalisation, resulting in several distinct populations. (C) By HH12, there was a simpler profile, with 2-3 *SHH* expressing populations, *PTCH1* was confined to an anterior band, and *FGF10* had resolved into a *SHH/FGF10* population in the A-fold, and a central disc of expression in the centre of the V-face. *BMP2* was no longer detected anteriorly, and was expressed as two bands lateral to the A-fold/base.

Overall, the expression profiles of *SHH, FGF10, BMP2* and *PTCH1* over HH8-11 are complex, with multiple overlapping regions and heterogeneous levels of expression (Fig 5.2). As detailed in Chapter 6, I next sought a method of disentangling this complexity. To do this, I used *ex vivo* tissue culture of explanted developing hypothalamus cells, to examine whether the expression domains develop through mechanisms that are autonomous to the neuroepithelium

Ideally, I would have examined the profile of all four genes (*FGF10, BMP2, SHH, PTCH1*). However, the *FGF10* and *BMP2* probes were not easy to work with, as each has relatively few short hairpins (see Chapter 2). Preliminary experiments to visualise these expression

domains in isolated explants showed a poor signal to noise ratio (Appendix Fig 1). At this point, access to the lab was limited due to the COVID-19 restrictions, which meant that I could not resolve issues with optimising the HCR *in situ* for visualising *FGF10* or *BMP2.* The analyses in Chapter 6 were therefore limited to *SHH* and *PTCH1*: these probes that were more robust (greater number of hairpins).

Chapter 6

Characterisation of *ex vivo* expression of *SHH* and *PTCH1*

6.1 Introduction

In Chapter 5 I demonstrated the relative patterns of expression of *SHH* and *PTCH1* over HH8-HH14 *in vivo*. At HH8, *SHH* and *PTCH1* are both expressed in a rod of anterior ventral midline cells. By HH12, this symmetric arrangement is broken. Posteriorly, *SHH* is expressed in the U-shaped A-fold, while adjacent/overlapping cells express low levels of *PTCH1*. In the crook of the U-shaped A-fold - a region occupied by posterior tuberal progenitors - *SHH* is becoming downregulated. Anterior to these, *SHH* is expressed in an arc, just inside, and overlapping with a wider arc of cells that express high levels of *PTCH-1.*

A critical question is how *SHH* becomes organised into the pattern observed at HH12. Previous studies have shown that the underlying prechordal mesendoderm induces *SHH* expression in the developing hypothalamus (Dale *et al.*, 1997; Patten *et al.*, 2003). This occurs around HH6-HH10 during convergent extension. By HH10, cells of the prechordal mesendoderm are beginning to disperse (Jacob *et al.*, 1984; Seifert and Christ, 1990; Ellis *et al.*, 2015). I next set out to ask: is the organisation of *SHH*and *PTCH1* (and their subsequent correlation with morphology) a result of neuroepithelial or mesodermal influences?

To do so I set out to isolate hypothalamic explants, free from adjacent tissues, and then culture them *ex vivo*, with the following aims: (i) to assess to what extent the changes in expression profiles of *SHH and PTCH1* are a result of interactions within the neuroepithelium; and (ii) to develop an assay with which to perturb the patterning of *SHH and PTCH1* and by doing so begin to unpick the potential interactions between these factors.

6.2 Results

6.2.1 HH10 hypothalamic explants ball-up in culture, precluding analysis of regionalisation of *SHH*/*PTCH1*

My first aims were to both confirm the reliability and accuracy of my dissection, and to characterise the molecular properties of the explants prior to *ex vivo* culture, which would enable me to place them in the context of my wholemount views.

As a starting point, I attempted to dissect *SHH*-expressing hypothalamic progenitors from HH10. I began at HH10 because of my characterisation of HH10 morphology in Chapters 3-4, which made dissection of *SHH* and *PTCH1* expressing cells by-eye straightforward. Thus, I aimed to dissect neuroepithelium composed of the A-fold and V-face. Following this, I fixed the explants and labelled them for *SHH* and *PTCH1* via HCR *in situ* hybridisation.

My results showed I could accurately dissect the developing hypothalamus. Strong expression of *PTCH1* was detected along the top edge of the explants, with more weakly expressing *PTCH1*-positive cells overlapping with *SHH* expression in the centre of the explant (Fig 6.1A'-C'). In many of the explants, the U-shaped A-fold (strong *SHH*) could be detected, (Fig 6.1B''', C''', F''') indicating that the isolation does not result in an immediate change in morphology.

As expected from the results presented in Chapter 4, explants dissected but not cultured (t0) taken at the 10.1-3 sub-stages showed progressive regionalisation of *SHH* and *PTCH1* expression (Fig 6.1D-F). At 10.1, expression of *SHH* and *PTCH1* was detected in the centre of the explants, comprising the A-fold and posterior V-face (Fig 6.1A'-D', A''-D''). Strongest *PTCH1* expression was seen anteriorly, and in *SHH* low/negative cells. This complementary relationship progressed by 10.3, where *PTCH1* expression was greatly reduced in the *SHH* cells, and was only detected at the outer limit of the explant. (Fig 6.1F'-F'').

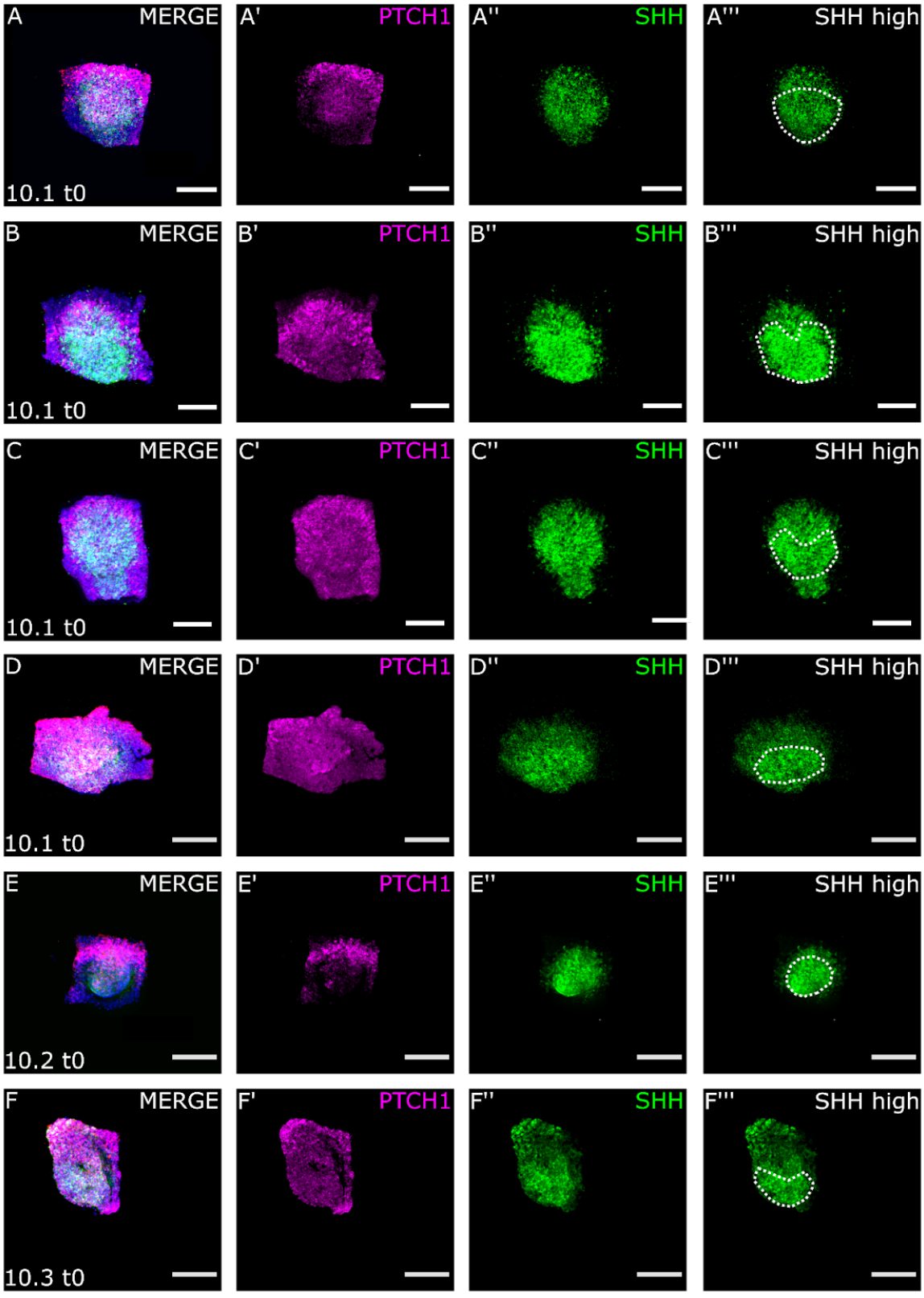

Figure 6.1 t0 explants show a progression of regionalisation of *SHH* and *PTCH1*. All panels show wholemount ventral views of dissected neuroepithelia (10x). (A-F) explants taken from progressively older embryos through 10.1-10.3, labelled for *SHH* and *PTCH1*.

(A’-F’) Throughout the stage 10 sub-stages, *PTCH1* and *SHH* expression domains transitioned from initially overlap substantially to being mostly mutually exclusive. In many explants, the U-shaped A-fold could be detected). Scale bars 100μm.

Taken together, my results from the HH10 t0 explant dissection characterise the initial state of the HH10 explant prior to culturing - an important baseline by which to compare against. I showed I was able to accurately and reliably dissect *SHH/PTCH1* positive cells over the HH10 substages. Following this, I set out to characterise the progression of *SHH/PTCH1* expression in cultured explants, starting with explants cultured for 24 hours (henceforth, t24 explants).

To this end, I dissected neuroepithlia at HH10, again using the morphological landmarks of the A-fold/V-face as a guide. I then embedded these into collagen beds (Dale et al., 1997, Placzek et al., 1993; Section 2.2.3), and cultured them for 24 hours, before fixing and visualising *SHH* and *PTCH1* expression via HCR *in situ* hybridisation (Fig 6.2).

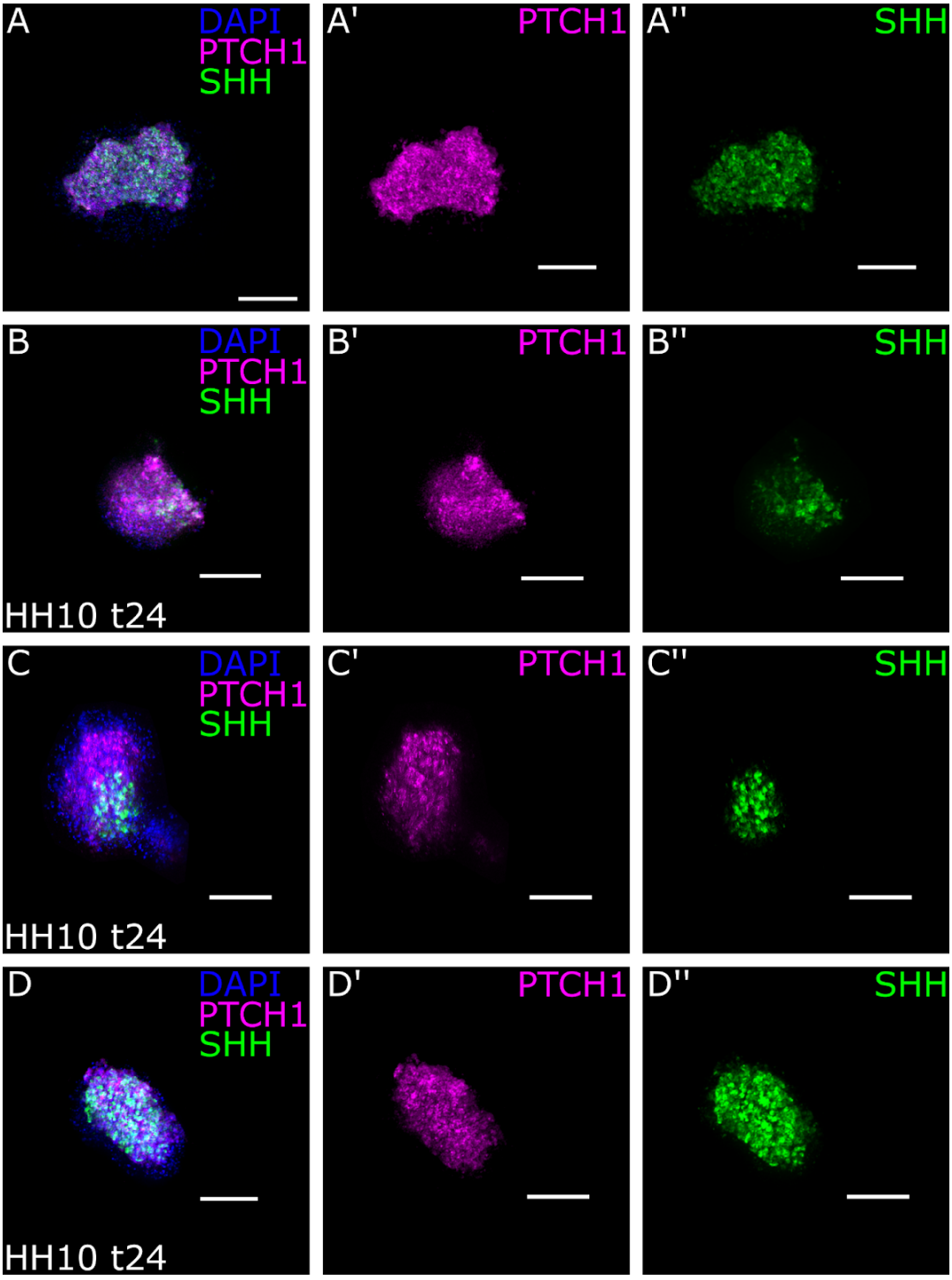

Figure 6.2. HH10 t24 explants show co-expression of *SHH* and *PTCH1*. All panels show wholemount views of cultured explants (10x). (A-D) explants cultured for 24 hours, labelled for *PTCH1, SHH,* and *BMP2*. (A'-D') *PTCH1* expression showed no obvious regionalisation, and was expressed through most of the explant. (A''-D'') *SHH* expression varied; there were some explants which exhibited regionalisation (B'', C'') whereas in others *SHH* was also expressed throughout the explant (A'', D''). (A'''-D'''). Scale bars 100μm.

The explants did not grow in size substantially after 24 hours of culturing, but did transition from a flat, monolayer epithelium into more spherical tissue (Fig 6.2A-D).

I did not see any discrete regionalisation of *SHH* and *PTCH1*. In 4/4 explants, *SHH* and *PTCH1* overlapped. (Fig 6.2A'-D', 2A''-D''). In two of these, *PTCH1* and *SHH* were expressed uniformly throughout the explants (Fig 6.2A', D', 2A', D''). And, in the other two, *SHH* was not expressed uniformly throughout the explant, but in a smaller area than *PTCH1*, suggesting the beginning of regionalisation (Fig 6.2B'-C', B''-C'').

Overall, I did not see the expected regionalisation of *SHH* and *PTCH1* in the HH10 t24 explants. I did observe the potential beginning of regionalisation, but all explants had substantial or total overlap of *SHH* and *PTCH1* expression. I reasoned that this could be due to two factors: (i) the HH10 dissection was technically difficult and following dissection, the cells in the tissue were inactive (due to chilling to 4℃) for some time after implantation into the collagen matrix, hence the HH10 t24h culture may not reflect 24 hours post HH10 development; (ii) the tendency of the HH10 explants to curl into a ball may have obliterated any regionalisation that had occurred.

Due to these factors, I next set out to isolate explants from younger stages: HH8 and HH9 embryo: the anterior midline/prospective hypothalamus is simpler (and therefore quicker) to dissect at these stages, when the folds have not yet formed. At HH8 expression of *SHH* and *PTCH1,* appear relatively uniform, and at HH9, expression of *SHH* and *PTCH1* are only slightly regionalised into distinct parts of the tissue (Chapter 5). Following this, I planned to culture these for longer - 48 hours.

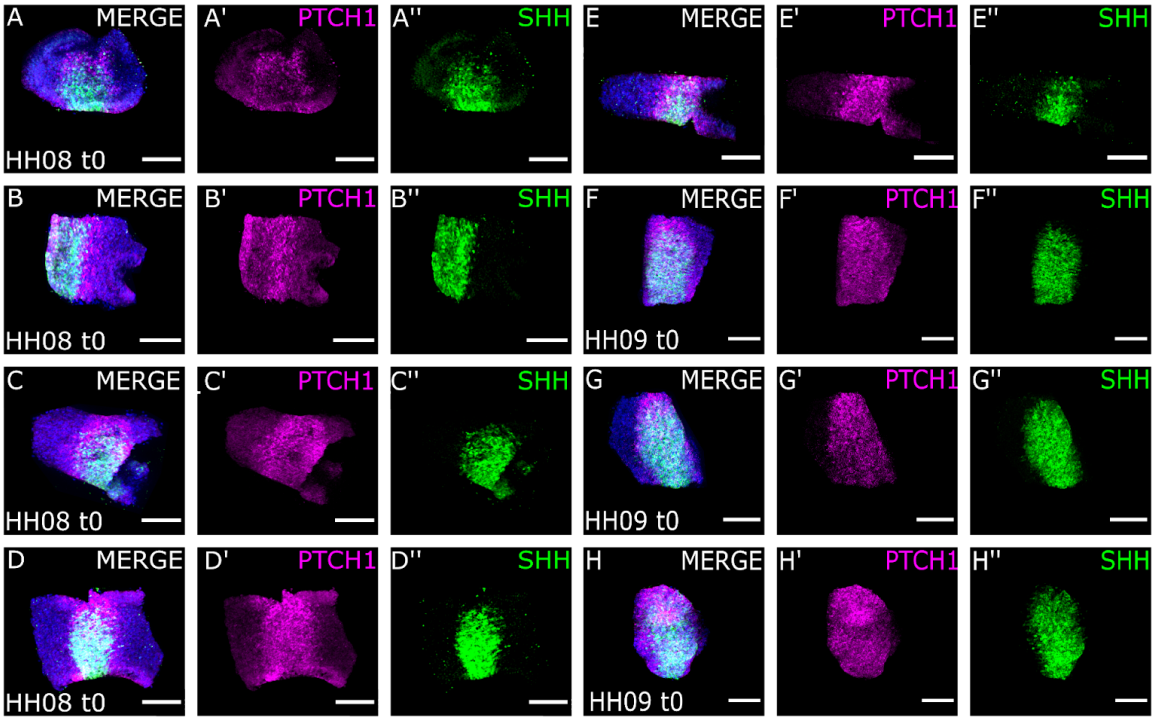

Figure 6.3. HH8-9 t0 explants have overlapping expression of *SHH* and *PTCH1*. All panels show wholemount ventral views of dissected neuroepithelia (10x). (A-E) explants taken from HH8 embryos, labelled for *PTCH1* (A'-D') and *SHH* (A''-D''). *PTCH1* was expressed uniformly throughout the middle of the explant, occasionally with slightly stronger expression laterally. (A'-B'), the *SHH* expression domain was uniform and overlapped almost entirely with *PTCH1* (A''-D''). (F-H) explants taken from HH9 embryos labelled for *PTCH1* (F'-H') and *SHH* (E''-H''). *PTCH1* expression was throughout the middle of the explant, overlapping with *SHH*, with a slight non uniformity, where *PTCH1* expression was slightly anterior to *SHH* expression. Scale bars 100µm.

6.2.2 *SHH* and *PTCH1* already show some regionalisation at HH8-HH9

I dissected explants from HH8 or HH9 and fixed them without culturing, and then visualised the expression of *PTCH1* and *SHH* using HCR *in situ* hybridization (Fig 6.3). Henceforth, I refer to these as HH8-9 *t0 explants*. At HH8, I detected *SHH* expression in the centre of each explant (Fig 6.3A''-E'', n=5). In 3/5 explants, *PTCH1* expression appeared uniformly distributed with expression extending slightly around the *SHH* domain (Fig 6.3B', D', E'); in 2/5 explants, *PTCH1* expression appeared slightly stronger along one edge (Fig 6.3A', C') In all 3 explants isolated at HH9, *SHH* and *PTCH1* were expressed throughout most of the explant, with *PTCH1* extending slightly outside of the *SHH*/*PTCH1* domain(Fig 6.3F'-H',

F''-H''). Qualitative inspection suggested that *SHH* and *PTCH1* were expressed in complementary gradients (compare Fig 6.3F'-H' with F''-H''). These results confirmed a conclusion from Chapter 5, that *SHH/PTCH1* are already beginning to organise into discrete domains by HH9.

A trade-off from explanting at HH8 compared to HH10 is that there are substantially fewer morphological landmarks at HH8. This means there is a greater risk of contamination from neuroepithelium outside of the target area. Nevertheless, my results show a clear picture of the landscape of *SHH* and *PTCH1* expression in the HH8 t0 explant, I therefore next aimed to culture them to determine if substantial growth and regionalisation occurred *ex vivo*.

6.2.3 *SHH* and *PTCH1* regionalise *ex vivo* into distinct domains

To do this, I next dissected prospective hypothalamic explants from HH8 and HH9 embryos, cultured them for 48 hours and labelled them as before for *SHH* and *PTCH1* via HCR *in situ* hybridization, terming these the *t48 explants* (Fig 6.4). I found regionalisation between *SHH* and *PTCH1* in every cultured explant (n=3/3 at HH8, 3/3 at HH9). At HH8-9 t48, 3/3 explants were spherical, each showed *PTCH1* expression in an arc above *SHH* expression (Fig 6.4A'-A'', C'-C'', D'-D''). In each of these spherical explants, *SHH* expression was detected as a disc, overlapping slightly with the *PTCH1* arc (Fig 6.4A, B, C).

At HH9, all explants exhibited regionalisation of *SHH* and *PTCH1* expression. *PTCH1* was expressed in regions largely separate to *SHH* expression, but with overlap (Fig 6.4D-F). Within each explant the area occupied by *SHH* or *PTCH1*-expressing cells varied, perhaps reflecting subtle variation in the area isolated at t=0. (cf. Fig 6.4F', F'' and 6.4E', E'').

Having established HH8 as an optimal stage for explanting to assess organisation of *SHH* and *PTCH1*, I next sought to understand the stability of the observed regionalisation of *SHH* and *PTCH1*. *In vivo*, the developing hypothalamic tissue grows substantially between HH8-14. Despite this increase in size, I only observed a single, radial boundary between *SHH* and *PTCH1* i.e. *PTCH1 was* always expressed in an arc around the disc shaped *SHH* expression at t=48h. In other developing tissues, e.g. in the developing rugae (regular folds of tissue) of the palate *SHH* and *PTCH1* are expressed in periodic stripes (Lee *et al.*, 2011; Xu *et al.*, 2016). However, in the developing hypothalamus, I observed a constant pattern of *SHH* and *PTCH1*, and therefore I hypothesised that the regionalised explants would also exhibit a constant pattern.

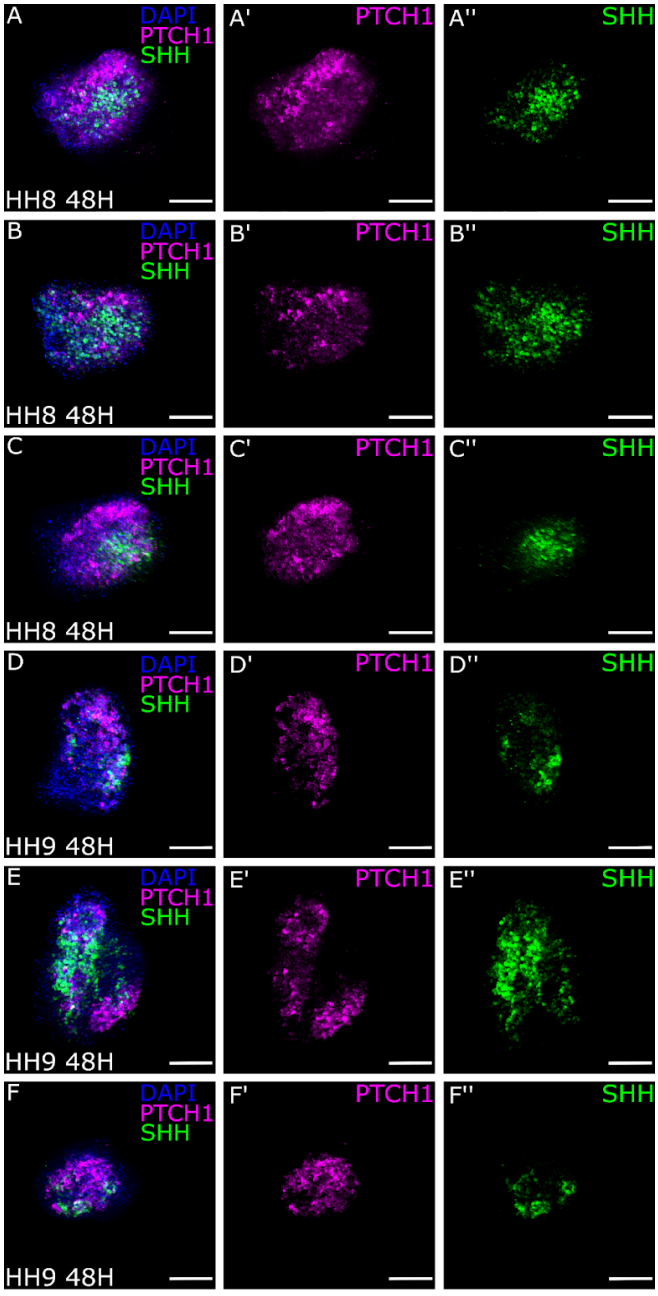

Figure 6.4 Explants taken from HH8-9 embryos and cultured for 48 hours exhibit organisation of *SHH* and *PTCH1* expression. (A-F) All panels show wholemount views of cultured (48h) explants (10x) labelled via HCR *in situ* hybridisation for *PTCH1* (A'-F') and *SHH* (A''-F''). At HH8 t48, *PTCH1* and *SHH* regionalise and are not expressed uniformly throughout the explant (A'-G', A''-F''), however in some cases their expression domains overlap (B', B''', D', D'''). At HH9 t48 *PTCH1* and *SHH* also regionalise, and there are also examples of overlap between *SHH* and *PTCH1* (D'-F', D''-F''). Scale bars 100μm.

6.2.4 *SHH* and *PTCH1* regionalisation is maintained throughout explant growth

To test this hypothesis, I next dissected explants at either the 4, 5, or 6 somite stage, and cultured them for 72 hours. (Fig 6.5), and termed these *t72 explants*. As there was relatively little growth of the t24 explants described above, I estimated that these were approximately equivalent to E3 in development (HH8: 26-29h + 72h - 24h stasis = approx 74 hours). I found, as with the HH8 48h explants that *SHH* and *PTCH1* regionalised into distinct domains (Fig 6.5A'-J', A''-J'').

Explants taken from embryos with 4 somites displayed a constant pattern of *SHH* and *PTCH1* expression, and in these *SHH* and *PTCH1* expression were mutually exclusive (Fig 6.5A'-C', A''-C''). However, there was variability in the relative proportion of the explant that was *SHH/PTCH1* positive. In one case, *SHH* and *PTCH1* together occupied the entire explant (Fig 6.5B'-B''), whereas in the other HH8 4-somite explants they were only expressed in a smaller proportion of the tissue (Fig 6.5A'-A'', C'-C''). In these cases, the majority of the *SHH/PTCH1* negative explant tissue lay adjacent to *PTCH1* expression but not *SHH* expression, possibly reflecting anisotropic anterior expansion *in vivo*.

At 5 somites, I observed the only explant which appeared to have two stripes of *PTCH1* expression, one large, comprising approximately half the tissue, and one small in the opposite end of the explant (Fig 6.5D'). Here, *SHH* expression was situated between these two regions (Fig 6.5D'').

However, this was the only example of multiple domains of *PTCH1* expression. In the 6 somite t72 explants, I only observed single domains of both *PTCH1* and *SHH* expression (Fig 6.5E-J). There did not appear to be a clear pattern as to whether the expression domains of *PTCH1* or *SHH* were larger. In some cases,the *PTCH1* expression domain was substantially larger than the *SHH* expression domain (Fig 6.5H'-J', H''-J''). Conversely, the *SHH* domain was sometimes larger than the *PTCH1* domain (Fig 6.5 E'-E'', F'-F''). Whilst less clear than in the 4 somite t72 explants, the tissue negative for either *SHH* or *PTCH1* lay next to the *PTCH1* expression domain (Fig 6.5E-I, white arrowheads).

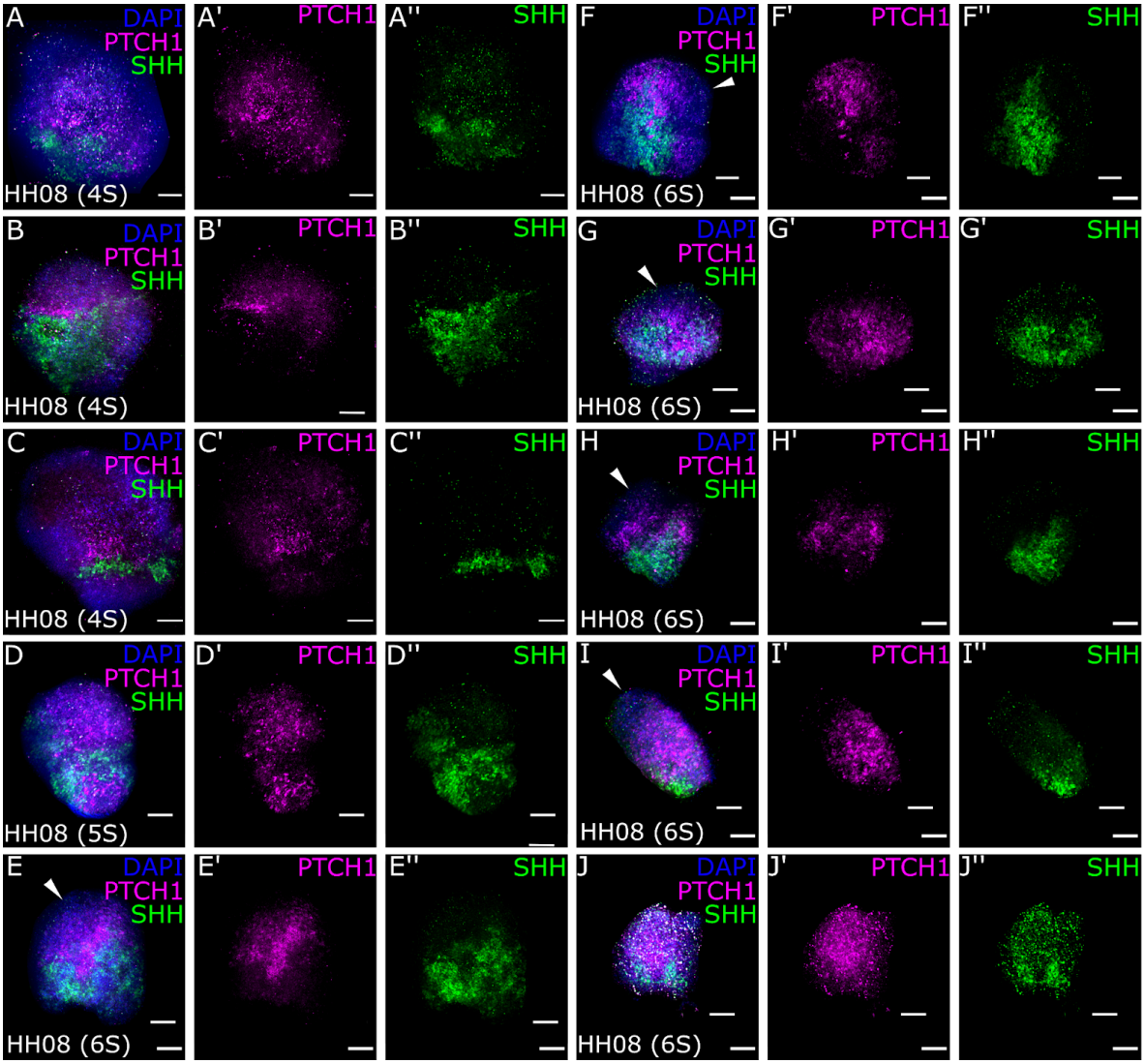

Figure 6.5. Explants taken from HH8 embryos at 4-6 somites, cultured for 72 hours, exhibit organisation of *SHH* and *PTCH1* expression. (A-J) All panels show wholemount views of cultured (72h) explants (10x) labelled via HCR *in situ* hybridisation for *PTCH1* (A'-J') and *SHH* (A''-J''). At HH8 (4 somites) t72, *PTCH1* and *SHH* regionalised substantially but did not comprise a substantial portion of the overall tissue (A'-C', A''-C''). At HH8 5 somites, there were two domains of *PTCH1* expression which surrounded the *SHH* expression (D'-D''). At HH8 6 somites *PTCH1* and *SHH* also regionalise, with discrete domains of expression (E'-J', E''-J''). Scale bars 100μm.

Overall, I have shown here that the expression domains of *SHH* and *PTCH1* break symmetry *ex vivo,* which lends support to the model presented in Chapter 4 - that interactions between PTCH1 and SHH in the neuroepithelium organise *PTCH1* and *SHH* into discrete domains of expression. Additionally, as the explants are permitted to grow large

and are not constrained by normal developing hypothalamic/brain morphology, I can assess the effect of unconstrained tissue growth on the regionalisation of *SHH* and *PTCH1.*

I next set out to understand whether the *SHH/PTCH1* regionalisation phenomenon reflected a retention of the anteroposterior axis throughout explant development.

6.2.5 Lineage tracing shows explants retain anterior-posterior memory

To assess anteroposterior axis retention, I dissected explants taken from neuroepithelia at HH8, and injected them with the fluorescent cell dye DiI, targeting the anterior edge. After DiI injection, I cultured these explants for 72h as prior, visualising *SHH* and *PTCH1* expression to examine their relative expression patterns compared to the *initial* anterior edge of the explant (Fig 6.6).

DiI incorporated successfully into cells in the explants, and was located in/anterior to the *PTCH1* expression domain (Fig 6.6A'-D', A'''-D''' n=4/4). Supporting the conclusions from my analysis in Sections 5.2.4-5, *SHH* and *PTCH1* were expressed complementarily and were largely mutually exclusive (Fig 6.6B'-D', B''-D''). In the smallest of these explants, *SHH* and *PTCH1* overlapped partially (Fig 6.6A'-A''). However, DiI was still found only in *PTCH1* expressing cells (Fig 6.6A'''), and the merged views show clear regions of expression of *SHH* and *PTCH1* (Fig 6.6A), suggesting that *SHH* and *PTCH1* were in the process of regionalising into mutually exclusive domains in this explant.

SHH and *PTCH1* were already beginning to be regionalised along the anterior-posterior axis by HH8.It is possible that this non uniformity is responsible for the consistent regionalisation of *PTCH1* at the anterior of the explant. I therefore next set out to dissect explants from younger embryos.

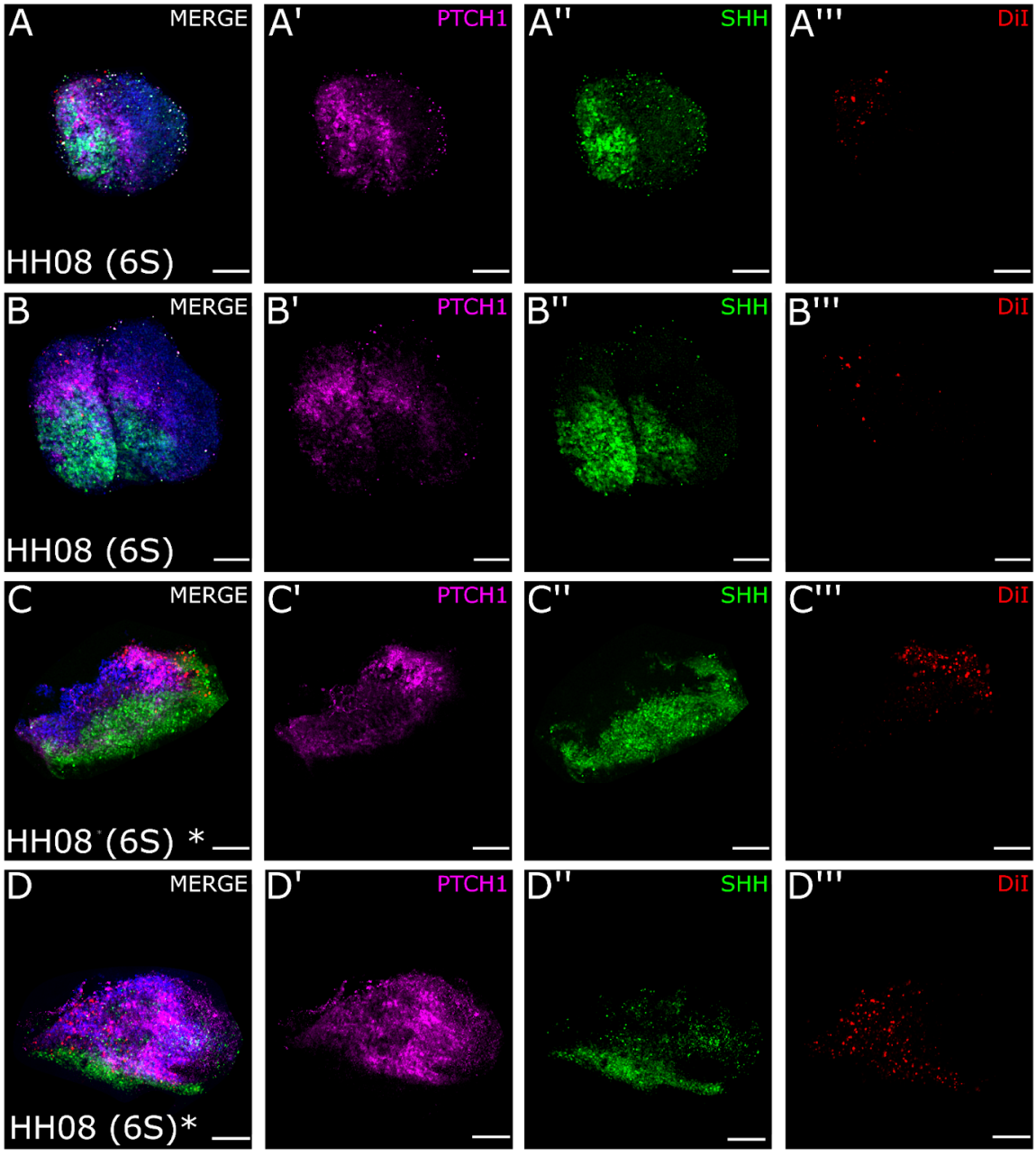

Figure 6.6. HH8 explants cultured for 72 hours retain the relative anteroposterior axis. (A-B) panels show wholemount views of HH6 explants cultured for 72 hours, (C-D) panels show mid optical sections from wholemount stacks of HH6 explants, denoted by *. All panels show explants labelled via HCR *in situ* hybridisation for *PTCH1* (A'-D'), *SHH* (A''-D''), and via injection for DiI (A'''-D'''). In the HH8 t72 explants, *PTCH1* and *SHH* organise into distinct domains of expression (A'-D', D''-D''). DiI injected into the *initial* anterior of the explant now labels the *PTCH1* expression domain but not the *SHH* (A'''-D'''). Scale bars 100μm.

To do this, I dissected HH6 explants (Fig 6.7; n=3). I did not fix t0 explants for this stage, but the wholemount views of isolated neuroepithelia showed that at HH6, *SHH* was expressed in a rod of ventral midline cells, tapering off anteriorly (Fig 6.7A, A") and *PTCH1* was detected weakly and uniformly throughout and beyond these (Fig 6.7A, A'). The ventral midline was very obvious at HH6, as it is translucent, and for dissection I targeted a square patch of tissue around the anterior-most ventral midline (Fig 6.7A, boxed area).

After dissection, I targeted DiI to the anterior edge of each explant, and then cultured each for 72h (Fig 6.7B-D), visualising via HCR *in situ* for *SHH* and *PTCH1* expression (Fig 6.7B'-B"', D'-D"'). I estimated the developmental stage of the explants as approximately HH17+ (HH6: 23-25h + 72h - 24h stasis = approx 71 hours). In 2/3 explants, I observed an unexpected pattern to *SHH* expression: it was expressed in a Y-shape. In all 3 explants I observed substantial regionalisation of *SHH* and *PTCH1* (Fig 6.7B'-B" - 7D'-D"), whereby they resolved into distinct domains with little overlap. In the 2 explants in which Y-shaped *SHH* was detected, *PTCH1* appeared between the 'arms' of the Y-shape. DiI was observed in the *PTCH1* expressing tissue, indicating this to be the anterior part of the explant (Fig 6.7B"'-D"').

The cultured HH6 explants therefore appeared to show aspects of neuroepithelial self-organisation. First, a rod of *SHH* appears to become organised into a Y-shaped domain over time. Second, *PTCH1* becomes organised into a region anterior to *SHH*.

Overall, the HH6 t72 explants support the conclusion from the HH8 t72 explants: that the cells in the explants retain their relative antero-posterior axis, and suggest that the *initial* anterior after culture was where there was *PTCH1* expression and not *SHH.* The results presented here provide a basis for experiments unpicking organisation in hypothalamic development.

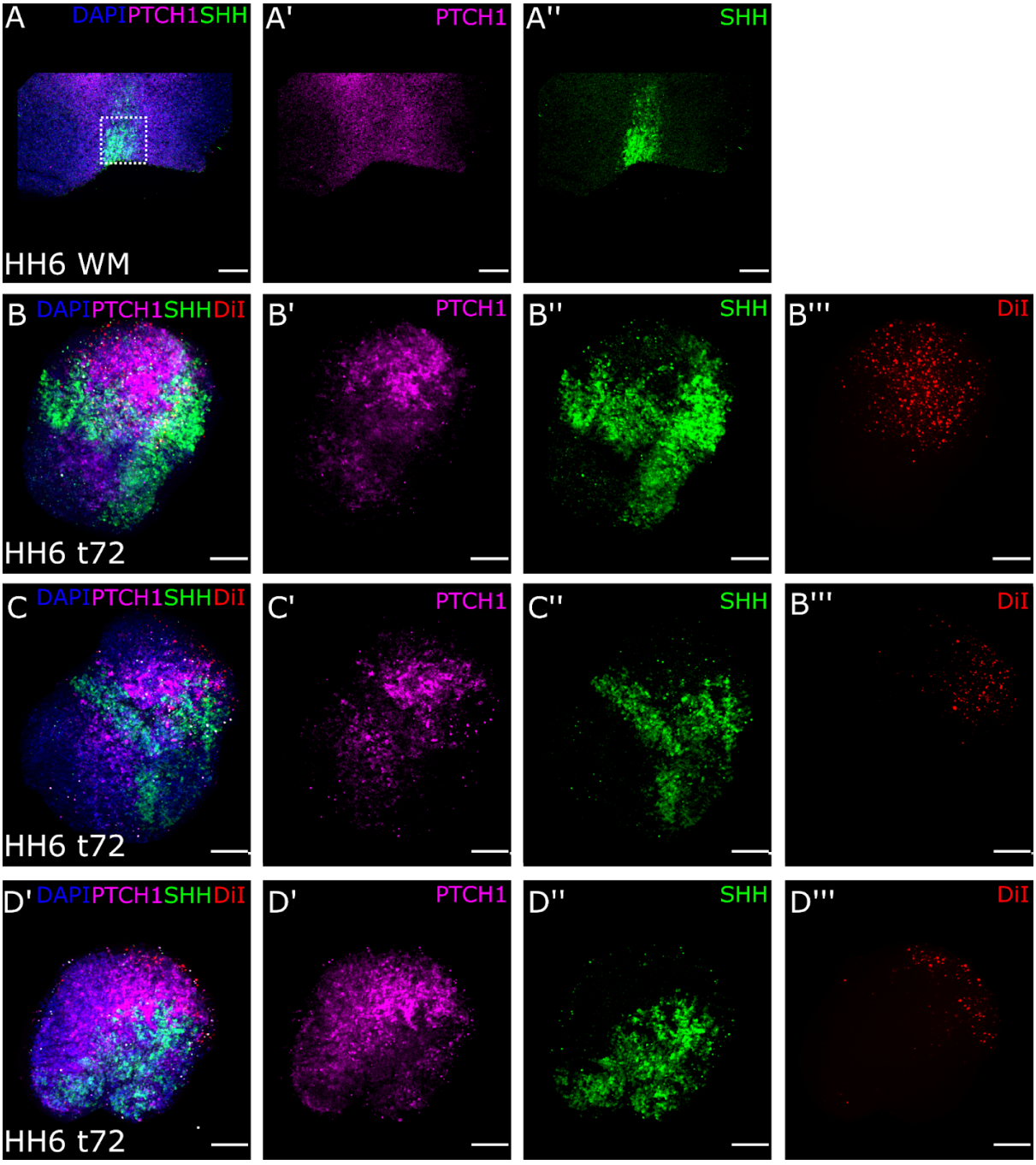

Figure 6.7. *PTCH1* marks the initial anterior of HH6 explants, cultured for 72 hours. (A) wholemount ventral view of a neuroepithelium from an HH6 embryo labelled via HCR *in situ* hybridisation for *PTCH1* (A') and *SHH* (B'). (B-D) wholemount views of cultured (72h) explants labelled via HCR *in situ* hybridisation for *PTCH1* (B'-D'), *SHH* (B''-D''), and via DiI (B'''-D'''). *In vivo, PTCH1* and *SHH* are expressed uniformly around the ventral midline (A-A''), *PTCH1* was expressed wider and at relatively lower levels compared to *SHH* (A'-A''). In the HH6 t72, *PTCH1* and *SHH* regionalise into distinct domains of expression (B'-D', B''-D'') with little overlap. *PTCH1* was expressed in tissue which was labelled as initially anterior at t0 by DiI (B'''-D'''). The DiI labelling was located in the *PTCH1* expressing tissue

which was at the interface with the *SHH* expression domain. All magnifications 10x. Scale bars 100μm.

6.2.6 *Follistatin* expressing cells are discrete from *Shh*-expressing ventral midline hypothalamic cells at HH8-12

At the same time that I was conducting my studies, the Placzek lab was conducting a large scRNA-seq analysis of chick hypothalamic development (Kim *et al.*, 2022). This study showed that the hypothalamus is induced from prethalamic-like diencephalic cells, that can be characterised through expression of follistatin (FST). This study also revealed that FST can inhibit hypothalamic induction (Kim *et al.*, 2022). A future aim would be to ask whether *SHH*-expressing prosencephalic ventral midline cells can intrinsically drive the altered expression patterns of *SHH and PTCH1* that are found *in vivo*, and as a first step towards this, I examined the profile of *SHH* relative to *FST*.

I therefore performed double-label HCR analysis to compare the profiles of *FST* and *SHH* in wholemount neuroepithelia between stages HH8-11+ (Fig 6.8). I found that at every stage, *FST* and *SHH* expressing cells were mutually exclusive (Fig 6.8A-G). At HH8-9, *SHH* and *FST* directly abutted each other at their medio-lateral extents (Fig 6.8A'-C', A''-C''). By HH11, *SHH* and *FST* were still mutually exclusive, but a substantial gap was detected mediolaterally between the *SHH* and *FST* expression domains, with *FST*-expressing cells confined to the anterior optic vesicles by the end of HH11 (Fig 6.8G, G''). Strikingly, comparison with wholemount embryos analysed in Chapter 5 showed, the cells in the *FST/SHH* negative gap were expressing *BMP2* and *SHH* (Fig 5.3 E'''-F''').

Overall, characterisation of the *FST* expression domain across HH8-11 showed that *FST* and *SHH* cells are mutually exclusive at these stages. However, their close proximity means that it is likely that my explants (certainly those at HH6-HH8) would have some contamination from more lateral *FST*-positive tissues. Further work should develop an understanding of whether the results reported here are due to the presence of *FST* expressing cells in the initial culture.

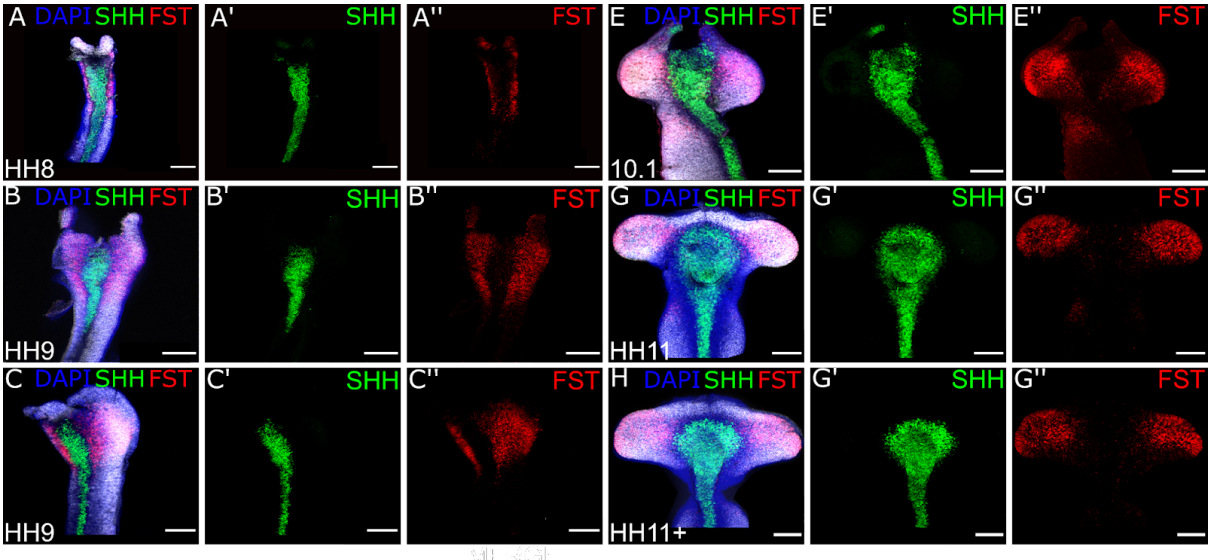

Figure 6.8: *SHH* and *FST* are mutually exclusive in the developing chick brain between HH8-HH11. (A-H) Ventral views of isolated neuroepithelia from embryos at stages HH8-12, processed for HCR in situ hybridisation for *SHH* (A'-H'), and *FST* (A''-H''). Prior to HH10, the *SHH* positive cells abutted *FST* positive cells mediolaterally (A'-C', A''-C''). Between HH9 and 10.1 a small lateral gap between the *SHH* and *FST* positive cells was established (D'- E', D''-E''). After HH10, the gap between *SHH* and *FST* positive cells widened (F'-G', F''-G''). Scale bars 100μm.

6.3 Summary

I was able to dissect hypothalamic explants at HH08-10 with a high degree of accuracy - previous work has used hypothalamic explants but a key novelty here is a thorough characterization of the base state of the explants - the t0.

SHH and *PTCH1* regionalise in a neuroepithelial intrinsic manner after 48h in culture. Neuroepithelial intrinsic SHH is important in hypothalamus development (Szabó *et al.*, 2009) but my results here suggest that the expression of *SHH* also organises in a neuroepithelial intrinsic manner, which could be a potential ongoing regulating mechanism for the effects of SHH when the interface between the neuroepithelium and the prechordal mesoderm is lost. Surprisingly, there did not seem to be a clear rule whether the HH8 t72 cultures expressed predominantly *SHH* or *PTCH1*. Re-examining the t0 HH8 cultures, this could be due to the heterogeneity along the anteroposterior axis, which suggests that the regionalisation between *SHH* and *PTCH1* is highly sensitive.

Additionally, the largest amount of tissue in the HH8 t72 explants always seemed to be on the *SHH* negative border with *PTCH1* expression (rather than on the other side of the *SHH* positive). This is important, as it hints that expansion of the explant always occurred on the side of the explant contralateral to *SHH* positive cells.

The hypothalamus first grows anteriorly, through the expansion of anterotuberal progenitors. It may be that the contralateral tissue reflects this and the explants have organised anteroposteriorly as they would *in vivo*, where PTCH1 is always expressed anterior to SHH (after HH8). To support this hypothesis, I used DiI lineage tracing to mark the anterior, finding that the anterior does coincide with the *PTCH1* expression at both HH8 and HH6. This was surprising, as at HH6 there is no obvious upregulation of *PTCH1* anteriorly (which, whilst small at HH8, may be enough to ensure anterior patterning).

A result that I did not expect from the HH6 t72 explants was that the expression domain of *SHH* was often Y-shaped. This is important, as it implies not only can these explants self organise along the anteroposterior axis, but also that there is a degree of mediolateral self organisation. This is reminiscent of the *in vivo* pattern of *SHH* over HH10-14 described in Chapter 5, where I showed that the posterior tuberal region showed a U-shaped *SHH* expression along the A-fold. Intuitively, this U-shape could be the same/very similar patterning to the Y-shape seen in the HH6 t72 explants.

Chapter 7

Discussion

In Chapter 1 I outlined several open questions to be tackled in this thesis. Here I summarise my results in the context of those questions:

1. **Can DNNs be used to sub-stage the developing chick brain in a more fine-grained manner than conventional staging methods?**
   To address this question, I first characterised a subtle staging problem in the developing HH10 chick embryo brain. I characterised a way of tackling this problem using the sub-stages 10.1-3. I then assessed the extent to which these sub-stages were linked to somite number, finding it to be an unreliable indicator of prosencephalic morphology. I then developed a deep neural network based image classifier to stage HH10 embryos according to these sub-stages. To obtain an accurate classifier, I tested several network architectures, and systematically examined the utility of a large variety of augmentations (Chapter 3).
2. **What is the structure of the early tissue morphology when the hypothalamus is being a) specified and b) organised into distinct progenitor regions?**
   To answer this, I conducted a fine-grained morphological study of the developing chick embryo at HH10, focusing on the ventral developing hypothalamus cells/tissue. I used a variety of methods to identify and further characterise morphological structures, finding that during/immediately after hypothalamic specification (HH8) a prominent fold develops at HH9 (the A-fold), and there was a relatively larger and flatter region anterior to this, termed the Ventral face (V-face) (Chapter 4).
3. **What are the earliest signs of regionalisation that prefigure the organisation of the hypothalamus into anterior and posterior tuberal, and mammillary progenitor domains?**
   Having found this morphology, I next tackled this question by investigating whether there were key molecular events that prefigured and correlated with this morphology. I visualised genes which were important to early hypothalamus development: *SHH*, *PTCH1, BMP2, GLI1*. Finding substantial regionalisation, which in many cases coincided with the morphology I described in Chapter 4, I provide novel insights into the complicated spatial expression of these genes (Chapter 5).
4. **To what extent is the regionalisation of the developing hypothalamus intrinsic, or does it rely on external factors (e.g. from the PM)?**

To address this, I used *ex vivo* cultures of hypothalamic explants over HH8-10 to investigate to what degree the molecular changes I report are intrinsic to the neuroepithelium. Principally, I find that there is a degree of neuroepithelial intrinsic regionalisation in both the anteroposterior and mediolateral axes. In conducting this work, I also develop an assay to investigate hypothalamic regionalisation through perturbations.

7.1 Characterising sub-stages of the HH10 chick embryo

In Chapter 3, I characterised a subtle staging problem in experiments: that the conventional Hamburger-Hamilton staging criteria for early chick embryos - number of somites - is not precise enough for early chick brain development. Sub-staging embryos to study hypothalamus development is novel, and doing so using deep neural networks makes use of modern, powerful techniques for image classification. This means that devising a more detailed and fine-grained staging system does not result in additional arduous pre-analysis from the experimental biologist.

Other attempts have been made to devise staging systems for developmental biology research that move beyond conventional staging metrics. Some authors have devised morphometric systems for staging, where some metric is used to stage the embryo. One advantage of my method is that all of the features that experimentalists in my lab have used to sub-stage the HH10 embryos do not have to be explicitly defined, but are instead encoded automatically through the neural network training process. One drawback of this is that an erroneous or irrelevant feature could be learned by the classifier, and here I mitigate this through saliency analyses, where I show that the classifier focuses on sub-stage specific features which were used during labelling.

This characterisation highlights that conventional staging studies may not be sufficient to fully understand hypothalamus development. My sub-staging method is one way in which more fine-grained time series and fate mapping experiments can be performed.

Advances in higher-resolution data collection methods (Cutrale *et al.*, 2019), including detailed time-courses of embryonic development by microscopy, necessitate careful

consideration of traditional staging guides. My studies underscore the importance of developing novel methods to finely gauge development in the early brain: I find that the number of somites is out of sync with early brain development. This has consequences for experiments on the development of early brain regions, including the hypothalamus, where accuracy may ultimately be key in deciphering the mechanisms leading to the emergence of distinct progenitor subtypes

Further work could expand the dimensions of the images used. I used 2-D morphological profiles to train my classifiers. Extending this with 3-D fluorescent images, which are increasingly used in developmental biology, could provide a more robust, accurate classifier. Additionally, including gene expression data for the brain classification could couple my sub-stages to a biological mechanism(s). Finally, the classifier could be extended for further use in the developing limb (Musy *et al.*, 2018), for example following my sub-staging approach, to provide a more fine-grained profile of limb development.

Additionally, future work should use the data presented in this thesis to fine-tune the labelling of the dataset. This could be done by using the wholemount ventral views, which are characterised in the context of both morphological and molecular profiles to fully characterise 10.1-3, with explicit links to biological events. Doing so will also minimise the risk of labelling errors.

7.2 Development of an image classifier to classify the HH10 sub-stages

Whilst I tested a large variety of different data augmentation, training, and construction regimes - this was not exhaustive. There are several additional steps which could be taken. For example, slightly expanding the dataset to accommodate a third (unaugmented) test set would be ideal as the final test of accuracy for the classifier.

Including as an additional preprocessing step an image feature extraction, such as the Haralick texture analysis (Haralick *et al.*, 1973), which have been used successfully to extract image features from MRI scans in biomedical imaging (Wibmer *et al.*, 2015) This would increase the interpretability of the PCA/k-means clustering, which I currently only use to justify my choice of sub-stage number.

In this work, my approach was to use biological domain expertise to inform a machine learning classifier to aid in experiments on HH10 chick embryos. By doing so, I combined the objective, systematic nature of machine learning approaches with biological domain expertise. This enabled training of high accuracy image classifiers on limited datasets, through bespoke data processing and augmentation regimes.

The key novelty of the study is the development of a strategy that enables classification of limited microscopy datasets covering subtle morphological changes in different experimental systems. I report a novel staging problem in early chick brain development, namely that the early brain undergoes subtle morphological changes over a very short time window, and that this phenomenon is uncoupled from somite number. This agrees with other studies on different developing tissues. For example, asynchronies have been reported in somite number and both mouse limb morphology (Musy *et al.*, 2018), and frog neural development (Sáenz-Ponce *et al.*, 2012). Therefore, I and others find that the number of somites is uncoupled from wider organ development at certain stages. Due to this uncoupling, traditional staging methods can fail, risking missing key developmental events and altering interpretation of experiments. My trained image classifier provides a solution to classify the developing brain (and hypothalamus) as it undergoes subtle morphological change.

Development is a continuous process, so a pragmatic consideration is how to categorise development into discrete tractable stages. The methodology used here provides an unbiased and systematic way of determining the number of classes to separate developmental staging data. In this instance, clustering of the brain dataset suggested three classes, but in other cases the class number may be more/less and my approach naturally extends to that.

Previous efforts to classify microscopy images in developmental biology have focused on hyperparameter optimisation (Pond *et al.*, 2021) without data augmentation. In contrast, I have instead focused on exploring different data augmentations, as I can fully exploit biological domain expertise when augmenting data, as opposed to hyperparameter optimisation. Recent theoretical work supports my approach, highlighting the superiority of data augmentation at optimising the learning of DCNNs (Hernández-García and König, 2018). I saw substantial differences in model performance with different data augmentations, indicating the importance of reasoned augmentation regime design. I also found that combining individually successful augmentations was an effective method to consolidate the benefits of these augmentations. To exemplify the utility of my approach, I then applied

similar data augmentation regimes to a developing limb dataset. Again, I made reasoned predictions about the dataset, for instance, that the model would overfit without flipping augmentations. I conclude that careful analysis of the data and an appropriate augmentation regime should be designed for specific datasets and problems encountered in developmental biology.

My work indicates that training using InceptionV3 and ResNet50 architectures is not always suitable for all classification problems, specifically on small datasets. This is unsurprising, as these models were built for ImageNet, a more general and larger dataset. Indeed, other work on biological image classification using small (albeit larger than ours) datasets has encountered issues using a ResNet50 architecture. Margapuri et al. tested various model architectures (including ResNet50) at classifying different bee species (Margapuri *et al.*, 2020). They found that ResNet50 overfits on their data, achieving at best a 7.4% accuracy. They also tested InceptionV3 finding similar results to ours, with a maximum accuracy of 44.5%. Whilst these authors did test augmentations including rotation and cutout, they found that the un-augmented data achieved higher accuracies. Considering these and my findings, it is clear that applying widely used image classification architectures alone is not a straightforward solution when dealing with small datasets.

My chosen approach, of training a DCNN to classify images, has advantages over more traditional classifiers that rely on precomputed features of the dataset. The latter either requires arduous manual selection and measurement of image features or computing image texture features. However, computing image texture features is reliant on registration of the dataset, which itself is not trivial particularly for developmental biology datasets.

In contrast, my approach requires no prior knowledge about the embryos, nor the skill to assess the morphological features. My approach also shows that pre-selected features may not be those that are the most useful for classification. For instance, I find that the best classifier of the 10.3 brain sub-stage is neuromere shape (not one of the pre-selected features), while for the limb, morphology was a stronger classifying feature than *SHH* expression, even in cases where *SHH* was expressed in control and not in the treated limb. My strategy would also allow image classifiers to be trained for other biological problems with limited microscopy data. Finally, using my DCNN is straightforward for the end user, an important factor when considering the time critical nature of biological experiments.

Finally, I used saliency maps to gain insight into the regions of the images to which the classifiers were most sensitive. My results illustrate the utility of saliency analysis in

interpreting classifiers in a manner that is coherent to experimental biologists. This has been exemplified in other areas at the interface of DL and biomedical research e.g. X-ray images of lung cancer and infection labelled by radiologists (Baltruschat *et al.*, 2019; Panwar *et al.*, 2020). Here, the authors leveraged saliency methods to understand classifier decision making, an important step if DNN based classifiers are to have a role in medical decision making. The use of such methods will encourage confidence in non-specialists about DCNN-based classifiers. As I show here, there is potential for insight into the most predictive features of labelled classes, free from human preconceptions. Therefore, these analyses encourage confidence in the classifier, which will increase uptake by the wider developmental biology field.

7.3 Characterisation of early hypothalamus morphology in 3-D at HH10

In Chapter 4, I defined and characterised a novel morphology in the developing hypothalamus at HH8-14. This study is important because previous work has only mentioned the neuroepithelial morphology in passing (Fu *et al.*, 2017). I generated a detailed visualisation of morphology over HH8-14, which are the stages where hypothalamic induction and regionalisation are occurring (Fu *et al.*, 2017; Kim *et al.*, 2022). Further work here could refine the morphometric study through a user-generated ground truth. Currently, the U-net which I used to classify cell membranes in Section 4.2.2 was packaged pre-trained on a confocal dataset of cell membranes in plant tissue. Generating a more expansive hypothalamic membrane dataset, and training the U-net on manually segmented hypothalamic cell membranes, would enhance the segmentation. Further, an extended time series of morphology between HH14 (the latest I visualised) and E5 embryo, where the hypothalamus has developed the protruding morphology (Fu *et al.*, 2017) would be useful.

7.4 Investigation of early hypothalamic regionalisation and correlations with developing morphology

Building on the work in Chapter 4, In Chapter 5, I focused on visualising genes involved in early hypothalamic regionalisation, using ventral views of wholemount neuroepithelia which I had isolated from the surrounding tissues.

Previous efforts have usually investigated the development of the hypothalamus using primarily un-dissected wholemounts and sections. Whilst there has been some previous examination of the dissected neuroepithelium (Dale *et al.*, 1999), I have shown in this Chapter a novel approach to analysing hypothalamic morphology and morphogenesis by extension into 3-D. The principal advantage of using the wholemount ventral views is they reveal the mediolateral shapes and extents of nascent hypothalamic regions, as well as how these relates to anteroposterior regionalisation and morphology (i.e. the A-fold/V-face).

Future work should seek to exploit the advantages of each modality of visualising the developing hypothalamus, and by doing so ameliorate the disadvantages of each method. For example, wholemount and sagittal sections naturally complement each other as sagittal sections can verify wholemount views, which are more susceptible to artefacts as a result of perspective shifts.

A particularly surprising feature I noticed of early hypothalamus development was that my wholemount ventral views showed there was a high degree of heterogeneity and dynamism in *SHH*, *BMP2*, and *PTCH1* expression. In each, my data showed an extension on the current understanding. For *SHH*, I showed that the expression profile of *SHH* was not a simple radial disc, but in fact had distinct points of strong/weak expression in the A-fold and lateral to the A-fold respectively. In contrast to the findings of Fu et al., (2017) I found *FGF10* and *SHH* appeared to be expressed to be in complementary gradients at HH10, *FGF10* running from anterior to posterior and *SHH* vice versa.

This strong expression in the A-fold coincided with where *SHH* and *FGF10* overlapped, which may have important implications for the subsequent specification, migration, and growth of the hypothalamus. Similarly, the weak expression of *SHH* coincided with the eventual location of *BMP2* at HH11-14, where *BMP2* was confined lateral to A-base.

Previous work has shown that *BMP2* can downregulate *SHH* expression in the developing hypothalamus, but through a Tbx2 related mechanism. There is no evidence that *Tbx2* is expressed in the *BMP2* positive cells immediately lateral to the A-fold, so open questions here are i) is *BMP2* downregulating *SHH* here and ii) if so, through what mechanism?

Making thorough use of the single cell RNA sequencing dataset provided by (Kim *et al.*, 2022) may elicit potential target factors which could explain this.

More anteriorly, I showed that there was an early regionalisation of *SHH*/*BMP2* as the A-fold and V-face become apparent at HH9. *BMP2* begins to be expressed in a heart-shaped ring, overlapping with outermost *SHH*-expressing cells. Triple-labelling of *SHH*, *BMP2* and *PTCH1* show *BMP2* medial to *PTCH1*-domains. In the apex of the heart-shaped ring - a region that marks/predicts the posterior V-face - *BMP2* is transiently expressed at high levels, before being downregulated here. What mediates this is unclear. The area this is occurring in, the V-face neuroepithelium, is in register (i.e. aligned on the antero-posterior axis) with the prechordal mesoderm, and a potential candidate for this mediation is the release of factors from the prechordal mesoderm, as shortly after, the registration between the neuroepithelium and prechordal mesoderm is lost as the prechordal mesoderm becomes relatively more posterior (Fu *et al.*, 2019). However, a more detailed characterisation of prechordal mesoderm-neuroepithelial signalling is required before a specific mechanism can be hypothesised.

Therefore, in Chapters 4-5 I was able to characterise highly dynamic expression patterns of genes marking early hypothalamic regionalisation, and relate this to the A-fold and V-face over HH8-14.

This has important implications for hypothalamus development. If the earliest detectable regionalisations prefigure the development of morphology then a more complete understanding of hypothalamic regionalisation and development must take into account this morphogenetic process. A related question is whether these morphological structures are the earliest detectable indications of the distinctive adult morphology of the hypothalamus. This morphology can be characterised as having three attributes: (i) the organisation of adult neuronal populations doro-ventrally - does this reflect differences in the planar organisation at early time points? (ii) Following this, does the A-base/V-face mark the most ventral point, and the future location of the infundibulum? (iii) Does this morphogenesis occurring between HH9-14 reflect that much of the hypothalamus protrudes ventrally from the rest of the forebrain, as indeed it does by HH14?

To test these hypotheses, further work should seek to perturb the formation of the A-fold, in the first instance by manipulating SHH/FGF10 signalling. As the A-fold is consistently located where SHH and FGF10 overlap, this could reveal how the anteroposterior location of the A-fold is determined. Similarly, knockdown of BMP2 could provide clues as to whether

the lateral (to the A-fold) downregulation of SHH reflects a mediolateral size constraint on the developing morphology.

7.5 An *ex vivo* assay to assess neuroepithelial regionalisation in the early developing hypothalamus

In Chapter 6, I built on previous work that used hypothalamic explants to investigate molecular regionalisation in hypothalamus development (Manning *et al.*, 2006; Kim *et al.*, 2022). I presented two novel findings. First, that the explants retain their anterior/posterior axis as measured by *PTCH1* regionalising with DiI which labelled the initial anterior of the explant after culture. This could be expanded on by using DiI and DiO simultaneously on the initial lateral limits of the explants, to assess whether there is retention of the mediolateral axis.

In this way, my work represents a basis for assessing how much of the developing hypothalamus regionalisation is intrinsic to events in the neuroepithelium, as the prechordal mesoderm was removed prior to culture. The regionalisation of the hypothalamus being (at least semi-) intrinsic is important as it narrows down the potential mechanisms. Further work here should investigate potential mechanisms by perturbing the markers of regionalisation (e.g. *SHH* and *PTCH1*) through small molecule inhibitors such as Cyclopamine (Stanton and Peng, 2010).

A surprising result from the *ex vivo* studies presented in Chapter 6 was that *SHH* expression frequently organised into a ‘Y’ pattern. This pattern of expression is reminiscent of the pattern seen *in vivo* (in the A-fold) from HH10 onwards (Chapter 5, Fig 5.2). As these *SHH* expressing cells appear to mark the posterior tuberal hypothalamus, the recurrence of this pattern *ex vivo* implies that the onset of posterior tuberal hypothalamus identity may be neuroepithelial intrinsic. A substantial advantage of conducting simultaneous *in vivo* and *ex vivo* studies is through comparison between the two.

Not only do the explant cultures indicate to what extent regionalisation is neuroepithelial intrinsic, they also can provide clues to underlying mechanisms of development through virtue of removal. For example, my results show that explants cultured at HH6 for 72 hours show both anteroposterior axis retention (i.e. *PTCH1* expression anteriorly) and also, that

potentially the posterior-tuberal progenitor cells posterior to this self-organise (i.e. the Y-shaped *SHH* profile).

In vivo, the anterior *PTCH1* positive, *SHH* negative cells appear to prefigure the anterior hypothalamus/ anterior limit of the hypothalamus (Fig 5.2) Posterior to these cells, are the anterior tuberal progenitors, which express *FGF10* but not *SHH*. Whilst the *FGF10* probes did not work satisfactorily in my *ex vivo* studies, whereas I observe that *ex vivo,* the anterior *PTCH1* expressing cells usually abut the posterior Y-shaped *SHH* expression.

Therefore I would have expected that if tuberal progenitors were retaining every aspect of *in vivo* behaviour there would be a *SHH, PTCH1* negative population of cells anterior to the Y-shaped *SHH* profile. The consistent lack of this, in both the HH6 and HH8 explants, could indicate that the continued generation of anterior tuberal progenitors (which are *FGF10* positive, *SHH* negative), require ongoing signalling from the prechordal mesoderm for some time after HH8.

7.6 A role for mathematical modelling

Mathematical modelling has played a useful role in deciphering the contribution of SHH and other signalling molecules in the neural tube (Balaskas *et al.*, 2012). Here, the authors describe the temporal dynamics of expression of three neural tube genes downstream of Shh signalling (Pax6, Olig2, Nkx2.2). Further, Cohen et al. revealed how quantitative modelling of SHH activity in the neural tube allowed for increased understanding of a switch-like role for SHH, providing evidence for how graded morphogen signals can produce sharp and distinct outputs in developing tissues (Cohen *et al.*, 2014; Groves *et al.*, 2020).

Other work has used mathematical modelling to investigate SHH patterning/molecular interactions in complex spatial domains. For example, Menshykau et al. investigated lung branching morphogenesis using simulations of FGF10 and SHH, solving their equations on 2-D spatial domains that resembled lung branches (Menshykau *et al.*, 2012). In doing so, they could also investigate the impact that lung-like morphology has on the regulatory network between FGF10 and SHH.

The data I have acquired in this thesis have led me to the point where mathematical modelling will be instrumental in further unpicking the complex regionalisation of SHH (and

FGF10/BMPs) in the developing hypothalamus that I investigated in Chapter 5. Such modelling could also aid understanding the relative contribution and feedback of this regionalisation on the developing morphology I described in Chapter 4. In addition, the development of a more fine-grained classifier will allow me to more closely match mathematical models to experimental data. Finally, the *ex vivo* work provides a complementary experimental method to modelling, as it will allow us to unpick the relative contributions of the prechordal mesoderm and neuroepithelium in ongoing hypothalamic regionalisation/growth.

In summary, the work presented in this thesis encompasses a range of different experimental and computational approaches and includes the study of patterning and morphogenesis events in the developing hypothalamus. I have provided novel insights into early hypothalamic morphogenesis and molecular regionalisation. The challenge in any future work is to continue to disentangle these complex processes through further experimentation, image analysis, and mathematical modelling.

Appendix

	Repeat											
	1	**2**	**3**	**4**	**5**	**6**	**7**	**8**	**9**	**10**	**Avg.**	**SD**
RFC	**54.8**	25.8	35.5	25.9	32.3	41.9	35.5	29.0	38.7	45.2	36.5	9.1
SVM	22.6	**41.9**	32.3	29.0	22.6	38.7	35.5	22.6	32.3	35.5	31.3	**7.0**
KNN	41.9	38.7	**51.2**	45.2	41.9	32.3	38.7	29.0	22.6	41.9	**38.3**	8.3

Appendix Table 1 Traditional machine learning classification on the un-augmented dataset. The original dataset was used to fit ten classifiers, and the classification accuracies were determined with a different (80:20) split of training/ testing data for each model. RFC; Random forest classifier. SVM; support vector machine, KNN; k-nearest neighbours (k = 3). Highest classification accuracies for each repeat, highest average for each classifier (Avg.), and lowest standard deviation (SD) are shown in bold.

Aug	Fold											
	1	**2**	**3**	**4**	**5**	**6**	**7**	**8**	**9**	**10**	**Avg.**	**SD**
1	40.7	41.5	43.3	46.7	42.4	46.1	47.0	46.7	46.5	40.4	44.1	**2.7**
1 + 2	**41.0**	40.0	53.3	49.1	**44.9**	38.1	46.8	46.9	47.5	39.4	44.7	4.9
1 + 3	35.6	**50.7**	51.3	**49.6**	43.3	47.6	46.2	**47.1**	32.9	**49.1**	45.3	6.3
1 + 4	40.0	35.4	54.4	40.9	40.9	46.6	46.7	46.7	**48.7**	42.6	44.3	5.4
1 + 5	40.1	41.9	53.8	45.4	36.2	47.5	46.7	46.7	46.8	40.1	44.5	5.0
1 + 2,4,5 RC	38.0	42.2	**60.5**	38.7	40.9	**52.8**	**48.6**	46.0	47.1	37.8	**45.4**	7.4
Fold Avg.	39.2	42.0	52.8	45.1	41.4	46.5	47.0	46.7	45.1	41.6		

Appendix Table 2 Augmentation exploration of the dataset using InceptionV3. I explored the data-space using *k*-fold cross validation, the individual fold validation accuracies that each network achieved are shown in columns 1-10, and the averages and standard deviation of these accuracies is shown in the rightmost columns. As a baseline processing step, all images were rotated 15 times, at equally spaced degrees. I then tested augmentations on top of this baseline, before a final test whereby each image was randomly augmented. Augmentations (Aug) as follows: (1) rotation (baseline); (2) shear; (3) crop; (4) Gaussian blur; (5) cutout; (RC) random combination of rotation + cutout, or shear, or blur. Highest validation accuracies for each fold, highest average for each augmentation (Avg.), and lowest standard deviation (SD) are shown in bold.

Aug	Fold											
	1	**2**	**3**	**4**	**5**	**6**	**7**	**8**	**9**	**10**	**Avg.**	**SD**
1	40.0	71.1	73.5	54.1	69.4	66.9	64.1	70.9	65.9	63.7	64.0	10.0
1 + 2	65.4	40.1	67.0	51.0	69.8	67.1	63.4	48.7	67.9	56.2	59.9	11.7
1 + 3	44.2	55.6	60.9	52.4	51.8	46.7	46.7	50.0	45.8	46.9	50.1	**5.2**
1 + 4	**69.0**	**74.5**	**75.9**	51.1	**70.6**	69.2	**70.6**	70.1	**71.6**	**69.4**	**69.2**	6.8
1 + 5	45.7	40.1	56.9	52.0	44.3	**70.4**	69.8	49.9	71.3	48.2	54.9	11.7
1 + 2,4,5 RC	63.1	37.2	68.7	48.1	67.3	62.7	52.0	**71.0**	68.4	55.3	59.4	11.0
Fold Avg.	54.6	53.1	67.2	51.5	62.2	63.8	61.1	60.1	65.2	56.6		

Appendix Table 3 Augmentation exploration of the dataset using ResNet50. I explored the data-space using *k*-fold cross validation, the individual fold validation accuracies that each network achieved are shown in columns 1-10, and the averages and standard deviation of these accuracies is shown in the rightmost columns. As a baseline processing step, all images were rotated 15 times, at equally spaced degrees. I then tested augmentations on top of this baseline, before a final test whereby each image was randomly augmented (see **Table 3.1** caption).

Aug	Avg. (%)	SD	Min (%)	Max (%)
Rotation	80.3	6.7	64.7	**91.6**
Crop	74.8	8.4	59.9	82.3
Shear	78.4	4.8	68.1	84.8
Gaussian blur	80.3	4.9	71.9	89.3
Cutout	**83.6**	**4.6**	**76.1**	91.5
Crop	53.5	8.9	39.2	74.9

Appendix Table 4 Data augmentation regime exploration with hold-out cross-validation. The networks were initialised and trained with reshuffled data 10 times for each augmentation. Rotation achieves the highest accuracy at 91.6%, however cutout reaches 91.5%, and is the most reliable, with the highest average and lowest standard deviation. The optimal score for each metric is shown in bold.

Aug	Fold											
	1	**2**	**3**	**4**	**5**	**6**	**7**	**8**	**9**	**10**	**Avg.**	**SD**
1 + Möbius	55.7	57.6	47.4	49.1	49.4	41.3	38.1	57.4	43.9	66.1	50.6	8.6
1 + M:G (10% chance)	76.6	79.4	67.4	66.4	79.8	76.9	70.8	77.6	84.6	79.0	75.9	5.8

Appendix Table 5 Testing of Möbius transformations as data augmentations for the brain dataset. 1 + Möbius: the dataset is augmented with the baseline & Möbius transformations. 1 + M:G (10% chance). The dataset is augmented with Gaussian blur with a 10% chance of a Möbius transformation per image.

Hyperparameter	Value/category
Activation function	ReLU
Batch size	32
Layer dropout	20%
Final layer dropout	50%
L_2 regularisation λ	10^{-4}
Optimiser	Adam
Learning rate	10^{-4}
Average validation accuracy	64.1%
Min, Max validation accuracy	43.6%, 81.5%

Appendix Table 6 Optimal hyperparameters for the baseline, determined by Bayesian optimisation. I tested these hyperparameters with the following ranges: Activation function: ReLU-Sigmoid, Batch size: 16-128, Optimiser: Adam, Adadelta, Adamax, Adagrad, SGD, RMSprop, Layer dropout: 0.05-0.25%. Final layer dropout: 0.3-0.8%. λ: 10^{-3} - 10^{-6}, Learning rate: 10^{-1} - 10^{-6}, selecting the value/category which was used most by the optimisation algorithm.

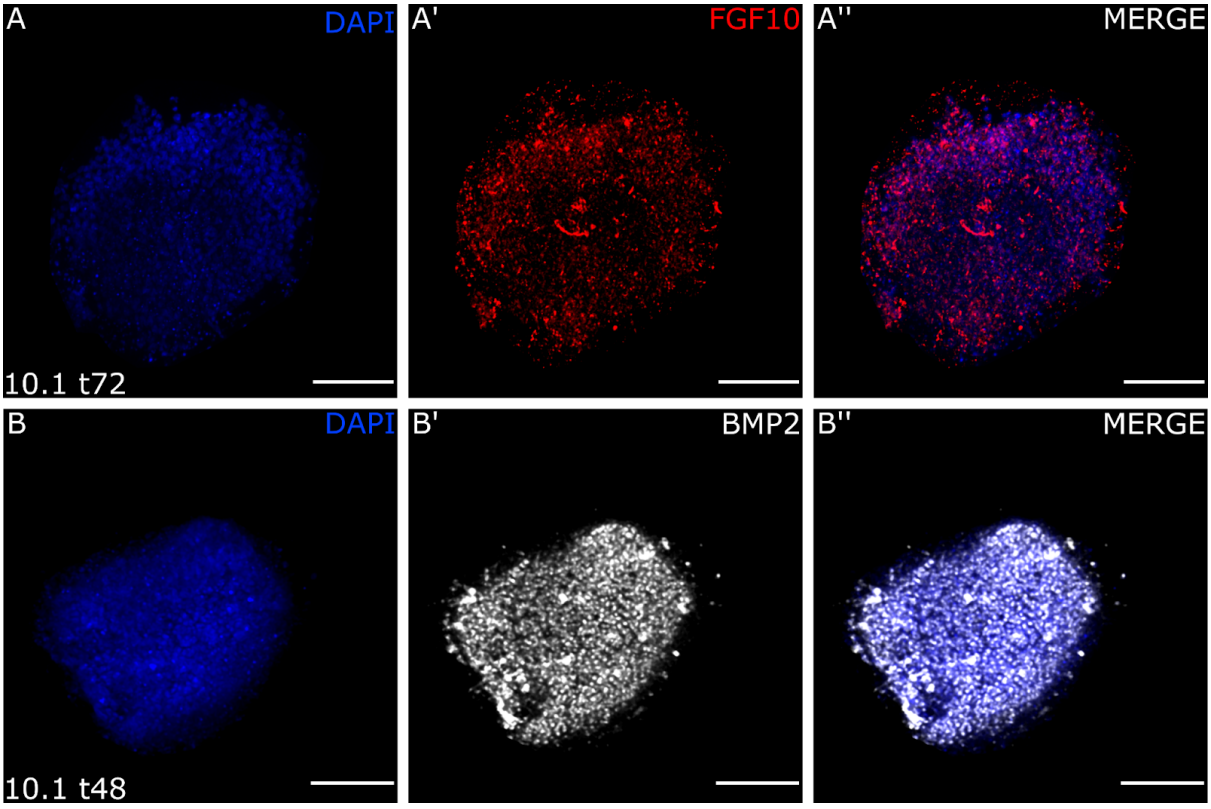

Appendix Figure 1 HCR *in situ* hybridisation for *FGF10* and *BMP2 ex vivo* results in a low signal to noise ratio. (A-A'') In a 10.1 explant cultured for 72h, *FGF10* signal (A') is non-specific and noisy. (B-B'') In a 10.1 explant cultured for 48h, BMP2 signal is also noisy, with non-specific signal. Scale bars 100μm.

References

1. **Abadi, M., Agarwal, A., Barham, P., Brevdo, E., Chen, Z., Citro, C., Corrado, G.S., Davis, A., Dean, J., Devin, M., Ghemawat, S., Goodfellow, I., Harp, A., Irving, G., Isard, M., Jia, Y., Jozefowicz, R., Kaiser, L., Kudlur, M., Levenberg, J., Mané, D., Monga, R., Moore, S., Murray, D., Olah, C., Schuster, M., Shlens, J., Steiner, B., Sutskever, I., Talwar, K., Tucker, P., Vanhoucke, V., Vasudevan, V., Viégas, F., Vinyals, O., Warden, P., Wattenberg, M., Wicke, M., Yu, Y. and Zheng, X.** (2015) 'TensorFlow: Large-Scale Machine Learning on Heterogeneous Systems'. Available at: https://www.tensorflow.org/.

2. **Adolphe, C., Junker, J.P., Lyubimova, A., Oudenaarden, A. van and Wainwright, B.** (2017) 'Patched Receptors Sense, Interpret, and Establish an Epidermal Hedgehog Signaling Gradient', *Journal of Investigative Dermatology*, 137(1), pp. 179–186. Available at: https://doi.org/10.1016/j.jid.2016.06.632.

3. **Agarap, A.F.** (2018) 'Deep learning using rectified linear units (ReLU)', *arXiv preprint arXiv:1803.08375* [Preprint].

4. **Álvarez-Buylla, A. and Ihrie, R.A.** (2014) 'Sonic hedgehog signaling in the postnatal brain', *Seminars in Cell & Developmental Biology*, 33, pp. 105–111. Available at: https://doi.org/10.1016/j.semcdb.2014.05.008.

5. Autodesk (2022) 'Autodesk Meshmixer. 3D visualization software for working with triangle meshes.' Available at: https://www.meshmixer.com

6. **Bai, C.B., Auerbach, W., Lee, J.S., Stephen, D. and Joyner, A.L.** (2002) 'Gli2, but not Gli1, is required for initial Shh signaling and ectopic activation of the Shh pathway', *Development (Cambridge, England)*, 129(20), pp. 4753–4761. Available at: https://doi.org/10.1242/dev.129.20.4753.

7. **Bailoni, A., Pape, C., Hütsch, N., Wolf, S., Beier, T., Kreshuk, A. and Hamprecht, F.A.** (2019) 'GASP, a generalized framework for agglomerative clustering of signed graphs and its application to Instance Segmentation'. arXiv. Available at: http://arxiv.org/abs/1906.11713 (Accessed: 7 July 2022).

8. **Balaskas, N., Ribeiro, A., Panovska, J., Dessaud, E., Sasai, N., Page, K.M., Briscoe, J. and Ribes, V.** (2012) 'Gene regulatory logic for reading the Sonic Hedgehog signaling gradient in the vertebrate neural tube', *Cell*, 148(1–2), pp. 273–284. Available at: https://doi.org/10.1016/j.cell.2011.10.047.

9. **Baltruschat, I.M., Nickisch, H., Grass, M., Knopp, T. and Saalbach, A.** (2019) 'Comparison of deep learning approaches for multi-label chest X-ray classification', *Scientific reports*, 9(1), pp. 1–10.

10. **Bedont, J.L., Newman, E.A. and Blackshaw, S.** (2015) 'Patterning, specification, and differentiation in the developing hypothalamus', *WIREs Developmental Biology*, 4(5), pp. 445–468. Available at: https://doi.org/10.1002/wdev.187.

11. **Bellusci, S., Grindley, J., Emoto, H., Itoh, N. and Hogan, B.L.** (1997) 'Fibroblast growth factor 10 (FGF10) and branching morphogenesis in the embryonic mouse lung', *Development*, 124(23), pp. 4867–4878. Available at: https://doi.org/10.1242/dev.124.23.4867.

12. **Ben-Hur, A. and Guyon, I.** (2003) 'Detecting Stable Clusters Using Principal Component Analysis', in M.J. Brownstein and A.B. Khodursky (eds) *Functional*

Genomics: Methods and Protocols. Totowa, NJ: Humana Press (Methods in Molecular Biology), pp. 159–182. Available at: https://doi.org/10.1385/1-59259-364-X:159.

13. **Bergstra, J. and Bengio, Y.** (2012) 'Random search for hyper-parameter optimization.', *J. Mach. Learn. Res.*, 13(2).

14. **Bhardwaj, G., Murdoch, B., Wu, D., Baker, D.P., Williams, K.P., Chadwick, K., Ling, L.E., Karanu, F.N. and Bhatia, M.** (2001) 'Sonic hedgehog induces the proliferation of primitive human hematopoietic cells via BMP regulation', *Nature Immunology*, 2(2), pp. 172–180. Available at: https://doi.org/10.1038/84282.

15. **Bholowalia, P. and Kumar, A.** (2014) 'EBK-means: A clustering technique based on elbow method and k-means in WSN', *Int. J. Comput. Appl.*, 105(9).

16. **Biran, J., Tahor, M., Wircer, E. and Levkowitz, G.** (2015) 'Role of developmental factors in hypothalamic function', *Front. Neuroanat.*, 9, p. 47. Available at: https://doi.org/10.3389/fnana.2015.00047.

17. **Boehm, B., Rautschka, M., Quintana, L., Raspopovic, J., Jan, Ž. and Sharpe, J.** (2011) 'A landmark-free morphometric staging system for the mouse limb bud', *Development*, 138, pp. 1227–1234. Available at: https://doi.org/10.1242/dev.057547.

18. **Bradski, G.** (2000) 'The OpenCV Library', *Dr. Dobb's Journal of Software Tools*. Available at: https://github.com/opencv/opencv

19. **Breiman, L.** (2001) 'Random Forests', *Machine Learning*, 45(1), pp. 5–32. Available at: https://doi.org/10.1023/A:1010933404324.

20. **Briscoe, J. and Small, S.** (2015) 'Morphogen rules: design principles of gradient-mediated embryo patterning', *Development*, 142(23), pp. 3996–4009. Available at: https://doi.org/10.1242/dev.129452.

21. **Briscoe, J. and Thérond, P.P.** (2013) 'The mechanisms of Hedgehog signalling and its roles in development and disease', *Nature Reviews. Molecular Cell Biology*, 14(7), pp. 416–429. Available at: https://doi.org/10.1038/nrm3598.

22. **Cadart, C., Zlotek-Zlotkiewicz, E., Le Berre, M., Piel, M. and Matthews, H.K.** (2014) 'Exploring the function of cell shape and size during mitosis', *Developmental Cell*, 29(2), pp. 159–169. Available at: https://doi.org/10.1016/j.devcel.2014.04.009.

23. **Caicedo, J.C., Roth, J., Goodman, A., Becker, T., Karhohs, K.W., Broisin, M., Molnar, C., McQuin, C., Singh, S., Theis, F.J. and Carpenter, A.E.** (2019) 'Evaluation of Deep Learning Strategies for Nucleus Segmentation in Fluorescence Images', *Cytometry Part A*, 95(9), pp. 952–965. Available at: https://doi.org/10.1002/cyto.a.23863.

24. **Carballo, G.B., Honorato, J.R., de Lopes, G.P.F. and Spohr, T.C.L. de S. e** (2018) 'A highlight on Sonic hedgehog pathway', *Cell Communication and Signaling*, 16(1), p. 11. Available at: https://doi.org/10.1186/s12964-018-0220-7.

25. **Carreno, G., Apps, J.R., Lodge, E.J., Panousopoulos, L., Haston, S., Gonzalez-Meljem, J.M., Hahn, H., Andoniadou, C.L. and Martinez-Barbera, J.P.** (2017) 'Hypothalamic sonic hedgehog is required for cell specification and proliferation of LHX3/LHX4 pituitary embryonic precursors', *Development (Cambridge, England)*, 144(18), pp. 3289–3302. Available at: https://doi.org/10.1242/dev.153387.

26. **Cayuso, J., Ulloa, F., Cox, B., Briscoe, J. and Martí, E.** (2006) 'The Sonic hedgehog pathway independently controls the patterning, proliferation and survival of neuroepithelial cells by regulating Gli activity', *Development (Cambridge, England)*, 133(3), pp. 517–528. Available at: https://doi.org/10.1242/dev.02228.

27. **Chang, D.T., López, A., von Kessler, D.P., Chiang, C., Simandl, B.K., Zhao, R., Seldin, M.F., Fallon, J.F. and Beachy, P.A.** (1994) 'Products, genetic linkage and limb patterning activity of a murine hedgehog gene', *Development (Cambridge, England)*, 120(11), pp. 3339–3353. Available at: https://doi.org/10.1242/dev.120.11.3339.

28. **Chawla, N.V., Bowyer, K.W., Hall, L.O. and Kegelmeyer, W.P.** (2002) 'SMOTE: Synthetic Minority Over-sampling Technique', *Journal of Artificial Intelligence Research*, 16, pp. 321–357. Available at: https://doi.org/10.1613/jair.953.

29. **Chiang, C., Litingtung, Y., Lee, E., Young, K.E., Corden, J.L., Westphal, H. and Beachy, P.A.** (1996) 'Cyclopia and defective axial patterning in mice lacking Sonic hedgehog gene function', *Nature*, 383(6599), pp. 407–413. Available at: https://doi.org/10.1038/383407a0.

30. **Chinnaiya, K., Tickle, C. and Towers, M.** (2014) 'Sonic hedgehog-expressing cells in the developing limb measure time by an intrinsic cell cycle clock', *Nature Communications*, 5(1), p. 4230. Available at: https://doi.org/10.1038/ncomms5230.

31. **Choi, H.M.T., Schwarzkopf, M., Fornace, M.E., Acharya, A., Artavanis, G., Stegmaier, J., Cunha, A. and Pierce, N.A.** (2018) 'Third-generation in situ hybridization chain reaction: multiplexed, quantitative, sensitive, versatile, robust', *Development (Cambridge, England)*, 145(12), p. dev165753. Available at: https://doi.org/10.1242/dev.165753.

32. **Chollet, F. and others** (2015) 'Keras'. Available at: https://keras.io.

33. **Cignoni, P., Callieri, M., Corsini, M., Dellepiane, M., Ganovelli, F. and Ranzuglia, G.** (2008) 'MeshLab: an Open-Source Mesh Processing Tool', p. 8. Eurographics Italian Chapter Conference, The Eurographics Association. doi.org/10.2312/LocalChapterEvents/ItalChap/ItalianChapConf2008/129-136

34. **Clark, A.** (2015) 'Pillow (PIL Fork) Documentation'. readthedocs. Available at: https://buildmedia.readthedocs.org/media/pdf/pillow/latest/pillow.pdf.

35. **Cohen, M., Page, K.M., Perez-Carrasco, R., Barnes, C.P. and Briscoe, J.** (2014) 'A theoretical framework for the regulation of Shh morphogen-controlled gene expression', *Development (Cambridge, England)*, 141(20), pp. 3868–3878. Available at: https://doi.org/10.1242/dev.112573.

36. **Collinet, C. and Lecuit, T.** (2021) 'Programmed and self-organized flow of information during morphogenesis', *Nature Reviews Molecular Cell Biology*, 22(4), pp. 245–265. Available at: https://doi.org/10.1038/s41580-020-00318-6.

37. **Crick, F.** (1970) 'Diffusion in embryogenesis', *Nature*, 225(5231), pp. 420–422. Available at: https://doi.org/10.1038/225420a0.

38. **Cutrale, F., Fraser, S.E. and Trinh, L.A.** (2019) 'Imaging, visualization, and computation in developmental biology', *Annual Review of Biomedical Data Science*, 2, pp. 223–251.

39. **Dahmane, N. and Ruiz i Altaba, A.** (1999) 'Sonic hedgehog regulates the growth

and patterning of the cerebellum', *Development (Cambridge, England)*, 126(14), pp. 3089–3100. Available at: https://doi.org/10.1242/dev.126.14.3089.

40. **Dale, J.K., Vesque, C., Lints, T.J., Sampath, T.K., Furley, A., Dodd, J. and Placzek, M.** (1997) 'Cooperation of BMP7 and SHH in the Induction of Forebrain Ventral Midline Cells by Prechordal Mesoderm', *Cell*, 90(2), pp. 257–269. Available at: https://doi.org/10.1016/S0092-8674(00)80334-7.

41. **Dale, K., Sattar, N., Heemskerk, J., Clarke, J.D., Placzek, M. and Dodd, J.** (1999) 'Differential patterning of ventral midline cells by axial mesoderm is regulated by BMP7 and chordin', *Development*, 126(2), pp. 397–408. Available at: https://doi.org/10.1242/dev.126.2.397.

42. **Dessaud, E., McMahon, A.P. and Briscoe, J.** (2008) 'Pattern formation in the vertebrate neural tube: a sonic hedgehog morphogen-regulated transcriptional network', *Development*, 135(15), pp. 2489–2503. Available at: https://doi.org/10.1242/dev.009324.

43. **DeVries, T. and Taylor, G.W.** (2017) 'Improved regularization of convolutional neural networks with cutout', *arXiv preprint arXiv:1708.04552*, pp. 1–8.

44. **Donovan, S.L. and Dyer, M.A.** (2005) 'Regulation of proliferation during central nervous system development', *Seminars in Cell & Developmental Biology*, 16(3), pp. 407–421. Available at: https://doi.org/10.1016/j.semcdb.2005.02.012.

45. **Dubourg, C., Lazaro, L., Pasquier, L., Bendavid, C., Blayau, M., Le Duff, F., Durou, M.-R., Odent, S. and David, V.** (2004) 'Molecular screening of SHH, ZIC2, SIX3, and TGIF genes in patients with features of holoprosencephaly spectrum: Mutation review and genotype-phenotype correlations', *Human Mutation*, 24(1), pp. 43–51. Available at: https://doi.org/10.1002/humu.20056.

46. **Eachus, H., Bright, C., Cunliffe, V.T., Placzek, M., Wood, J.D. and Watt, P.J.** (2017) 'Disrupted-in-Schizophrenia-1 is essential for normal hypothalamic-pituitary-interrenal (HPI) axis function', *Human Molecular Genetics*, 26(11), pp. 1992–2005. Available at: https://doi.org/10.1093/hmg/ddx076.

47. **Echelard, Y., Epstein, D.J., St-Jacques, B., Shen, L., Mohler, J., McMahon, J.A. and McMahon, A.P.** (1993) 'Sonic hedgehog, a member of a family of putative signaling molecules, is implicated in the regulation of CNS polarity', *Cell*, 75(7), pp. 1417–1430. Available at: https://doi.org/10.1016/0092-8674(93)90627-3.

48. **Ellis, P.S., Burbridge, S., Soubes, S., Ohyama, K., Ben-Haim, N., Chen, C., Dale, K., Shen, M.M., Constam, D. and Placzek, M.** (2015) 'ProNodal acts via FGFR3 to govern duration of Shh expression in the prechordal mesoderm', *Development (Cambridge, England)*, 142(22), pp. 3821–3832. Available at: https://doi.org/10.1242/dev.119628.

49. **Ericson, J., Morton, S., Kawakami, A., Roelink, H. and Jessell, T.M.** (1996) 'Two critical periods of Sonic Hedgehog signaling required for the specification of motor neuron identity', *Cell*, 87(4), pp. 661–673. Available at: https://doi.org/10.1016/s0092-8674(00)81386-0.

50. **Ericson, J., Muhr, J., Placzek, M., Lints, T., Jessell, T.M. and Edlund, T.** (1995) 'Sonic hedgehog induces the differentiation of ventral forebrain neurons: a common signal for ventral patterning within the neural tube', *Cell*, 81(5), pp. 747–756. Available at: https://doi.org/10.1016/0092-8674(95)90536-7.

51. **Eulenberg, P., Köhler, N., Blasi, T., Filby, A., Carpenter, A.E., Rees, P., Theis, F.J. and Wolf, F.A.** (2017) 'Reconstructing cell cycle and disease progression using deep learning', *Nat. Commun.*, 8(1), pp. 1–6.

52. **Fainsod, A., Deißler, K., Yelin, R., Marom, K., Epstein, M., Pillemer, G., Steinbeisser, H. and Blum, M.** (1997) 'The dorsalizing and neural inducing gene follistatin is an antagonist of BMP-4', *Mechanisms of Development*, 63(1), pp. 39–50. Available at: https://doi.org/10.1016/S0925-4773(97)00673-4.

53. **Fan, C.M. and Tessier-Lavigne, M.** (1994) 'Patterning of mammalian somites by surface ectoderm and notochord: evidence for sclerotome induction by a hedgehog homolog', *Cell*, 79(7), pp. 1175–1186. Available at: https://doi.org/10.1016/0092-8674(94)90009-4.

54. **Fu, T., Pearson, C., Towers, M. and Placzek, M**. (2019) 'Development of the basal hypothalamus through anisotropic growth', *J. Neuroendocrinol.*, 31, p. e12727. Available at: https://doi.org/10.1111/jne.12727.

55. **Fu, T., Towers, M. and Placzek, M.A.** (2017) 'Fgf10+ progenitors give rise to the chick hypothalamus by rostral and caudal growth and differentiation', *Development*, 144, pp. 3278–88. Available at: https://doi.org/10.1242/dev.153379.

56. **Fuccillo, M., Joyner, A.L. and Fishell, G.** (2006) 'Morphogen to mitogen: the multiple roles of hedgehog signalling in vertebrate neural development', *Nature Reviews. Neuroscience*, 7(10), pp. 772–783. Available at: https://doi.org/10.1038/nrn1990.

57. **Fushiki, T.** (2011) 'Estimation of prediction error by using K-fold cross-validation', *Stat. Comput.*, 21(2), pp. 137–146. Available at: https://doi.org/10.1007/s11222-009-9153-8.

58. **Gabas, A., Corona, E., Alenyà, G. and Torras, C.** (2016) 'Robot-aided cloth classification using depth information and CNNs', in *International Conference on Articulated Motion and Deformable Objects*. Springer, pp. 16–23.

59. **Gallet, A., Ruel, L., Staccini-Lavenant, L. and Thérond, P.P.** (2006) 'Cholesterol modification is necessary for controlled planar long-range activity of Hedgehog in Drosophila epithelia', *Development*, 133(3), pp. 407–418. Available at: https://doi.org/10.1242/dev.02212.

60. **Garcia, A.D.R., Han, Y.-G., Triplett, J.W., Farmer, W.T., Harwell, C.C. and Ihrie, R.A.** (2018) 'The Elegance of Sonic Hedgehog: Emerging Novel Functions for a Classic Morphogen', *The Journal of Neuroscience: The Official Journal of the Society for Neuroscience*, 38(44), pp. 9338–9345. Available at: https://doi.org/10.1523/JNEUROSCI.1662-18.2018.

61. **Garcia, K.E., Okamoto, R.J., Bayly, P.V. and Taber, L.A.** (2017) 'Contraction and stress-dependent growth shape the forebrain of the early chicken embryo', *Journal of the Mechanical Behavior of Biomedical Materials*, 65, pp. 383–397. Available at: https://doi.org/10.1016/j.jmbbm.2016.08.010.

62. **Garcia, K.E., Stewart, W.G., Espinosa, M.G., Gleghorn, J.P. and Taber, L.A.** (2019) 'Molecular and mechanical signals determine morphogenesis of the cerebral hemispheres in the chicken embryo', *Development (Cambridge, England)*, 146(20), p. dev174318. Available at: https://doi.org/10.1242/dev.174318.

63. **Gillard, G. and Röper, K.** (2020) 'Control of cell shape during epithelial

morphogenesis: recent advances', *Current Opinion in Genetics & Development*, 63, pp. 1–8. Available at: https://doi.org/10.1016/j.gde.2020.01.003.

64. **Goetz, S.C. and Anderson, K.V.** (2010) 'The primary cilium: a signalling centre during vertebrate development', *Nature Reviews Genetics*, 11(5), pp. 331–344. Available at: https://doi.org/10.1038/nrg2774.

65. **Goodfellow, I. and Bengio, A., Y. and Courville** (2016) *Deep Learning*. MIT Press.

66. **Groves, I., Placzek, M. and Fletcher, A.G.** (2020) 'Of mitogens and morphogens: modelling Sonic Hedgehog mechanisms in vertebrate development', *Philosophical Transactions of the Royal Society B: Biological Sciences*, 375(1809), p. 20190660. Available at: https://doi.org/10.1098/rstb.2019.0660.

67. **Hallou, A., Yevick, H.G., Dumitrascu, B. and Uhlmann, V.** (2021) 'Deep learning for bioimage analysis in developmental biology', *Development*, 148(18), p. dev199616. Available at: https://doi.org/10.1242/dev.199616.

68. **Hamburger, V. and Hamilton, H.L.** (1951) 'A series of normal stages in the development of the chick embryo', *J. Morphol.*, 88, pp. 49–92. Available at: https://doi.org/10.1002/aja.1001950404.

69. **Hans, F. and Dimitrov, S.** (2001) 'Histone H3 phosphorylation and cell division', *Oncogene*, 20(24), pp. 3021–3027. Available at: https://doi.org/10.1038/sj.onc.1204326.

70. **Haralick, R., Shanmugam, K. and Dinstein, I.** (1973) 'Textural Features for Image Classification', *IEEE Trans. Syst. Man Cybern.* [Preprint]. Available at: https://doi.org/10.1109/TSMC.1973.4309314.

71. **Haworth, K.E., Wilson, J.M., Grevellec, A., Cobourne, M.T., Healy, C., Helms, J.A., Sharpe, P.T. and Tucker, A.S.** (2007) 'Sonic hedgehog in the pharyngeal endoderm controls arch pattern via regulation of Fgf8 in head ectoderm', *Developmental Biology*, 303(1), pp. 244–258. Available at: https://doi.org/10.1016/j.ydbio.2006.11.009.

72. **He, K., Zhang, X., Ren, S. and Sun, J.** (2016) 'Deep residual learning for image recognition', in *Proceedings of IEEE Computer Society Conference on Computer Vision and Pattern Recognition*, pp. 770–778.

73. **Hernández-García, A. and König, P.** (2018) 'Data augmentation instead of explicit regularization', *arXiv preprint arXiv:1806.03852* [Preprint].

74. **Hjørland, B. and Albrechtsen, H.** (1995) 'Toward a new horizon in information science: Domain-analysis', *Journal of the American Society for Information Science*, 46(6), pp. 400–425. Available at: https://doi.org/10.1002/(SICI)1097-4571(199507)46:6<400::AID-ASI2>3.0.CO;2-Y.

75. **Hunter, J.D. (2007)** 'Matplotlib: A 2D graphics environment', *Comput. Sci. Eng.*, 9, pp. 90–95. Available at: https://doi.org/10.1109/MCSE.2007.55.

76. **Hynes, M., Porter, J.A., Chiang, C., Chang, D., Tessier-Lavigne, M., Beachy, P.A. and Rosenthal, A.** (1995) 'Induction of midbrain dopaminergic neurons by Sonic hedgehog', *Neuron*, 15(1), pp. 35–44. Available at: https://doi.org/10.1016/0896-6273(95)90062-4.

77. **Iizuka, O., Kanavati, F., Kato, K., Rambeau, M., Arihiro, K. and Tsuneki, M.** (2020) 'Deep learning models for histopathological classification of gastric and colonic

epithelial tumours', *Sci. Rep.*, 10, pp. 1–11. Available at: https://doi.org/10.1038/s41598-020-58467-9.

78. **Jacob, M., Jacob, H.J., Wachtler, F. and Christ, B.** (1984) 'Ontogeny of avian extrinsic ocular muscles', *Cell and Tissue Research*, 237(3), pp. 549–557. Available at: https://doi.org/10.1007/BF00228439.

79. **Jacquemet, G.** (2021) 'Deep learning to analyse microscopy images', *Biochem.*, 43, pp. 60–64. Available at: https://doi.org/10.1042/bio_2021_167.

80. **Jin, L., Wu, J., Bellusci, S. and Zhang, J.-S.** (2019) 'Fibroblast Growth Factor 10 and Vertebrate Limb Development', *Frontiers in Genetics*, 9, p. 705. Available at: https://doi.org/10.3389/fgene.2018.00705.

81. **Jung, A.B., Wada, K., Crall, J., Tanaka, S., Graving, J., Reinders, C., Yadav, S., Banerjee, J., Vecsei, G., Kraft, A., Rui, Z., Borovec, J., Vallentin, C., Zhydenko, S., Pfeiffer, K., Cook, B., Fernández, I., De Rainville, F.-M., Weng, C.-H., Ayala-Acevedo, A., Meudec, R., Laporte, M., and others** (2020) 'imgaug'. Available at: https://github.com/aleju/imgaug.

82. **Kenney, A.M. and Rowitch, D.H.** (2000) 'Sonic hedgehog promotes G(1) cyclin expression and sustained cell cycle progression in mammalian neuronal precursors', *Molecular and Cellular Biology*, 20(23), pp. 9055–9067. Available at: https://doi.org/10.1128/MCB.20.23.9055-9067.2000.

83. **Khosravi, P., Kazemi, E., Zhan, Q., Malmsten, J.E., Toschi, M., Zisimopoulos, P., Sigaras, A., Lavery, S., Cooper, L.A.D., Hickman, C., Meseguer, M., Rosenwaks, Z., Elemento, O., Zaninovic, N. and Hajirasouliha, I.** (2019) 'Deep learning enables robust assessment and selection of human blastocysts after in vitro fertilization', *NPJ Digit. Med.*, 2(1), pp. 1–9. Available at: https://doi.org/10.1038/s41746-019-0096-y.

84. **Kiecker, C. and Niehrs, C.** (2001) 'The role of prechordal mesendoderm in neural patterning', *Current Opinion in Neurobiology*, 11(1), pp. 27–33. Available at: https://doi.org/10.1016/s0959-4388(00)00170-7.

85. **Kim, D.W., Place, E., Chinnaiya, K., Manning, E., Sun, C., Dai, W., Groves, I., Ohyama, K., Burbridge, S., Placzek, M. and Blackshaw, S.** (2022) 'Single-cell analysis of early chick hypothalamic development reveals that hypothalamic cells are induced from prethalamic-like progenitors', *Cell Reports*, 38(3), p. 110251. Available at: https://doi.org/10.1016/j.celrep.2021.110251.

86. **Kim, D.W., Washington, P.W., Wang, Z.Q., Lin, S.H., Sun, C., Ismail, B.T., Wang, H., Jiang, L. and Blackshaw, S.** (2020) 'The cellular and molecular landscape of hypothalamic patterning and differentiation from embryonic to late postnatal development', *Nature Communications*, 11(1), p. 4360. Available at: https://doi.org/10.1038/s41467-020-18231-z.

87. **Kohtz, J.D., Baker, D.P., Corte, G. and Fishell, G.** (1998) 'Regionalization within the mammalian telencephalon is mediated by changes in responsiveness to Sonic Hedgehog', *Development*, 125(24), pp. 5079–5089. Available at: https://doi.org/10.1242/dev.125.24.5079.

88. **Krauss, S., Concordet, J.P. and Ingham, P.W.** (1993) 'A functionally conserved homolog of the Drosophila segment polarity gene hh is expressed in tissues with polarizing activity in zebrafish embryos', *Cell*, 75(7), pp. 1431–1444. Available at: https://doi.org/10.1016/0092-8674(93)90628-4.

89. **Krueger, R., Beyer, J., Jang, W.-D., Kim, N.W., Sokolov, A., Sorger, P.K. and Pfister, H.** (2019) 'Facetto: Combining unsupervised and supervised learning for hierarchical phenotype analysis in multi-channel image data', *IEEE Trans. Vis. Comput. Graph.*, 26(1), pp. 227–237. Available at: https://doi.org/10.1109/TVCG.2019.2934547.

90. **Lechan, R.M. and Toni, R.** (2000) 'Functional Anatomy of the Hypothalamus and Pituitary', in K.R. Feingold, B. Anawalt, A. Boyce, G. Chrousos, W.W. de Herder, K. Dhatariya, K. Dungan, J.M. Hershman, J. Hofland, S. Kalra, G. Kaltsas, C. Koch, P. Kopp, M. Korbonits, C.S. Kovacs, W. Kuohung, B. Laferrère, M. Levy, E.A. McGee, R. McLachlan, J.E. Morley, M. New, J. Purnell, R. Sahay, F. Singer, M.A. Sperling, C.A. Stratakis, D.L. Trence, and D.P. Wilson (eds) *Endotext*. South Dartmouth (MA): MDText.com, Inc. Available at: http://www.ncbi.nlm.nih.gov/books/NBK279126/ (Accessed: 23 June 2022).

91. **LeCun, Y., Bengio, Y. and Hinton, G.** (2015) 'Deep learning', *Nature*, 521(7553), pp. 436–444. Available at: https://doi.org/10.1038/nature14539.

92. **LeCun, Y., Bottou, L., Bengio, Y. and Haffner, P.** (1998) 'Gradient-based learning applied to document recognition', *Proc. IEEE*, 86(11), pp. 2278–2324. Available at: https://doi.org/10.1109/5.726791.

93. **Lee, J.-M., Miyazawa, S., Shin, J.-O., Kwon, H.-J., Kang, D.-W., Choi, B.-J., Lee, J.-H., Kondo, S., Cho, S.-W. and Jung, H.-S.** (2011) 'Shh signaling is essential for rugae morphogenesis in mice', *Histochemistry and Cell Biology*, 136(6), pp. 663–675. Available at: https://doi.org/10.1007/s00418-011-0870-7.

94. **Legland, D., Arganda-Carreras, I. and Andrey, P.** (2016) 'MorphoLibJ: integrated library and plugins for mathematical morphology with ImageJ', *Bioinformatics*, 32(22), pp. 3532–3534. Available at: https://doi.org/10.1093/bioinformatics/btw413.

95. **Gaetan G. Lehmann, David Legland** (2012)**.** Efficient N-Dimensional surface estimation using Crofton formula and run-length encoding. https://hal.inrae.fr/hal-02811118

96. **LeNail, A.** (2019) 'NN-SVG: publication-ready neural network architecture schematics', *J. Open Source Softw.*, 4(33), p. 747. Available at: https://doi.org/10.21105/joss.00747.

97. **Litingtung, Y., Lei, L., Westphal, H. and Chiang, C.** (1998) 'Sonic hedgehog is essential to foregut development', *Nature Genetics*, 20(1), pp. 58–61. Available at: https://doi.org/10.1038/1717.

98. **Manning, L., Ohyama, K., Saeger, B., Hatano, O., Wilson, S.A., Logan, M. and Placzek, M.** (2006) 'Regional Morphogenesis in the Hypothalamus: A BMP-Tbx2 Pathway Coordinates Fate and Proliferation through Shh Downregulation', *Developmental Cell*, 11(6), pp. 873–885. Available at: https://doi.org/10.1016/j.devcel.2006.09.021.

99. **Margapuri, V., Lavezzi, G., Stewart, R. and Wagner, D.** (2020) 'Bombus Species Image Classification', *arXiv preprint arXiv:2006.11374* [Preprint].

100. **Marigo, V., Johnson, R.L., Vortkamp, A. and Tabin, C.J.** (1996) 'Sonic hedgehog differentially regulates expression of GLI and GLI3 during limb development', *Developmental Biology*, 180(1), pp. 273–283. Available at: https://doi.org/10.1006/dbio.1996.0300.

101. **Marigo, V., Roberts, D.J., Lee, S.M., Tsukurov, O., Levi, T., Gastier, J.M., Epstein, D.J., Gilbert, D.J., Copeland, N.G. and Seidman, C.E.** (1995) 'Cloning, expression, and chromosomal location of SHH and IHH: two human homologues of the Drosophila segment polarity gene hedgehog', *Genomics*, 28(1), pp. 44–51. Available at: https://doi.org/10.1006/geno.1995.1104.

102. **Marigo, V. and Tabin, C.J.** (1996) 'Regulation of patched by sonic hedgehog in the developing neural tube', *Proceedings of the National Academy of Sciences of the United States of America*, 93(18), pp. 9346–9351. Available at: https://doi.org/10.1073/pnas.93.18.9346.

103. **Menshykau, D., Kraemer, C. and Iber, D.** (2012) 'Branch Mode Selection during Early Lung Development', *PLOS Computational Biology*, 8(2), p. e1002377. Available at: https://doi.org/10.1371/journal.pcbi.1002377.

104. **Moir, L., Bochukova, E.G., Dumbell, R., Banks, G., Bains, R.S., Nolan, P.M., Scudamore, C., Simon, M., Watson, K.A., Keogh, J., Henning, E., Hendricks, A., O'Rahilly, S., Barroso, I., Sullivan, A.E., Bersten, D.C., Whitelaw, M.L., Kirsch, S., Bentley, E., Farooqi, I.S. and Cox, R.D.** (2017) 'Disruption of the homeodomain transcription factor orthopedia homeobox (Otp) is associated with obesity and anxiety', *Molecular Metabolism*, 6(11), pp. 1419–1428. Available at: https://doi.org/10.1016/j.molmet.2017.08.006.

105. **Musy, M., Flaherty, K., Raspopovic, A., J. and Robert-Moreno, Richtsmeier, J.T. and Sharpe, J.** (2018) 'A quantitative method for staging mouse embryos based on limb morphometry', *Development*, 145, p. dev154856. Available at: https://doi.org/10.1242/dev.154856.

106. **Nagase, T., Nagase, M., Osumi, N., Fukuda, S., Nakamura, S., Ohsaki, K., Harii, K., Asato, H. and Yoshimura, K.** (2005) 'Craniofacial anomalies of the cultured mouse embryo induced by inhibition of sonic hedgehog signaling: an animal model of holoprosencephaly', *The Journal of Craniofacial Surgery*, 16(1), pp. 80–88. Available at: https://doi.org/10.1097/00001665-200501000-00016.

107. **Newgreen, D.F. and Erickson, C.A.** (1986) 'The migration of neural crest cells', *Int. Rev. Cyt.*, 103, pp. 89–145. Available at: https://doi.org/10.1016/S0074-7696(08)60834-7.

108. **Ohyama, K., Ellis, P., Kimura, S. and Placzek, M.** (2005) 'Directed differentiation of neural cells to hypothalamic dopaminergic neurons', *Development*, 132(23), pp. 5185–5197. Available at: https://doi.org/10.1242/dev.02094.

109. **Palma, V., Lim, D.A., Dahmane, N., Sánchez, P., Brionne, T.C., Herzberg, C.D., Gitton, Y., Carleton, A., Alvarez-Buylla, A. and Ruiz i Altaba, A.** (2005) 'Sonic hedgehog controls stem cell behavior in the postnatal and adult brain', *Development (Cambridge, England)*, 132(2), pp. 335–344. Available at: https://doi.org/10.1242/dev.01567.

110. **Palmeirim, I., Henrique, D., Ish-Horowicz, D. and Pourquié, O.** (1997) 'Avian hairy gene expression identifies a molecular clock linked to vertebrate segmentation and somitogenesis', *Cell*, 91, pp. 639–648. Available at: https://doi.org/10.1016/S0092-8674(00)80451-1.

111. **Panwar, H., Gupta, P.K., Siddiqui, M.K., Morales-Menendez, R., Bhardwaj, P. and Singh, V.** (2020) 'A deep learning and grad-CAM based color visualization approach for fast detection of COVID-19 cases using chest X-ray and CT-Scan images', *Chaos Solitons Fractals*, 140, p. 110190. Available at:

https://doi.org/10.1016/j.chaos.2020.110190.

112. **Partridge, M. and Calvo, R.A.** (1998) 'Fast dimensionality reduction and simple PCA', *Intell. Data Anal.*, 2(3), pp. 203–214. Available at: https://doi.org/10.1016/S1088-467X(98)00024-9.

113. **Patten, I., Kulesa, P., Shen, M.M., Fraser, S. and Placzek, M.** (2003) 'Distinct modes of floor plate induction in the chick embryo', *Development*, 130(20), pp. 4809–4821. Available at: https://doi.org/10.1242/dev.00694.

114. **Pearson, C.A., Ohyama, K., Manning, L., Aghamohammadzadeh, S., Sang, H. and Placzek, M.** (2011) 'FGF-dependent midline-derived progenitor cells in hypothalamic infundibular development', *Development*, 138(12), pp. 2613–2624. Available at: https://doi.org/10.1242/dev.062794.

115. **Pedregosa, F., Varoquaux, G., Gramfort, A., Michel, V., Thirion, B., Grisel, O., Blondel, M., Prettenhofer, P., Weiss, R., Dubourg, V., Vanderplas, J., Passos, A., Cournapeau, D., Brucher, M., Perrot, M. and Duchesnay, E.** (2011) 'Scikit-learn: machine learning in Python', *J. Mach. Learn. Res.*, 12, pp. 2825–2830.

116. **Pepicelli, C.V., Lewis, P.M. and McMahon, A.P.** (1998) 'Sonic hedgehog regulates branching morphogenesis in the mammalian lung', *Current biology: CB*, 8(19), pp. 1083–1086. Available at: https://doi.org/10.1016/s0960-9822(98)70446-4.

117. **Pickering, J., Chinnaiya, K. and Towers, M.** (2019) 'An autoregulatory cell cycle timer integrates growth and specification in chick wing digit development', *eLife*. Edited by M.E. Bronner, 8, p. e47625. Available at: https://doi.org/10.7554/eLife.47625.

118. **Placzek, M. and Briscoe, J.** (2005) 'The floor plate: multiple cells, multiple signals', *Nature Reviews. Neuroscience*, 6(3), pp. 230–240. Available at: https://doi.org/10.1038/nrn1628.

119. **Placzek, M. and Briscoe, J.** (2018) 'Sonic hedgehog in vertebrate neural tube development', *International Journal of Developmental Biology*, 62(1-2–3), pp. 225–234. Available at: https://doi.org/10.1387/ijdb.170293jb.

120. **Placzek, M., Jessell, T.M. and Dodd, J.** (1993) 'Induction of floor plate differentiation by contact-dependent, homeogenetic signals', *Development*, 117(1), pp. 205–218. Available at: https://doi.org/10.1242/dev.117.1.205.

121. **Pond, A.J.R., Hwang, S., Verd, B. and Steventon, B.** (2021) 'A deep learning approach for staging embryonic tissue isolates with small data', *PLoS One*, 16, p. e0244151. Available at: https://doi.org/10.1371/journal.pone.0244151.

122. **Puelles, L. and Rubenstein, J.L.R.** (2003) 'Forebrain gene expression domains and the evolving prosomeric model', *Trends in Neurosciences*, 26(9), pp. 469–476. Available at: https://doi.org/10.1016/S0166-2236(03)00234-0.

123. **Ranjan, S., Nayak, D.R., Kumar, K.S., Dash, R. and Majhi, B.** (2017) 'Hyperspectral image classification: A k-means clustering based approach', in *4th International Conference on Advanced Computing and Communication Systems*, pp. 1–7. Available at: https://doi.org/10.1109/ICACCS.2017.8014707.

124. **Riddle, R.D., Johnson, R.L., Laufer, E. and Tabin, C.** (1993) 'Sonic hedgehog mediates the polarizing activity of the ZPA', *Cell*, 75(7), pp. 1401–1416. Available at: https://doi.org/10.1016/0092-8674(93)90626-2.

125. **Roelink, H., Augsburger, A., Heemskerk, J., Korzh, V., Norlin, S., Ruiz i Altaba, A., Tanabe, Y., Placzek, M., Edlund, T. and Jessell, T.M.** (1994) 'Floor plate and motor neuron induction by vhh-1, a vertebrate homolog of hedgehog expressed by the notochord', *Cell*, 76(4), pp. 761–775. Available at: https://doi.org/10.1016/0092-8674(94)90514-2.

126. **Rohatgi, R., Milenkovic, L. and Scott, M.P.** (2007) 'Patched1 regulates hedgehog signaling at the primary cilium', *Science (New York, N.Y.)*, 317(5836), pp. 372–376. Available at: https://doi.org/10.1126/science.1139740.

127. **Ronneberger, O., Fischer, P. and Brox, T.** (2015) 'U-Net: Convolutional Networks for Biomedical Image Segmentation'. arXiv. Available at: https://doi.org/10.48550/arXiv.1505.04597.

128. **Rosin, P.L. and Fierens, F.** (1995) 'Improving neural network generalisation', in *International Geoscience and Remote Sensing Symposium*. IEEE, pp. 1255–1257.

129. **Rowitch, D.H., S-Jacques, B., Lee, S.M., Flax, J.D., Snyder, E.Y. and McMahon, A.P.** (1999) 'Sonic hedgehog regulates proliferation and inhibits differentiation of CNS precursor cells', *The Journal of Neuroscience: The Official Journal of the Society for Neuroscience*, 19(20), pp. 8954–8965.

130. **Rubenstein, J.L., Martinez, S., Shimamura, K. and Puelles, L.** (1994) 'The embryonic vertebrate forebrain: the prosomeric model', *Science (New York, N.Y.)*, 266(5185), pp. 578–580. Available at: https://doi.org/10.1126/science.7939711.

131. **Sáenz-Ponce, N., Mitgutsch, C. and del Pino, E.M.** (2012) 'Variation in the schedules of somite and neural development in frogs', *Proc. Natl. Acad. Sci. U.S.A.*, 109, pp. 20503–20507. Available at: https://doi.org/10.1073/pnas.1219307110.

132. **Saha, K. and Schaffer, D.V.** (2006) 'Signal dynamics in Sonic hedgehog tissue patterning', *Development*, 133(5), pp. 889–900. Available at: https://doi.org/10.1242/dev.02254.

133. **Schindelin, J., Arganda-Carreras, I., Frise, E., Kaynig, V., Longair, M., Pietzsch, T., Preibisch, S., Rueden, C., Saalfeld, S., Schmid, B., Tinevez, J.-Y., White, D.J., Hartenstein, V., Eliceiri, K., Tomancak, P. and Cardona, A.** (2012) 'Fiji: an open-source platform for biological-image analysis', *Nature Methods*, 9(7), pp. 676–682. Available at: https://doi.org/10.1038/nmeth.2019.

134. **Schmid, B., Schindelin, J., Cardona, A., Longair, M. and Heisenberg, M.** (2010) 'A high-level 3D visualization API for Java and ImageJ', *BMC Bioinformatics*, 11(1), p. 274. Available at: https://doi.org/10.1186/1471-2105-11-274.

135. **Seifert, R. and Christ, B**. (1990) 'On the differentiation and origin of myoid cells in the avian thymus', *Anatomy and Embryology*, 181(3), pp. 287–298. Available at: https://doi.org/10.1007/BF00174622.

136. **Sekine, K., Ohuchi, H., Fujiwara, M., Yamasaki, M., Yoshizawa, T., Sato, T., Yagishita, N., Matsui, D., Koga, Y., Itoh, N. and Kato, S.** (1999) 'Fgf10 is essential for limb and lung formation', *Nature Genetics*, 21(1), pp. 138–141. Available at: https://doi.org/10.1038/5096.

137. **Shimogori, T., Lee, D.A., Miranda-Angulo, A., Yang, Y., Wang, H., Jiang, L., Yoshida, A.C., Kataoka, A., Mashiko, H., Avetisyan, M., Qi, L., Qian, J. and Blackshaw, S**. (2010) 'A genomic atlas of mouse hypothalamic development', *Nature Neuroscience*, 13(6), pp. 767–775. Available at: https://doi.org/10.1038/nn.2545.

138. **Shin, S., Lee, Y., Kim, M., Park, J., Lee, S. and Min, K.** (2020) 'Deep neural network model with Bayesian hyperparameter optimization for prediction of NOx at transient conditions in a diesel engine', *Eng. Appl. Artif. Intell.*, 94, p. 103761. Available at: https://doi.org/10.1016/j.engappai.2020.103761.

139. **Simard, P.Y., Steinkraus, D. and Platt, J.C.** (2003) 'Best practices for convolutional neural networks applied to visual document analysis', in *Icdar*.

140. **Simonyan, K., Vedaldi, A. and Zisserman, A.** (2014) 'Deep Inside Convolutional Networks: Visualising Image Classification Models and Saliency Maps', *arXiv:1312.6034 [cs]* [Preprint]. Available at: http://arxiv.org/abs/1312.6034 (Accessed: 17 February 2022).

141. **Simonyan, K. and Zisserman, A.** (2014) 'Very deep convolutional networks for large-scale image recognition', *arXiv preprint arXiv:1409.1556* [Preprint].

142. **Smilkov, D., Thorat, N., Kim, B., Viégas, F. and Wattenberg, M.** (2017) 'Smoothgrad: removing noise by adding noise', *arXiv preprint arXiv:1706.03825* [Preprint].

143. **Srivastava, N.** (2013) 'Improving neural networks with dropout', *University of Toronto*, 182(566), p. 7.

144. **Swanson** (1987) 'The hypothalamus', in. Elsevier (Handbook of Chemical Neuroanatomy), pp. 1-124.

145. **Swanson, L.** (1992) *Brain Maps: Structure of the Rat Brain*. (Elsevier, Amsterdam).

146. **Swanson, L.W.** (2012) *Brain Architecture: Understanding the Basic Plan*. Oxford University Press.

147. **Szabó, N.-E., Zhao, T., Çankaya, M., Theil, T., Zhou, X. and Alvarez-Bolado, G.** (2009) 'Role of Neuroepithelial Sonic hedgehog in Hypothalamic Patterning', *Journal of Neuroscience*, 29(21), pp. 6989–7002. Available at: https://doi.org/10.1523/JNEUROSCI.1089-09.2009.

148. **Szegedy, C., Liu, W., Jia, Y., Sermanet, P., Reed, S., Anguelov, D., Erhan, D., Vanhoucke, V. and Rabinovich, A.** (2015) 'Going deeper with convolutions', in *Proceedings of IEEE Computer Society Conference on Computer Vision and Pattern Recognition*, pp. 1–9.

149. **Thompson, D.W.** (1917) *On Growth and Form*. Edited by J.T. Bonner. Cambridge: Cambridge University Press (Canto). Available at: https://doi.org/10.1017/CBO9781107325852.

150. **Thompson, N.C., Greenewald, K., Lee, K. and Manso, G.F.** (2020) 'The computational limits of deep learning', *arXiv preprint arXiv:2007.05558* [Preprint].

151. **Tickle, C., Summerbell, D. and Wolpert, L.** (1975) 'Positional signalling and specification of digits in chick limb morphogenesis', *Nature*, 254(5497), pp. 199–202. Available at: https://doi.org/10.1038/254199a0.

152. **Tickle, C. and Towers, M.** (2017) 'Sonic Hedgehog Signaling in Limb Development', *Frontiers in Cell and Developmental Biology*, 5. Available at: https://www.frontiersin.org/articles/10.3389/fcell.2017.00014 (Accessed: 23 July 2022).

153. **Towers, M., Mahood, R., Yin, Y. and Tickle, C.** (2008a) 'Integration of growth and specification in chick wing digit-patterning', *Nature*, 452(7189), pp. 882–886. Available at: https://doi.org/10.1038/nature06718.

154. **Trowe, M.-O., Zhao, L., Weiss, A.-C., Christoffels, V., Epstein, D.J. and Kispert, A.** (2013) 'Inhibition of Sox2-dependent activation of Shh in the ventral diencephalon by Tbx3 is required for formation of the neurohypophysis', *Development (Cambridge, England)*, 140(11), pp. 2299–2309. Available at: https://doi.org/10.1242/dev.094524.

155. **Turing, A.** (1952) The chemical basis of morphogenesis. Philosophical Transactions of the Royal Society of London. Series B, Biological Sciences, Vol. 237, No. 641 (1952), 37-72.

156. **Ulloa, F. and Briscoe, J.** (2007) 'Morphogens and the control of cell proliferation and patterning in the spinal cord', *Cell Cycle (Georgetown, Tex.)*, 6(21), pp. 2640–2649. Available at: https://doi.org/10.4161/cc.6.21.4822.

157. **Valet, M., Siggia, E.D. and Brivanlou, A.H.** (2022) 'Mechanical regulation of early vertebrate embryogenesis', *Nature Reviews Molecular Cell Biology*, 23(3), pp. 169–184. Available at: https://doi.org/10.1038/s41580-021-00424-z.

158. **Wallace, V.A.** (1999) 'Purkinje-cell-derived Sonic hedgehog regulates granule neuron precursor cell proliferation in the developing mouse cerebellum', *Current biology: CB*, 9(8), pp. 445–448. Available at: https://doi.org/10.1016/s0960-9822(99)80195-x.

159. **Waskom, M., Gelbart, M., Botvinnik, O., Ostblom, J., Hobson, P., Lukauskas, S., Gemperline, D.C., Augspurger, T., Halchenko, Y., Warmenhoven, J., Cole, J.B., Ruiter, J. de, Vanderplas, J., Hoyer, S., Pye, C., Miles, A., Swain, C., Meyer, K., Martin, M., Bachant, P., Quintero, E., Kunter, G., Villalba, S., Brian, Fitzgerald, C., Evans, C., Williams, M.L., O'Kane, D., Yarkoni, T. and Brunner, T.** (2021) 'mwaskom/seaborn: v0.11.2 (August 2021)'. Zenodo. Available at: https://doi.org/10.5281/zenodo.5205191.

160. **Wechsler-Reya, R.J. and Scott, M.P.** (1999) 'Control of neuronal precursor proliferation in the cerebellum by Sonic Hedgehog', *Neuron*, 22(1), pp. 103–114. Available at: https://doi.org/10.1016/s0896-6273(00)80682-0.

161. **Weiss, L.E., Milenkovic, L., Yoon, J., Stearns, T. and Moerner, W.E.** (2019) 'Motional dynamics of single Patched1 molecules in cilia are controlled by Hedgehog and cholesterol', *Proceedings of the National Academy of Sciences*, 116(12), pp. 5550–5557. Available at: https://doi.org/10.1073/pnas.1816747116.

162. **Wibmer, A., Hricak, H., Gondo, T., Matsumoto, K., Veeraraghavan, H., Fehr, D., Zheng, J., Goldman, D., Moskowitz, C., Fine, S., Reuter, V.E., Eastham, J., Sala, E. and Vargas, H.A.** (2015) 'Haralick Texture Analysis of prostate MRI: Utility for differentiating non-cancerous prostate from prostate cancer and differentiating prostate cancers with different Gleason Scores', *European radiology*, 25(10), pp. 2840–2850. Available at: https://doi.org/10.1007/s00330-015-3701-8.

163. **Wilson, S.L., Wilson, J.P., Wang, C., Wang, B. and McConnell, S.K.** (2012) 'Primary cilia and Gli3 activity regulate cerebral cortical size', *Developmental Neurobiology*, 72(9), pp. 1196–1212. Available at: https://doi.org/10.1002/dneu.20985.

164. **Wolny, A., Cerrone, L., Vijayan, A., Tofanelli, R., Barro, A.V., Louveaux, M.,**

Wenzl, C., Strauss, S., Wilson-Sánchez, D., Lymbouridou, R., Steigleder, S.S., Pape, C., Bailoni, A., Duran-Nebreda, S., Bassel, G.W., Lohmann, J.U., Tsiantis, M., Hamprecht, F.A., Schneitz, K., Maizel, A. and Kreshuk, A. (2020) 'Accurate and versatile 3D segmentation of plant tissues at cellular resolution', *eLife*. Edited by C.S. Hardtke, D.C. Bergmann, D.C. Bergmann, and M. Graeff, 9, p. e57613. Available at: https://doi.org/10.7554/eLife.57613.

165. **Wolpert, L.** (1969) 'Positional information and the spatial pattern of cellular differentiation', *Journal of Theoretical Biology*, 25(1), pp. 1–47. Available at: https://doi.org/10.1016/s0022-5193(69)80016-0.

166. **Wu, Z., Zhang, W., Chen, G., Cheng, Lu, Liao, J., Jia, N., Gao, Y., Dai, H., Yuan, J., Cheng, Linzhao and Xiao, L.** (2008) 'Combinatorial Signals of Activin/Nodal and Bone Morphogenic Protein Regulate the Early Lineage Segregation of Human Embryonic Stem Cells*', *Journal of Biological Chemistry*, 283(36), pp. 24991–25002. Available at: https://doi.org/10.1074/jbc.M803893200.

167. **Xu, J., Liu, H., Lan, Y., Aronow, B.J., Kalinichenko, V.V. and Jiang, R.** (2016) 'A Shh-Foxf-Fgf18-Shh Molecular Circuit Regulating Palate Development', *PLoS genetics*, 12(1), p. e1005769. Available at: https://doi.org/10.1371/journal.pgen.1005769.

168. **Xu, Q., Guo, L., Moore, H., Waclaw, R.R., Campbell, K. and Anderson, S.A.** (2010) 'Sonic hedgehog signaling confers ventral telencephalic progenitors with distinct cortical interneuron fates', *Neuron*, 65(3), pp. 328–340. Available at: https://doi.org/10.1016/j.neuron.2010.01.004.

169. **Yamada, T., Placzek, M., Tanaka, H., Dodd, J. and Jessell, T.M.** (1991) 'Control of cell pattern in the developing nervous system: polarizing activity of the floor plate and notochord', *Cell*, 64(3), pp. 635–647. Available at: https://doi.org/10.1016/0092-8674(91)90247-v.

170. **Yasuhiro, K.** (2021) 'tf-keras-vis', *GitHub repository*. GitHub. Available at: https://github.com/keisen/tf-keras-vis.

171. **Yu, Y., Arora, A., Min, W., Roifman, C.M. and Grunebaum, E.** (2009) 'EdU incorporation is an alternative non-radioactive assay to [(3)H]thymidine uptake for in vitro measurement of mice T-cell proliferations', *Journal of Immunological Methods*, 350(1–2), pp. 29–35. Available at: https://doi.org/10.1016/j.jim.2009.07.008.

172. **Zeng, X., Goetz, J.A., Suber, L.M., Scott, W.J., Schreiner, C.M. and Robbins, D.J.** (2001) 'A freely diffusible form of Sonic hedgehog mediates long-range signalling', *Nature*, 411(6838), pp. 716–720. Available at: https://doi.org/10.1038/35079648.

173. **Zhang, J. and Mitliagkas, I. (2019)** 'YellowFin and the Art of Momentum Tuning', *Proceedings of Machine Learning and Systems*, 1, pp. 289–308.

174. **Zhou, S., Zhang, J., Jiang, H., Lundh, T. and Ng, A.Y.** (2021) 'Data augmentation with Mobius transformations', *Mach. Learn.: Sci. Technol.*, 2, p. 025016. Available at: https://doi.org/10.1088/2632-2153/abd615.

175. **Zhu, J. and Mackem, S.** (2011) 'Analysis of mutants with altered Shh activity and posterior digit loss supports a biphasic model for Shh function as a morphogen and mitogen', *Developmental dynamics : an official publication of the American Association of Anatomists*, 240(5), pp. 1303–1310. Available at: https://doi.org/10.1002/dvdy.22637.

176. **Z. Stanton, B. and F. Peng, L.** (2010) ‘Small-molecule modulators of the Sonic Hedgehog signaling pathway’, *Molecular BioSystems*, 6(1), pp. 44–54. Available at: https://doi.org/10.1039/B910196A.